Numerical Simulations of the Black Summer Fires: Impact of Moisture, Sensible Heat Release and Aerosol-Radiation Interaction on the Smoke Plume and Cloud Formation

Zur Erlangung des akademischen Grades einer
DOKTORIN DER NATURWISSENSCHAFTEN (Dr. rer. nat.)
von der KIT-Fakultät für Physik des
Karlsruher Instituts für Technologie (KIT)

genehmigte

DISSERTATION

von

M.Sc. Lisa Janina Muth
aus Bad Homburg vor der Höhe

Tag der mündlichen Prüfung:	26.04.2024
Referentin:	Prof. Dr. Corinna Hoose
Korreferent:	Prof. Dr. Peter Braesicke

Abstract

Vegetation fires are a natural part of fire-prone ecosystems. In the face of climate change extreme fire events are expected to increase. One recent example is the Australian bushfire season 2019/2020, also referred to as Black Summer. This is the most severe and intense season on record and had a peak over New Years in south-east Australia. These severe fires were accompanied by a "pyro-cumulonimbus super outbreak". Pyro-cumulonimbus (pyro-Cbs) are cumulonimbus clouds created by strong updrafts from intense vegetation fires. Sufficient available moisture leads to convective cloud formation, increasing the buoyancy through latent heat release, transporting the fire emissions up to the upper troposphere/lower stratosphere region.

Vegetation fires emit gases and aerosols into the atmosphere, which have a strong impact on air quality, atmospheric chemistry and the Earth's radiation budget. One way to quantify these impacts is the use of numerical modeling. Numerical simulations with grid resolutions in the order of a 100 m resolve convection and are therefore able to resolve the plume rise explicitly based on buoyancy fluxes (sensible and latent heat release). Weather and climate models with coarser grid resolutions, in the order of 10 km-100 km, usually parameterize convection and therefore also need to parameterize or assume an emission height.

In this study the numerical model ICON-ART is used to simulate the plume rise and transport of biomass burning aerosols in two different setups. First, a plume-resolving setup (600 m grid spacing) is used. For this, a parameterization for the sensible heat and moisture release by the fire is implemented in the model. This implementation enables the simulation of moist convection lifting the aerosol plume up to 12 km, the tropopause region. The heat and moisture release is given by the input data form the Global Fire Assimilation System (GFAS), which varies spatially, creating a wide range of simulated plume heights. A sensitivity study indicates that the plume height and the triggering of moist convection is more sensitive to the heat release than to the release of moisture.

The plume-resolving simulation is limited by the small simulation domain and is not suitable for the study of aerosol transport. Therefore, a second setup in the limited area mode with a larger domain is constructed, which parameterizes convection and the plume rise. In a first experiment the impact of moisture release is analyzed, a second experiment analyzes the heat release and in a third experiment the impact of aerosol-radiation interaction is investigated. A final experiment includes all three implementations, namely the heat and moisture release by the fire and the aerosol-radiation interaction. In the plume-parameterizing setup, the effect of moisture release is small. The emission of moisture in grid cells close to saturation leads to a selective increase in cloud water and ice close to the emission

source. The release of sensible heat by the fire generates buoyancy, which lifts the aerosol plume and destabilizes the atmosphere. This results in the plume-rise model predicting increased injection heights. Additionally, the heat release increases convective cloud formation, creating further buoyancy through latent heat release. The increase in initial plume height strongly impacts the transport. Aerosol-radiation interaction is implemented for two size modes in two mixing states. The absorption of solar radiation at the plume top increases the temperature and creates buoyancy, which leads to a self-lofting of the plume. The absorption and scattering of solar radiation by the aerosols further reduce the radiation reaching the surface. This dimming decreases the near surface temperature by up to 7 K. It is also shown that the aerosol-radiative forcing depends on the cloud cover. The experiment including all three implementations shows an increase in plume heights at the beginning of the simulation, which is affiliated with the heat and moisture release by the fire. The plume is distributed more widely horizontally and increases the aerosol mass above clouds. This further leads to an increased lofting effect. With this setup it is possible to simulate plumes that reach the upper troposphere/lower stratosphere region, which is in agreement with observations.

Zusammenfassung

Vegetationsbrände sind natürliche Prozesse in vielen Ökosystemen. Aufgrund des Klimawandels ist mit einer Zunahme extremer und schwer kontrollierbarer Brände zu rechnen. Ein aktuelles Beispiel ist die Waldbrandsaison 2019/2020 in Australien, die als „Black Summer Fires“ bezeichnet wird. Dabei handelt es sich um die schwersten und intensivsten Waldbrände seit Beginn der Aufzeichnungen, die über Neujahr einen Hochpunkt im Südosten Australiens erreichten. Dieser Hochpunkt zeichnet sich durch vermehrte Formation von Pyrocumulonimbus (pyro-Cbs) aus, die durch die starken Auftriebe der Feuer entstehen.

Feueremissionen haben einen großen Einfluss auf den Strahlungshaushalt der Erde, die Atmosphärenchemie und die Luftqualität. Ein Werkzeug zur Quantifizierung dieser Einflüsse sind numerische Modelle. Es gibt Modelle, die in hochaufgelösten Simulation (Auflösung in der Größenordnung 100 m) die Fahnendynamik explizit ausrechnen. Diese Rechnung basiert auf einem durch die Brände generiertem Auftriebsterm (fühlbare und latente Wärmefreisetzung) und explizit gerechneter Konvektion. Wetter- und Klimamodelle haben hingegen eine deutlich gröbere Auflösung (Größenordnung 10 km-100 km). Für diese Simulationen muss die Konvektion parametrisiert werden und damit auch die Injektionshöhe der Feueremissionen.

Im Rahmen dieser Arbeit wird das numerische Modell ICON-ART in zwei verschiedenen Konfigurationen verwendet. Die erste Konfiguration ist konvektionsauflösend mit expliziter Berechnung der Rauchfahne und in der zweiten Konfiguration ist die Konvektion und die Injektionshöhe parametrisiert. Für die Parametrisierung der Injektionshöhe wird ein sogenanntes „plume-rise“-Modell genutzt. Es wird gezeigt, dass die Implementierung von Feuchte- und Wärmefreisetzung durch Brände in einer konvektionsauflösenden Simulation (600 m Gitterabstand) zu feuchter Konvektion führt. Außerdem wird gezeigt, dass sowohl Flüssig- als auch Eiswolken durch die Brände simuliert werden (Pyro-Cumulus). Dieser Prozess transportiert Aerosole bis in eine Höhe von 12 km. Des Weiteren ist es möglich mit diesen Implementierungen die Maximalhöhe des „plume-rise“-Modells zu reproduzieren. Im Vergleich zum „plume-rise“-Modell berücksichtigt die konvektionsauflösende Simulation einen Tagesgang der Wärme- und Feuchtefreisetzung. Beides variiert außerdem abhängig von der gemessenen „Fire Radiative Power“ (FRP), was dazu führt, dass sich die Spannweite der simulierten Fahnenhöhen vergrößert. Die hohe Auflösung limitiert die Größe des Simulationsgebietes und die Aerosolfahne wird schon nach wenigen Stunden aus dem Simulationsgebiet transportiert. Das Setup eignet sich daher nicht, um den Aerosoltransport zu untersuchen. Deswegen werden weitere Experimente in einem größeren Simulationsgebiet durchgeführt, die die Konvektion und Injektionshöhe parametrisieren und ebenfalls den Einfluss von Feuchte-

und Wärmefreisetztung untersuchen. Zusätzlich werden die Aerosol-Strahlungswechselwirkungen analysiert. Beim Setup mit dem „plume-rise“-Modell ist der Effekt der Feuchtefreisetzung gering. Die Emission von Feuchtigkeit in Gitterzellen an der Grenze zur Übersättigung führt vereinzelt zu Anstiegen im Wolkenwasser und Eis. Die Freisetzung fühlbarer Wärme durch die Brände führt zu einer Labilisierung der Atmosphäre, wodurch sich die Injektionshöhen des „plume-rise“-Modell erhöhen. Zusätzlich erzeugter Aufwind unterstützt konvektive Wolkenbildung und es wird mehr latente Wärme freigesetzt. Die Zunahme der anfänglichen Fahnenhöhe wirkt sich stark auf den Transport der Aerosole aus. Die Aerosol-Strahlungswechselwirkung wurde für zwei Größenmoden in zwei Mischungszuständen implementiert. Die Streuung und Absorption solarer Strahlung erwärmt die oberen Aerosolschichten, dies erzeugt einen Auftrieb und lässt die Fahne aufsteigen. Darüber hinaus kommt es zu einer Verringerung der solaren Einstrahlung am Boden, dies reduziert die 2m-Temperatur um bis zu 7 K. Weiter wird gezeigt, dass der Strahlungsantrieb der Aerosole von der Bewölkung abhängt. Ein Experiment, das alle drei Implementierungen beinhaltet (Feuchte- und Wärmefreisetzung, sowie Aerosol-Strahlungswechselwirkung), zeigt einen noch stärkeren Strahlungseffekt, da die Aerosolfahne eine höhere initiale Höhe durch die implementierte Feuchte- und Wärmefreisetzung aufweist und Aerosole dadurch vermehrt oberhalb von Wolken liegen. Der Vergleich mit Satellitenbeobachtungen zeigt, dass die Implementierung von Aerosol-Strahlungswechselwirkung, Wärme- und Feuchtefreisetzung nötig ist um pyro-konvektive Zellen realistisch zu simulieren.

Contents

1. Introduction

Vegetation fires are a natural part of a functioning ecosystem, where the vegetation is influenced by a fire regime with a specific frequency, season, extension and intensity. There are fire-sensitive systems and fire-prone systems. In fire-sensitive systems, for example rain forests and tropical forest, fires usually have negative effects and are mostly related to deforestation and clearing burns (Fidelis, 2020). In fire-prone ecosystems, fire is an ecological and evolutionary factor in maintaining the genetic biodiversity and variability. However, human activity has influenced fire regimes via ignition causes, vegetation properties, fuel availability and vegetation management e.g. grazing, agriculture, prescribed burning, deforestation, and planting (Levin et al., 2021). In the following, the term wildfire is used to describe fires that are unplanned and burn out of control. In recent years, record breaking wildfire events have occurred in fire-prone systems: the Canadian fire storm in August 2017, the Siberian fires in July and August 2019 and the Australian Black Summer Fires 2019/2020. Duane et al. (2021) suggest the extremeness of these events are a consequence of climate change and according to Marlon et al. (2008) it is plausible that wildfire events will increase in future due to climate change.

The emissions of vegetation fires consist of various trace gases and particulate matter. The emitted particles consist of three main components: organic materials, black carbon and trace inorganic species (Lack et al., 2012; Pósfai et al., 2003). The size of these particles ranges from 30 nm to 160 nm for newly emitted particles (Hosseini et al., 2010; Levin et al., 2010) up to 1150 nm for aged particles (Cahill et al., 2008). Therefore, the particles classify as fine ($PM_{2.5}$) to ultrafine particles ($PM_{0.1}$) and impact air quality and human health (Schraufnagel, 2020). The fine particles are able to reach deep into the respiratory system and the interstitial lung, which can trigger an inflammatory process. According to Schraufnagel (2020), the toxicity increases for small particles with large surface areas and further depends on the physical characteristics of the particles. Therefore, it is of interest to know where the smoke originates from, how long it will last and what the pollutant concentrations are. One way to obtain this information is through numerical modeling of the vegetation fire emissions.

For a good representation of the plume characteristics in the model a sufficient understanding of the plume dynamics is necessary. The plume dynamics are a complex interaction of the atmospheric conditions and the fire. Figure 1.1 illustrates these interactions. Fire emits particulate matter and gases into the atmosphere. The heat released by the fire creates buoyancy, further colder ambient air masses are entrained into the plume. The buoyancy and the atmospheric stability determine the plume rise. An additional factor is the available moisture in the atmosphere and released by the fire itself. Sufficient moisture leads to cloud formation, which creates additional buoyancy through latent heat release. The

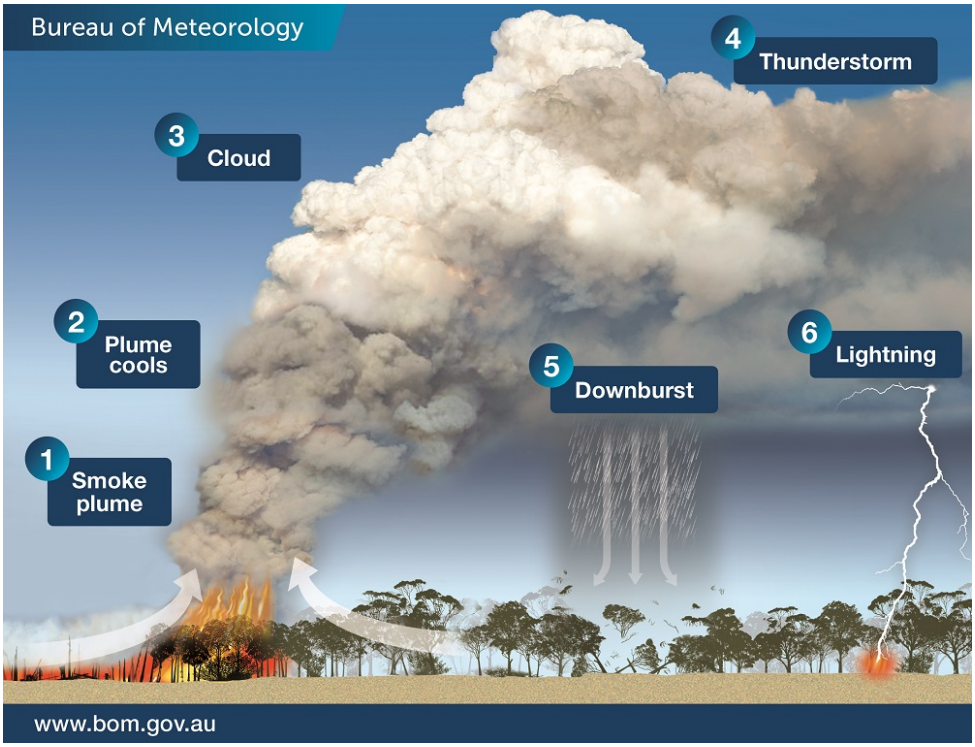

Figure 1.1.: Fire-atmosphere interaction, including pyro-convection with cloud formation. Taken from Bureau of Meteorology (2018).

formation of cumulus and cumulonimbus clouds in connection with fires is referred to as pyro-cumulus (pyro-Cu) and pyro-cumulonimbus (pyro-Cbs) and can transport biomass burning emissions up to the lower stratosphere (Fromm et al., 2012). Figure 1.1 illustrates further that the wind direction and speed near the fire is impacted by the pyro-convection. This often fans the fire and increases the fire spread, creating a positive feedback loop (Bradstock et al., 2012). Changes in wind can further occur when pyro-Cbs create downbursts. Additionally, lightning can start new fires. This is often referred to as "bushfires make their own weather" (BOM, 2018).

The height of the plume is an important attribute, as it determines the smoke transport. The free troposphere is characterized by stronger winds and less turbulence than the boundary layer. Therefore, if smoke reaches the free troposphere it can be transported hundreds or thousands of kilometers away from the fire source (Val Martin et al., 2006). Further, the removal processes are more efficient in the boundary layer which reduces the aerosol lifetime. In contrast, plumes that remain within the boundary layer are well mixed and persist closer to the source (Trentmann et al., 2002). This makes the injection height a key parameter in numerical weather and climate models. Besides the injection height the emission flux of the aerosols and trace gases is of great importance. Information on both parameters is rare and remain with large uncertainties. There are very limited in situ measurements and there is a large spacial and temporal variability of biomass burning, which is why emission monitoring is mostly based on satellite data (Kaiser et al., 2012). Unfortunately, satellite data is also limited by temporal and special resolution,

and disturbed by clouds.

Moreover, the smoke plume transport is impacted by aerosol-radiation interaction. Biomass burning aerosols consist of organic carbon (OC) and black carbon (BC), which absorb solar radiation. This leads to a dimming effect, as less solar radiation reaches the surface. The absorption of solar radiation by optically thick smoke layers further induces a considerable warming of that layer and the ambient air. This heating creates buoyancy and induces a self-lofting of the smoke plume. This effect is shown for example by Hirsch and Koren (2021), Kablick III et al. (2020), Khaykin et al. (2020), and Ohneiser et al. (2020, 2022, 2023) in case of the Australian Black Summer Fires. The self-lofting effect is not only shown for wildfire plumes but also for volcanic plumes (Muser et al., 2020). The impact of aerosol-radiation interaction on the radiative fluxes is referred to as the direct aerosol effect. The changes in atmospheric stability that lead to changes in cloud formation are known as the semi-direct aerosol effect. Last, aerosols can impact cloud microphysics by acting as cloud condensation nuclei (CCN) and ice nucleating particle (INP) and thereby impact the cloud optical properties and lifetime (Liu et al., 2020).

When it comes to simulation of aerosol-radiation-interaction a precise representation of the aerosol optical properties is necessary. The aerosol optical properties are highly dependent on the particle size and the black carbon content (Reid et al., 2005b,a), both parameters vary spatially and temporarily. The initial aerosol properties depend on the fuel type, fuel moisture and combustion phase, but the physical, chemical and optical properties change rapidly as the plume dilutes. This diversity results in large uncertainties and leads to errors in the representation of the biomass burning aerosol optical properties in numerical weather and climate models. This is outlined by Brown et al. (2021), who find that biomass burning aerosols are too absorbing in many climate models.

As argued above, there are various parameters that determine the plume height: the release of sensible and latent heat by the fire, the atmospheric stability, the background meteorology and the emission of aerosols that act as CCN and INP. The interaction of those parameters leads to a wide range of plume altitudes. Labonne et al. (2007) argue based on satellite measurements that a majority of the biomass burning aerosols remain in the mixing layer, because many wildfires occur in high pressure conditions with thermal stability. However, Kahn et al. (2007, 2008) argue that 20 % of the fires over Alaska-Yunkon inject aerosols directly into the free troposphere. This is also supported by the extensive study of Val Martin et al. (2010), which analyzes 3000 plumes over North America, with 4-12 % of the plumes reaching into the free troposphere. Fromm and Servranckx (2003) conclude that for unstable atmospheric conditions pyro-convection can easily loft biomass burning aerosols to the upper troposphere and even the lower stratosphere. There are different approaches and complexities to model the emission height, strongly depending on their purpose. In the following selected studies with different approaches are presented.

A simple approach is to use a fixed emission height. This is done by Colarco et al. (2004), Dirksen et al. (2009), and Lamarque et al. (2003). Dirksen et al. (2009) compare three different fixed emission heights. In their case study fixed emissions at ground level and at around 5 km result in remarkably similar vertical distributions. The comparison with CALIPSO (Cloud-Aerosol Lidar and Infrared Pathfinder

Satellite Observations) measurements shows that the plume height is underestimated in both cases. The third emission height in approximately 10 km agrees best with observations. Another approach is the simulation of an emission profile. An uniform profile throughout the troposphere is used by Lavoué et al. (2000), Pfister et al. (2006), and Wang et al. (2006). Other studies emit a pre-selected fraction of aerosol mass above the boundary layer (Generoso et al., 2007; Hyer et al., 2007; Leung et al., 2007; Turquety et al., 2007). However, these assumptions neglect the impacts of sensible and latent heat release by the fire and cloud microphysical effects.

Empirical-statistical plume-rise parameterizations are developed by Briggs (1975), but according to Raffuse et al. (2012) there is a systematical underestimation of the plume heights. These two empirical approaches rely on time-dependent meteorological conditions, uncertain calculations of the sensible heat flux and neglect latent heat release. This makes it challenging to get an accurate estimation of the plume height (Raffuse et al., 2012). Other empirical parameterizations are presented by Lavoué et al. (2000) and Sofiev et al. (2012).

A further approach is the physical parameterization of the injection height (Freitas et al., 2007, 2010; Kahn et al., 2007; Rio et al., 2010). One of the most commonly used plume-rise models is the one developed by Freitas et al. (2007). This model uses a prognostic scheme that determines the fire buoyancy based on the total sensible heat flux and fire area. It further includes latent heat release. This is also the plume-rise model used in this study and will be explained in more detail in section 4.4. Val Martin et al. (2012) test the Freitas model for different estimates of active fire area and total sensible heat flux with the result that the model is not able to reproduce the plume heights observed by the Multi-angle Imaging SpectroRadiometer (MISR). The plume height dynamic range is generally underestimated, and it does not reliably identify the plumes that are injected into the free troposphere. Therefore, it is necessary to critically assess the limitations of the respective model, assumptions made and uncertainties. Large uncertainties exist in the input parameters of the fire (released sensible and latent heat), as measurements are rare and available measurements, such as MODIS fire radiative power, are affected by clouds and dense smoke above the fire, leading to an underestimation of fire radiative power (FRP). Another challenge is the daily and seasonal fluctuation in emissions (Val Martin et al., 2010). Further, it should be noted that the physical parameterization of the plume rise is computationally expensive.

There are also studies that use inverse modeling to receive the emission mass and injection profile, for example Gonzi and Palmer (2010), but this method is not applicable for forecasts. A different approach to simulate plume rise is the performance of large eddy or convection resolving simulations. There are numerous studies with coupled fire-atmosphere models (Clark and Packham, 1996; Clark et al., 2004; Coen, 2005; Filippi et al., 2013; Kiefer et al., 2010, 2016, 2018; Kochanski et al., 2013; Linn et al., 2002; Mandel et al., 2011; Pimont et al., 2011; Sun et al., 2006). These studies have fine grid resolutions from 4 m-120 m and mainly focus on wind changes by the fire and how this impacts the fire itself. Kiefer et al. (2014) and Kochanski et al. (2016, 2018) use fire-atmosphere models nested to in coarser grid resolution to simulate meso-scale effects.

Trentmann et al. (2006) explicitly simulate the plume rise and conclude that the sensible heat release initiates the convection, while latent heat release from condensation and freezing dominates the total energy budget. The available moisture is mainly entrained and moisture released from the fire is neglectable. Luderer et al. (2006) further investigate these findings and perform sensitivity studies, with the conclusion that the meteorological conditions play a dominant role for pyro-convection. The emission of water vapor is found to be less important for the emission height than the sensible heat release but enhances the aerosol amount transported to the tropopause level. Further, it is found that dynamic and evolution of pyro-Cbs is weakly sensitive to the aerosols acting as CCN. Thurston et al. (2015) perform large eddy simulations to analyze the effect of sensible heat release and environmental moisture on pyro-Cu formation. They are able to simulate large pyro-Cb for intense fires in a moist atmosphere, the pyro-Cbs create substantial precipitation that form evaporation-cooled downbursts. In cases of weak fires in dry atmospheres, pyro-Cu formation is rare.

Research questions and outline

As outlined in the previous sections, there are many uncertainties when it comes to modeling biomass burning emissions, especially for extreme events, when injected into the free troposphere (Val Martin et al., 2012). This work presents numerical simulations of the Australian New Years event (ANY) during the Black Summer Fires, which are performed with the numerical model ICON-ART. This event is characterized by intense pyro-convection and smoke injections up to the lower stratosphere (Heinold et al., 2022). Assumptions and parameterizations of the heat and moisture released by the fires are made, implemented into the model and analyzed for two different grid spacing. Firstly, the plume rise is explicitly simulated in a setup with 600 m grid spacing and resolved convection. This setup is further referred to as "plume-resolving". The second setup has a grid spacing of 6.6 km, therefore convection is parameterized and the injection height is calculated with a one-dimensional plume-rise model. This setup is further referred to as "plume-parameterizing". With this plume-resolving setup, the sensitivity of both sensible heat and moisture release on the aerosol evolution is investigated and the results are compared to the plume-parameterizing simulation.
In the next step the known issue of the systematical underestimation of the injection height and dynamic height range by the plume-rise model is addressed. Therefore, sensible heat and moisture released by the fire are implemented as perturbations in the meteorology in the plume-parameterizing setup. Additionally, the optical properties of biomass burning aerosol are implemented and the impact of aerosol-radiation interaction is analyzed, to answer the following research questions:

1. How does moisture and sensible heat release by the fire impact the plume height and pyro-convection in a convection-resolving setup and how does it differ from a parameterized plume height?

2. What is the impact of moisture and sensible heat release by the fire on the plume evolution and cloud formation in a plume-parameterizing setup?

3. Does aerosol-radiation interaction induce a self-lofting of the plume within the first three days? And how does the semi-direct aerosol effect manifest itself?

In the following, the second chapter explores the fundamentals on fire-atmosphere interaction, including fire behavior, plume dynamics, and the impacts of vegetation fires on the atmosphere. The third chapter gives an overview of the Australian Black Summer Fires and the case study of this work. The fourth chapter contains a description of the ICON-ART model, the treatment of vegetation fires in the model and the modifications and implementations made in this study. The experiments are divided in three chapters. Chapter 5 shows the results of the plume-resolving simulations. Chapter 6 analyzes the plume-parameterizing experiments and chapter 7 compares the results of chapter 6 with observations. Chapter 8 contains the conclusions and outlook of this work.

2. Fundamentals on fire-atmosphere interaction

2.1. Fire behavior and plume dynamics

Fire in a physicochemical sense is the release of energy via the oxidation of chemical compounds (Bradstock et al., 2012). According to Bradstock et al. (2012) this process is often summarized as the "fire triangle" consisting of oxygen, fuel availability and sufficient heat as the key parameter to enable combustion. Fire characteristics like fire spread, fuel consumption, heat release, plume production and smoke dispersion are driven by the composition, structure and condition of the fuel, the weather and the topography. Fuel in general describes the combustible material, in terms of vegetation fires, fuel refers to the composite of dead and live vegetation. Vegetation fires are often described by the predominant fuel type (e.g. grass fire, forest fire, peat fire), although the fuel often is a composite of different vegetation types. Figure 2.1 illustrates the different fuel layers in a typical forest. Surface fuels are the most flammable and comprised of fallen leaves, bark, twigs and dead vegetation in general. Usually, this layer provides the most energy release and is the first to ignited. Near surface fuels are comprised of grass, shrubs, creepers and collapsed understory and can vary in height from a few centimeters to over a meter. Elevated fuels consist of shrubs and regenerating vegetation. The height and density of this layer governs the flame dimension. Fires in the canopy are a common source of firebrands, material that is lofted and transported by the fire's convection. Firebrands have a high potential of igniting unburned vegetation in considerably distance from the fire. The ignition through firebrands is called "spotting" (Bradstock et al., 2012).

The combustion process takes place in three main phases: ignition, flaming and smoldering. The burning of small vegetation pieces (leaves, twigs, needles) is described as ignition phase. In this phase, the radiant heating of larger pieces and thus the evaporation of water vapor takes place, which enables ignition. In the flaming phase larger pieces (e.g. branches) combust. Hydrocarbons volatilize in the flame due to the thermally decomposing biomass mixed with air during rapid oxidation (Koppmann et al., 2005). Flaming combustion is followed by smoldering combustion, which begins when most volatiles are expelled from the cellulose fuel.

The section of a fire burning downwind is called head fire and it is characterized by tall flames, rapid incomplete combustion, dark smoke and fast burning consistent with the wind speed. Fires spreading against the wind are called back fires and are characterized by shorter flames, a more complete combustion and whiter smoke. The right and left side of a fire is referred to as flank fire. A schematic visualization is given in 2.2. In contrast to the fuel, the effects of weather and topography on fire behav-

ior are similar for all vegetation types (Liu et al., 2022). Weather that favors wildfires is also referred to as "fire weather", and primary refers to the meteorological variables wind, rainfall, temperature, relative humidity and solar radiation. The meteorological conditions govern water vapor transfer into and out of dead vegetation and therefore the short-term fuel moisture content. High temperatures, little rainfall and very low relative humidity, less than approximately 20 %, favor fuel evaporation, and therefore dry the fuels out. Drier fuels are more flammable and less energy is needed for ignition (Bradstock et al., 2012). Wind affects vegetation fires directly. Strong winds fan the fires and increase the spread of the fire front, as all fires burn fastest in the direction of the wind. Passing cold fronts and turbulent eddies can change the wind direction, hence spread the fire band (Bradstock et al., 2012). The diurnal cycle in solar radiation, temperature and humidity creates a cycle in the dead fuel moisture content, lowest in the afternoon. Additionally, wind speeds tend to peak in the afternoons, which increases the fire spread and intensity. During the night the fire activity decreases and reaches a minimum in the early mornings. Atmospheric instability makes fire behavior less predictable; convection is favored and this allows long distance spotting, starting new fires in considerable distance from the source (Roberts et al., 2009). Topography can impact the fire spread in different ways. Rocky slopes and drainages can act as fire breaks, due to the lack of fuel or moist fuel. The elevation and slope impact the ignition probability due to the temperature and moisture characteristics of the land. For example, a north-facing slope will heat up and dry out slower than a south facing slope. Lastly, fires spread faster uphill. Upcoming fuels are heated and dried out by the hot rising air from the fire downhill. The updrafts are likely to create spot fires (Bradstock et al., 2012).

Pyro-convection

Extreme wildfire events can violently disturb the atmospheric stability and create convective and thunderstorm-like clouds. These are referred to as pyro-Cu or pyro-Cb for ice capped cumulonimbus convection with lightning present. The prerequisite for this phenomenon is the overlap of regional fire activity with a conductive background meteorology. Ideal meteorological conditions for pyro-Cbs are a dry, well-mixed lower layer, beyond a moist middle troposphere (Cunningham and Reeder, 2009; Fromm et al., 2012; Rosenfeld et al., 2007). This atmospheric layering also favors downbursts when precipitation from the moist middle troposphere evaporates in the dry layer. These meteorological conditions typically occur during the local afternoon and evening when atmospheric instability reaches a maximum. The overlap of these conditions and vigorous fires generally limits pyro-Cbs to summertime fire seasons. The air parcel above the fire is induced with trace gases of the combustion including moisture and aerosols. It is further exposed to strong heating and therefore becoming positively buoyant.
The high concentrations of smoke particles, which act as CCN and INP, make the pyro-convective clouds precipitation-poor and reduce aerosol washout. It is often observed that aerosols entrain at the cloud base and detain at the top (Andreae et al., 2004; Reid et al., 1998a). The rapid updrafts in the cloud result in a rapid airflow towards the updraft base, this feeds the flaming fire and enables entrainment, feeding the

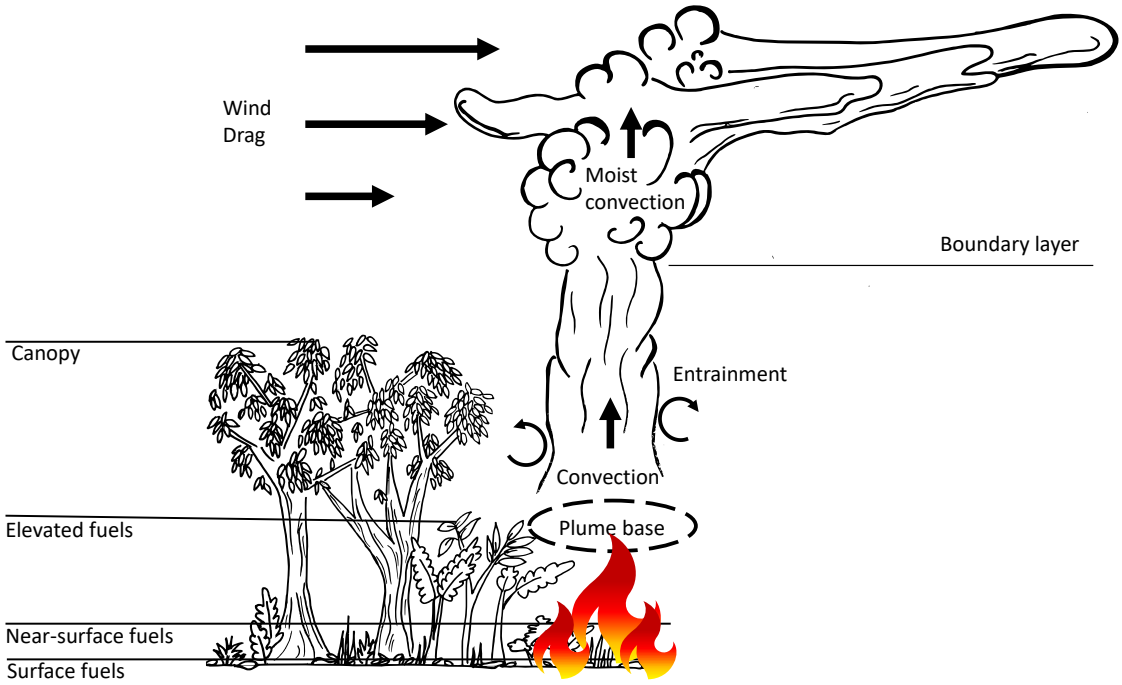

Figure 2.1.: Schematic illustration of the different categories of fuel strata present in a forest and the physical processes involved in fire plume dynamics adapted from Bradstock et al. (2012) and Paugam et al. (2016).

cloud with the moisture of surrounding air (figure 2.1). This creates a positive feedback loop (Fromm et al., 2006; Rosenfeld et al., 2007; Trentmann et al., 2006). Such conditions can lead to the formation of pyro-Cbs that reach the free troposphere or even penetrate through the tropopause into the lower stratosphere. It is often observed that pyro-Cbs result from multiple fires in close proximity, creating several updrafts. The phenomenon only lasts for a couple hours (Tory and Kepert, 2021).

2.2. Impact of fires on the atmosphere

2.2.1. Moisture release

The moisture released by the fire can be divided in two categories: combustion moisture and fuel moisture. Combustion moisture is chemically produced during the combustion process. Vegetation burned during wildfires typically consist of cellulose and hemicellulose, these are complex carbohydrate and polysaccharide and are the main parts of the of the cell wall. Cellulose and hemicellulose make 50-65 % of the vegetation fuel. Lignin (16-35 % of the fuel) is a complex non-carbohydrate polymer, which binds to cellulose fibers and strengthens the cell walls. 0.2-15 % of the fuel consists of mineral tracers and extractives, organic species (not part of the cellular structure) that are dissolved or outgassed during the combustion process (Koppmann et al., 2005; Simoneit, 2002). Complete combustion forms carbon dioxide and water along with other less prominent oxides. Combustion of cellulose rich vegetation ($C_6H_{10}O_5$ and $C_5H_8O_4$) produces around 0.8 molecules H_2O per molecule CO_2. Lignin compositions are more variable but can be assumed to be $C_6H_{6.4}O_2$ in average and the combustion releases 0.53 molecules H_2O

for each molecule CO_2. For an average biomass a ratio of 0.75 H_2O/CO_2 is a valid assumption (Parmar et al., 2008).

Water vapor, that is released additionally is considered fuel moisture. Fuel moisture content is the water stored in biomass in relation to its dry mass and is one of the primary variables to determine the fire risk and fire behavior in fire models. The fuel moisture has a strong impact on the ignition probability, combustion, available fuel, fire spread and smoke generation (Anderson et al., 2011). The release of fuel moisture is not limited to the combusting fuel but also extended to the surrounding fuels, which are dried by the heat of the fire. The energy sink of evaporation near the fire often serves as an energy source through condensation in higher altitudes (Potter, 2005). Fuel moisture is divided between live fuel and dead fuel. Dead fuel moisture is dependent on the meteorological conditions (temperature, relative humidity, wind and radiation), diameter of the material and biochemical compositions (Fiorucci et al., 2007). Dead fuels can exchange water with the atmosphere by condensation, adsorption of water vapor or precipitation, desorption and evaporation (Viney, 1991). The live fuel moisture content depends on the species-specific attributes like rooting depth and drought adaption strategies (Nolan et al., 2016).

The moisture in the plume is visually a combination of evaporated fuel moisture, a by-product of cellulose combustion, and entrainment from the ambient atmosphere. The strong buoyancy caused by the fire in combination with sufficient moisture in the smoke plume can lead to cloud formation and thus to the release of latent heat, which increases the buoyancy of the smoke plume.

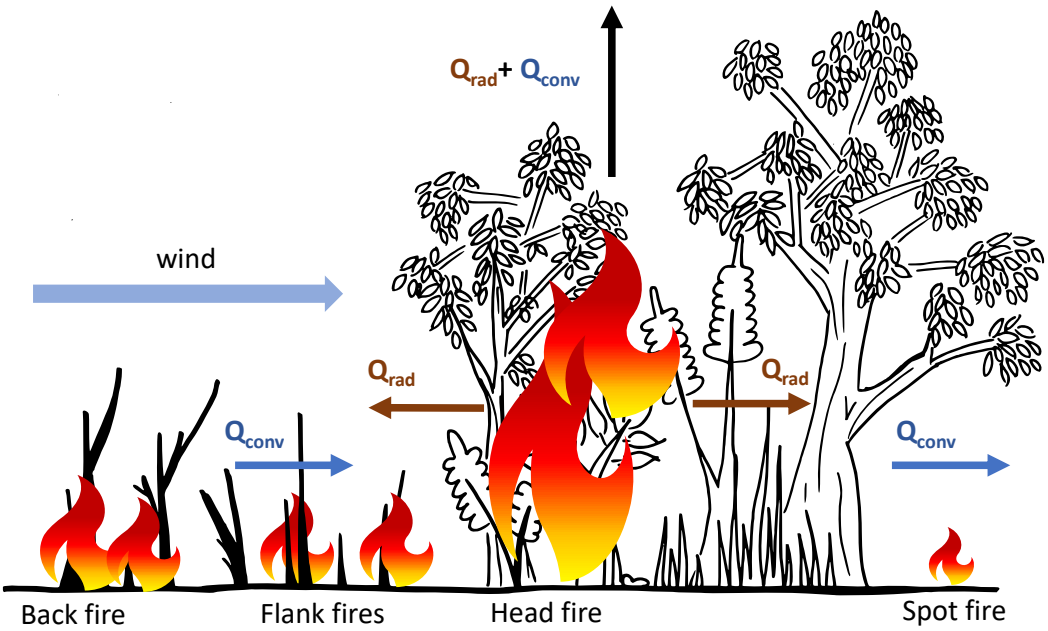

Figure 2.2.: Schematic illustration of heating fluxes and fire spread according to Lattimer (2019) Q_{conv} displays the convective heat transfer and Q_{rad} displays the radiative heat transfer.

2.2.2. Heat release from the fire

Heat release and heat transfer play an important role in the fire spread, ignition and plume rise. The heat transfer can occur through convection and radiation (Lattimer, 2019) and depends on the wind conditions, terrain slope and vegetation type. The wind velocity increases the heat transfer from the fire to the unburned fuels, this increases the rate of ignition and burning. Figure 2.2 illustrates the different heat transfer types in a schematic illustration of a spreading fire front. Radiative heating by the spreading front favors ignition of the vegetation ahead. In the flame region convection and radiation determine the heat release rate. The exchange of heat between the understory and the canopy affects the ignition of fuel and spread.

The heat released is modulated by three processes. First, conduction is the energy required to mechanically drive the fire and evaporate moisture from the fuels. Second, the endothermic energy needed to heat the fuel to ignition temperature and last, the initiation of self-sustaining chemical reactions. This outlines that radiative heating is a driving factor for the fire dynamics and convective heating determines the buoyancy of the plume. The relationship between radiative and convective heat transfer remains with uncertainties, as heat transfer depends on the type of vegetation, moisture content and topography. (Lattimer, 2019). Studies from Freeborn et al. (2008) and McCarter and Broido (1965) calculate a mean convective fraction of 55 % and 51.8 %. Radiant fractions of the total energy released from the fire between 10-20 % are proposed by Freeborn et al. (2008), Ke et al. (2021), and Val Martin et al. (2012).

2.2.3. Biomass burning emission products

Besides impacting atmospheric variables directly through heat and moisture, there is also a variety of gaseous and particulate tracers emitted to the atmosphere by wildfires. The emission of those depends on the fuel type and the combustion phase. If the combustion is complete, the chemical products are carbon dioxide and water. Incomplete combustion additionally emits carbon methane and nitrous oxide, nitric oxide, carbon monoxide and volatile organic compounds (VOC) (Nussbaumer, 1989). The composition and amount of gaseous emission are further impacted by the cause of fire, oxygen supply, temperature and elementary composition of the fuel (Marutzky, 1991).

Biomass burning aerosols

Besides gaseous emissions, "soot-like" particles and liquid aerosols, so called polycyclic aromatic hydrocarbons (PAH) are emitted during the combustion process. According to Reid et al. (2005b) these particles are qualitatively well understood. The particles have a variety of morphologies: chain aggregates, solid irregulars and more liquid/spherical shapes. The physical and chemical composition is strongly variable and depending on the fuel type, moisture, combustion phase, wind conditions and age of the particles. In the flame zone, black carbon chains rapidly aggregate and age due to the condensation

of low vapor pressure organics or through coagulation. This forms semi-spherical/semi-liquid droplets with solid complex cores. Typical core-to-shell fractions are 0.33-0.66 in diameter and 0.04-0.3 volume wise (Reid et al., 1998a). Further, there are widely varying reports of the particle density from 0.79 g cm^{-3} (Stith et al., 1981) to 1.53 g cm^{-3} (Reid et al., 1998a).

One major uncertainty is the particle size. There are numerous studies on this topic, looking at in situ measurements, laser spectroscopy, surface observations, field and laboratory studies, with largely varying results. There are numerous studies reporting a bi-modal size distribution for fresh and aged particles (Alonso-Blanco et al., 2014; Brock et al., 2021; Denjean et al., 2020; Fuzzi et al., 2007; Hodshire et al., 2019; McClure et al., 2020; Remer et al., 1998; Vestin et al., 2007; Wu et al., 2020). It is also shown that the size distribution depends on the particle lifetime. Laboratory studies of fresh particles report number size distributions between 30 nm and 160 nm (Hosseini et al., 2010; Levin et al., 2010). Reports of aged particles reach number diameters of 1150 nm (Cahill et al., 2008) but a majority of the number size distributions is between 100 nm and 400 nm (Chou et al., 2008; Denjean et al., 2020; Friedman et al., 2009; Hodshire et al., 2019, 2021; Janhäll et al., 2010; Kleinman et al., 2020; Ramnarine et al., 2019; Reid et al., 2005b; Sakamoto et al., 2015; Vestin et al., 2007). According to Reid et al. (2005b) a mean center for a monodisperse distribution can be set at 130 nm with a standard deviation around 1.7, although there is a considerable dependency on the fuel type and fire characteristics.

In terms of particle chemistry, there are three main components: organic materials, black carbon and trace inorganic species. The organic material, particulate organic matter (POM), is carbon associated with organic substances such as hydrogen (H), nitrogen (N), and oxygen (O) and makes up about 80 % of the particle mass. Black carbon or soot accounts for 5-9 % of the mass. Although there is no standard definition for black carbon, it is often defined as strongly light absorbing. Further, the trace inorganic species account for 12-15 % (Reid et al., 1998b).

The physical and chemical properties of biomass burning aerosols evolve over time. The driving factor in the development of the size distribution is coagulation due to the high aerosol concentrations in the cloud. (Andreae and Merlet, 2001). There are also reports on secondary organic aerosols in the plume, in chamber (Cubison et al., 2011; Ortega et al., 2013) and in field studies (DeCarlo et al., 2010; Reid et al., 1998b). These secondary aerosols either form through nucleation or condensation on existing particles. In addition, organic aerosol matter can evaporate during the dilution of the plume. Several studies show that biomass burning aerosol properties vary with plume age, combustion phase and fuel type (Hosseini et al., 2010; Janhäll et al., 2010). Therefore, it remains a challenge to constrain natural variability.

2.2.4. Radiative impact of biomass burning aerosols

"There are significant uncertainties in describing the optical properties of biomass burning aerosols, which are influenced by their composition, size, and mixing state. The aerosols affect the Earth's energy budget by scattering and absorbing solar and terrestrial radiation, and thereby modifying the radiative fluxes (Brown et al., 2021). In terms of optical properties the composition of the aerosols is often de-

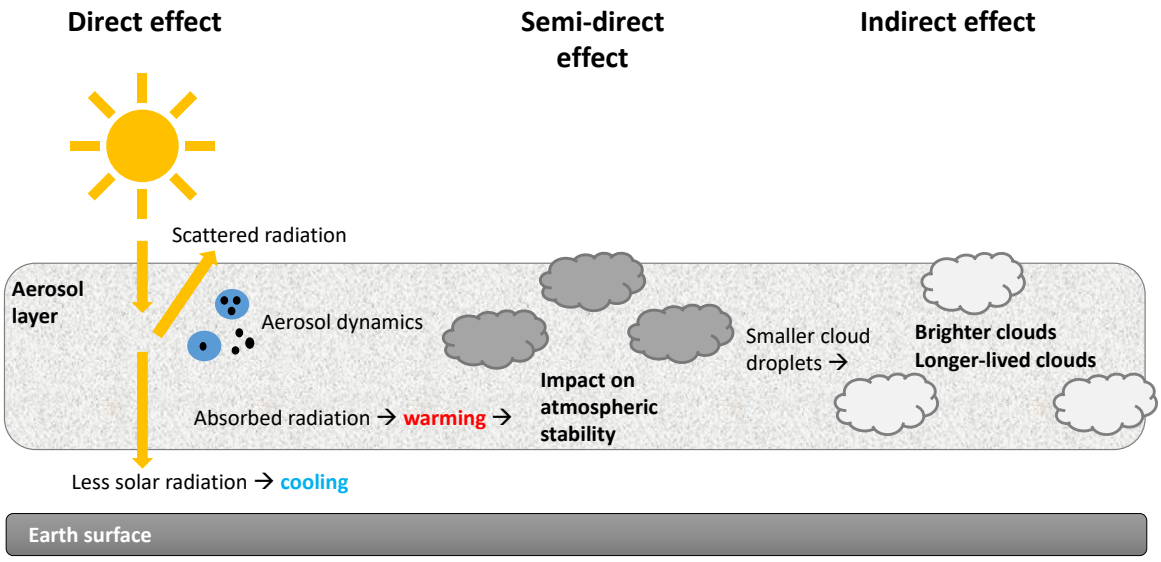

Figure 2.3.: Schematic illustration of aerosol–radiation interactions of incoming solar radiation, based on Bellouin and Yu (2022).

scribed by the ratio of organic carbon (OC) to black carbon (BC), the OC/BC ratio (Novakov et al., 2005). The radiation scattered and absorbed by the particles is strongly correlated with the particle size and BC content, which further depends on the individual fire physics and combustion phase. Aging processes affect the particle size and composition. For example, coagulation keeps the OC/BC ratio constant but increases mass scattering due to an increase in size alone (Reid et al., 2005a). Reid et al. (2005b) review reports on biomass burning optical properties, including in situ measurements, forward calculations and inversion studies. They conclude that with an average number size distribution of $d_n = 130$ nm and standard deviation $\sigma = 1.7$, a reasonable assumption for the refractive index is 1.5 ± 0.015i. Further, they recommend a mass absorption coefficient of 0.50 ± 0.15 m^2 g^{-1} and a single scattering albedo of 0.89 at a wavelength of 550 nm, well aware, that this recommendation represents an average value from which individual fires deviate considerably.

Brown et al. (2021) compare 12 observational data sets to nine state-of-the-art Earth system models/chemical transport models and conclude that current representations of biomass burning aerosols are too absorbing. It remains a challenge to find a general representation of the optical properties that fits individual fires.

The aerosol optical properties determine the effect on the Earth's radiation budget. Not all of the incoming solar radiation reaches the surface, some is reflected by clouds and some is absorbed and scattered by atmosphere. The same goes for the terrestrial radiation, large parts are absorbed and re-emitted by the atmosphere. Figure 2.3 displays how aerosols perturb the Earth's radiation budget. It is noteworthy

that vegetation fires affect the global radiation budget in numerous ways and the extent and magnitude is not yet fully understood (Sakaeda et al., 2011). Nevertheless, the effects can be categorized in the direct effect, the semi-direct effect and the indirect effect, as illustrated in figure 2.3.

The impact of scattering and absorption of radiation by aerosols on the Earth's radiation budget is referred to as the direct aerosol effect. The direct aerosol forcing is affected by cloud cover and the aerosol layer height. This is shown by Chang et al. (2021), Heinold et al. (2022), and Sellitto et al. (2022) for the Black Summer Fires. The radiative forcing at the top of the atmosphere is largest for aerosols above clouds, since it is depending on the albedo below the aerosol layer (Chand et al., 2009).

The absorptivity of the biomass burning aerosols leads to a spacial perturbation and redistribution of energy and therefore to changes in the surface energy budget, ground-surface flux exchange, atmospheric thermodynamic stability and finally cloud evolution (Liu et al., 2020). The last is referred to as semi-direct effect. The semi-direct aerosol effect describes a change in cloud cover or cloud water and ice path due to the aerosol-radiation interaction (Sakaeda et al., 2011). The magnitude and extent of the semi-direct effect is not clear and varies largely between different studies (Morgan et al., 2006). Biomass burning aerosols can further impact cloud microphysics. This is referred to as the indirect effect. Aerosols can act as CCN or INP and thereby change the cloud albedo and cloud lifetime. In addition, the release of latent heat resulting from internal microphysical processes can alter atmospheric stability and influence convection (Liu et al., 2020).

3. Australian Black Summer Fires

3.1. Role of fire in Australia

Vegetation fires in Australia are commonly referred to as "bushfires", therefore this terminology is used referring to vegetation fires in Australia. The exact role of fire in the evolution of Australia's environment is unclear, but with the Aboriginal colonization in the Late Pleistocene an additional fire source was introduced. Over generations, Aboriginals developed knowledge about the land, vegetation, and biodiversity. Traditional burnings are an Aboriginal cultural practice, which skillfully uses fire for the maintenance of the land (Gott, 2005). These burnings create a fine-grained mosaic of burned and unburned vegetation that is critical for the survival of a range of plants and animals, who are currently suffering from the abundance of this practice in most parts of Australia (Burbidge and McKenzie, 1989; Fisher et al., 2003; Fordyce et al., 1997; Franklin, 1999; McKenzie et al., 2007; Pardon et al., 2003; Russell-Smith and Bowman, 1992; Russell-Smith et al., 1998, 2002; Woinarski et al., 2001, 2010). The European colonization not only end Aboriginal burnings, but further influenced Australian fire regimes and vegetation by land clearances, introduction of large herbivores, and flammable and invasive plants. Additionally, climate change impacts fire regimes as it favors fire weather. This is shown for south-east Australia by Lucas (2005) and Williams et al. (2009). Therefore, it is expected that bushfires are likely to increase in intensity and frequency. The effect climate change might have on fuel characteristics is not clear. A decrease of water ability, which is predicted for south-east Australia, might reduce fuel production an accumulation, whereas increases in CO_2 concentrations may increase fuel availability (Bradstock et al., 2012). Australia has a great variety of vegetation, of which grassland, forest and mallee-heath are the three most fire-prone. Grasslands consist of native and introduced pastures and weeds that cover more than 75 % of Australia, often as an understory to other vegetation (Bradstock et al., 2012). Australian forests cover over 22 % of the continent, of which 78 % are dominated by eucalyptus. Mallee-heath fuels cover 2 % of the continent, throughout sandy areas in southern Australia. Mallee-heath is characterized by a spatially discontinuous fuel complex; therefore, fire spread is not supported without an elevated near-surface layer, expect for extreme fire weather conditions (Bradstock et al., 2012).

Any time of the year fires can occur in Australia due to different climates (as displayed in figure 3.1). Australia is divided in six main climate groups: equatorial, tropical, subtropical, desert, grassland and temperate with numerous subgroups (Figure 3.1). In the north the climate is determined by an annual monsoon season with a wet season from November-December till March-April. During the dry season the northern savanna is characterized by dry and sunny weather. This causes grass to die and the fuels

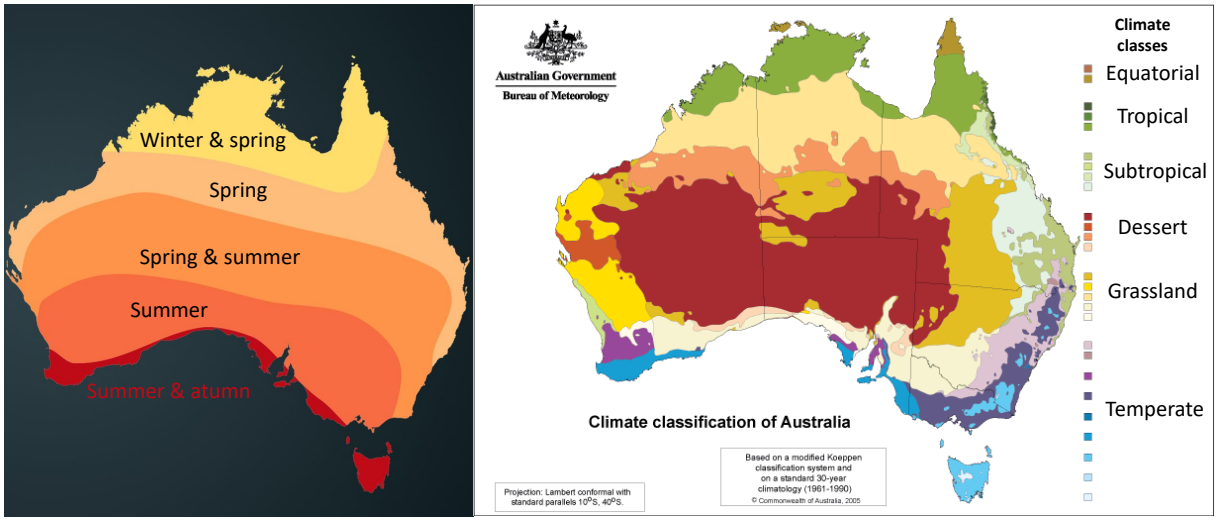

Figure 3.1.: Left: Fire seasons in Australia, adapted from Bureau of Meteorology (2020b). Right: Climate zones in Australia, based on a modified Köppen classification system, adapted from Bureau of Meteorology (2020c).

to dry paving the way for rapid burns. Intense high pressure systems over South Australia can increase the bushfire risk by the production of south-east to north-east winds. The highest fire risk from spring to summer occurs in New South Wales (NSW) and southern Queensland (QLD), where winters are typically dry. In southern Western Australia (WA), high fire risks arise when the fuel dries after winter rains. Further south, the fire season peaks during the summer months. Southern Australia's climate features warm to hot summers and cool winters, with the main rainfall occurring in spring and winter. Grass and forests dry out during the summer, making southeast Australia particularly vulnerable to bushfires. Interannual variability is linked to the El Niño Southern Oscillation (ENSO) and the Indian Ocean Dipole (IOD). El Niño years are generally associated with drier than average conditions, which favor bushfires.

3.2. Black Summer Fires

The therm "Black Summer Fires" commonly referrers to the Australian bushfire season 2019/2020. According to Morgan et al. (2020) this eight month fire period (from July to end of February) burned nearly twice the area of previous fire seasons. The Black Summer is labeled "unprecedented" because of its duration, intensity and spread. Morgan et al. (2020) outline that historical fires were confined to one or two states or territories, but the Back Summer Fires spread through multiple states. In terms of areas burned NSW was affected most with 5.68 million ha, followed by WA (2.04 million ha) and Victoria (VIC) (1.58 million ha). Across all states and territories 10.2 million ha were burned. 81% (8.19 million ha) of the burned area is categorized as native forest (Davey and Sarre, 2020). This makes 6% of

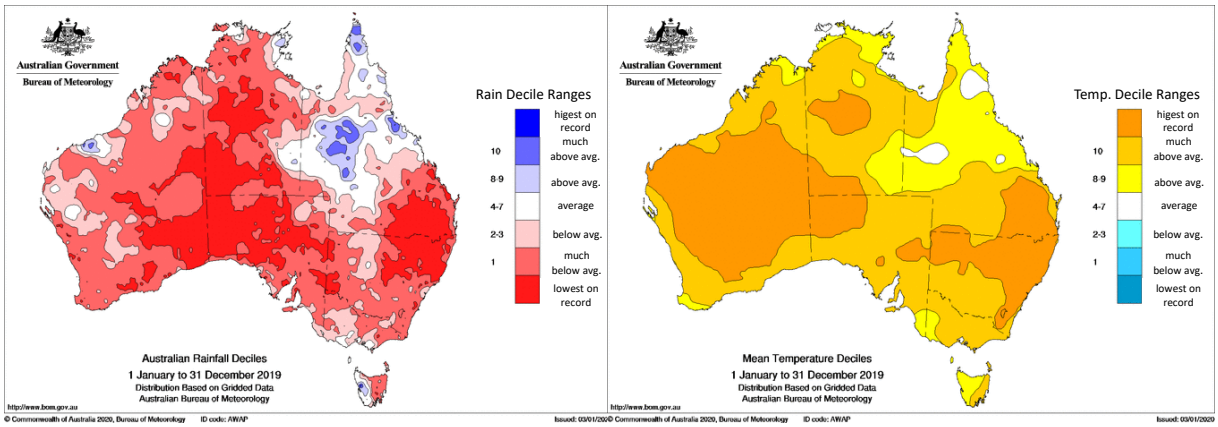

Figure 3.2.: Left: Mean temperature decile, right: Mean rain decile. source: Bureau of Meteorology (2020a).

Australia's total native forest. This severely affected Australia's biodiversity and caused tremendous loss in wildlife. The rest of the burned area is categorized as agricultural croplands and grasslands, forest plantations, peri-urban lands, native grasslands, and heath and scrub-lands. Moreover, these fires had major impacts on the rural communities due to property, farm and livestock losses and impacts on local tourism and economies. Further, smoke from the fires blackened Australian cities and communities for weeks. According to Borchers Arriagada et al. (2020) the Black Summer Fire smoke emissions has substantial social and ecological effects such as premature mortality and exacerbation of cardio-respiratory conditions. The health burden is estimated to 417 excess deaths, 1124 hospitalizations for cardiovascular problems, 2027 hospitalizations for respiratory problems and 1305 hospitalizations for asthma (Borchers Arriagada et al., 2020). This outlines the importance of good air quality forecasts so that measures, including warnings and evacuations, can be taken.

According to the Bureau of Meteorology (BOM), the summer of 2019/2020 has a very strong positive Indian Ocean Dipole (IOD). The IOD is a coupled ocean-atmosphere phenomenon caused by the difference in sea surface temperature between an area in the Arabian Sea (western Indian Ocean) and the eastern Indian Ocean south of Indonesia. A positive event is characterized by colder than usual sea surface temperatures (SST) in the east Indian Ocean. This decrease in temperature reduces convective heating and generates Rossby wave trains with a high pressure center south of Australia. This anomaly further causes dry conditions over southern and south-eastern Australia. During Australian springtime (September-October-November) the south and west of Australia experiences less than average rain fall due to intensifying and westwards shifting Rossby wave trains.

The year 2019 is the warmest year on record with area-averaged mean temperature of 1.53 °C above the mean temperature of 1962-1990. The annual mean temperatures were above average in nearly all of Australia, this is outlined by the figure 3.2. Figure 3.2 contains the mean temperature and rain deciles. This means that the historical observations are arranged in ascending order and split in 10 equally sized groups. The color bar indicates the groups and the ranging accordingly. Figure 3.2 also shows that 2019 is the driest year on record, with below average rainfall in most parts of Australia and a national average rainfall that is 40 % below the 1961-1990 mean of 465.2 mm. The southern half of Australia was particularly dry in the second half of the year. The warm and windy conditions led to several periods of severe fire weather, resulting in these large bushfires from September onward, lasting till the February 2020.

Weather condition around the Australian New Years event

This section provides an overview of the meteorological conditions for the Australian New Year event (ANY). Over New Years 2019, another heatwave affects the south-east Australia. Figure 3.3 displays the mean sea level pressure in hPa for the 00:00 UTC on December 29th, 30th, 31st and 1st January 2019/2020 and shows a pre-frontal trough and a cold front passing over south-east Australia. The temperature rises above 40°C and high wind speeds are observed ahead of the front. A high-pressure system in the Tasman Sea moves hot and dry air masses from the northwest to the southern states. This promotes the drying of fuel, creating even more dangerous fire weather conditions. The cold front passing over fire regions elevates the wind speeds and also changes the wind direction in some fire regions. This

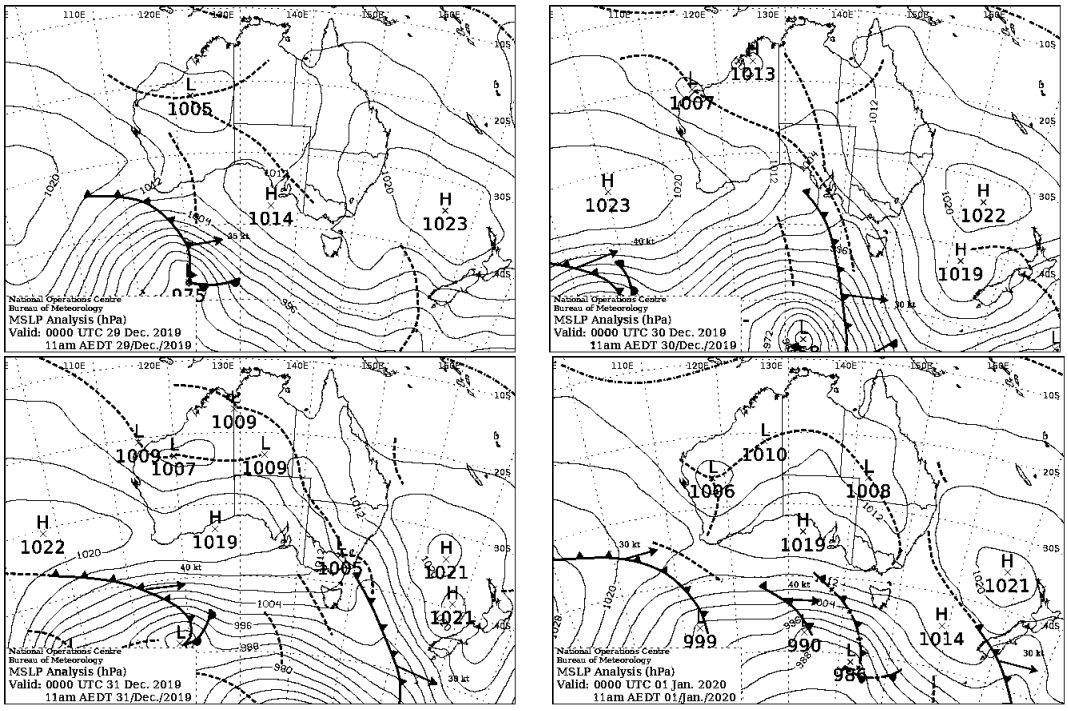

Figure 3.3.: Mean Sea Level Pressure left to right on the 29th, 30th, 31st of December 2019 and 1st of January 2020 at 00:00 UTC, source: Bureau of Meteorology (2022).

transforms the flank of the bushfire to a broader head fire and increases the fire spread. Along with the frontal system comes atmospheric instability and a tongue of mid-level moisture, favoring thunderstorm activity. This leads to a multi-day outbreak of pyro-Cb. 18 pyro-Cbs are reported between the 29th of December 2019 and 4th of January 2020. This outbreak injects approximately 1.0 Tg of biomass burning aerosol into the lower stratosphere (Peterson et al., 2021). Further, Fox-Hughes (2023) identifies a negatively tilted upper troposphere tough (axis oriented southwest–northeast), which, in conjunction with the surface pressure front, reinforces the vertical movements that are already present as the northwesterly airflow passes over south-eastern Australia. Fox-Hughes (2023) further reports low-level jets and down slope winds that increases fire activity.

4. Model description and extension

In the following chapter the numerical weather prediction (NWP) model ICON and the aerosol module ART are described in detail. Some theoretical background on aerosol-radiation interaction is given and a further focus is set on the treatment of biomass burning emissions and the modifications and implementations done in this work are explained.

4.1. The ICON modeling system

ICON stands for ICOsahedral Non-hydrostatic model and is a NWP model developed by the German Weather Service (DWD) and the Max Plank Institute for Meteorology (MPI-M), later joined by the German Climate Computing Center (DKRZ), the Karlsruhe Institute of Technology (KIT), and the center for Climate Systems Modeling (C2SM). ICON is the state-of-the-art NWP model and operationally used at DWD. It can be applied for seamless simulations from local to global scales (Giorgetta et al., 2018; Zängl et al., 2015). Special features of the model are the exact local mass conservation, mass consistent tracer transport, a flexible grid nesting capability and the use of non-hydrostatic equations on the global domain. The ICON grid is unstructured and triangular. The grid base is a 20-sided spherical icosahedron, which is refined in two steps. The root division step, which divides the arcs of the base triangle into n equal arcs, and the bisection step, which divides each triangle into 4 smaller triangles (Zängl et al., 2015). The ICON equation system follows compressible non-hydrostatic equations by Gassmann and Herzog (2008). It describes the atmosphere as a two-component system, consisting of dry air and water, latter can occur in all three phases. According to Wacker et al. (2006) partial densities are introduced to sum up the total density of the atmospheric mixture. A reference velocity vector is introduced, which is defined as a weighted mean to the governing equations (equations 4.1-4.5). Further, the Hesselberg averaging is applied on the equation set to separate turbulent fluctuations from the mean flow. This leads to the following equations:

$$\frac{\partial \widehat{v}_\mathrm{n}}{\partial t} + \frac{\partial \widehat{K}_\mathrm{h}}{\partial n} + (\widehat{\zeta} + f)\widehat{v}_\mathrm{t} + \widehat{w}\frac{\partial \widehat{v}_\mathrm{n}}{\partial z} = -c_\mathrm{pd}\widehat{\theta}_v \frac{\partial \overline{\pi}}{\partial n} - D_{\widehat{v}_\mathrm{n}} \tag{4.1}$$

$$\frac{\partial \widehat{w}}{\partial t} + \widehat{\boldsymbol{v}}_\mathrm{h} \cdot \nabla \widehat{w} + \widehat{w}\frac{\partial \widehat{w}}{\partial z} = -c_\mathrm{pd}\widehat{\theta}_v \frac{\partial \overline{\pi}}{\partial z} - g - D_{\widehat{w}} \tag{4.2}$$

$$\frac{\partial \overline{\rho}\,\widehat{\theta}_v}{\partial t} + \nabla \cdot (\overline{\rho}\widehat{\boldsymbol{v}}\widehat{\theta}_v) = \overline{Q} - D_{\widehat{\theta}_v} \tag{4.3}$$

$$\frac{\partial \overline{\rho}}{\partial t} + \nabla \cdot (\overline{\rho}\widehat{\boldsymbol{v}}) = 0 \tag{4.4}$$

$$\frac{\partial \overline{\rho}\widehat{q}_k}{\partial t} + \nabla \cdot (\overline{\rho}\widehat{q}_k\widehat{\boldsymbol{v}}) = -\nabla \cdot (\overline{\boldsymbol{J}_k} + \overline{\rho q_k'' \boldsymbol{v}''}) + \overline{\sigma_k} \tag{4.5}$$

Table 4.1.: Summary of variables used in the ICON equation system, adapted from Prill et al. (2022).

Symbol	Description	Unit
$\widehat{v}_\mathrm{n}$	perpendicular horizontal wind component	m s^{-1}
$\widehat{K}_\mathrm{h}$	horizontal component of the kinetic energy	m^2 s^{-1}
$\widehat{\zeta}$	vertical vortictiy component	s^{-1}
f	Coriolis parameter	s^{-1}
$\widehat{v}_\mathrm{t}$	tangential horizontal wind component	m s^{-1}
$\widehat{w}$	the vertical wind component	m s^{-1}
c_pd	specific heat capacity for dry air at constant pressure	J kg^{-1} K^{-1}
$\widehat{\theta}_v$	virtual potential temperature	K
π	Exner function	
$D_{\widehat{v}_\mathrm{n}}, D_{\widehat{w}}, D_{\widehat{\theta}_v}$	turbulent momentum fluxes	m s^{-2}
$\widehat{\boldsymbol{v}}_\mathrm{h}$	horizontal wind vector	m s^{-1}
g	gravitational acceleration	9.81 m s^{-1}
$\widehat{\boldsymbol{v}}$	three-dimensional wind vector	m s^{-1}
$\overline{\rho}$	air density	kg m^{-3}
$\overline{Q}$	diabatic heat source	kg K m^{-3} s^{-1}
$\widehat{q}_k$	mass fraction	
k $\in \{d, v, c, i, r, s, g\}$	dry air, water vapor, cloud water, cloud ice, rain, snow, graupel	
$\overline{\boldsymbol{J}_k}$	vertical diffusion flux for constituent k	kg m^{-2} s^{-1}
$\overline{\sigma_k}$	internal conversion rate for the kth constituent	kg m^{-3} s^{-1}

This equation system consists of the horizontal and vertical momentum equation (equations 4.1 and 4.2), the first law of thermodynamics (equation 4.3), the continuity equation (equation 4.4) and the continuity equation of the included constituents (equation 4.5). The prognostic variables are the horizontal wind velocity component normal to the triangle edges $\widehat{v}_\mathrm{n}$, the vertical wind component $\widehat{w}$, the density of the total air mixture $\widehat{\rho}$, the virtual potential temperature $\widehat{\theta}_v$, and the mass of the included constituents $\widehat{q}_k$. A further description of the terms is given in table 4.1. In the equation system the Reynolds average ($\phi = \overline{\phi} + \phi'$) and the barycentric mean ($\phi = \widehat{\phi} + \phi''$) are used. In ICON the computation of advection is divided into horizontal and vertical advection. This makes the computation more efficient and exact, compared to the calculation of three-dimensional advection. Further, local mass conservation is accomplished by using $\widehat{\rho}$ and $\widehat{\theta}_v$ in flux form (Rieger et al., 2015). The prognostic equation for the density of dry air is not solved

explicitly, but the prognostic equations for the total density and all but one partial density are solved. On this base the density of dry air is diagnosed. The wind velocity components (u, v, w) of the three-dimensional wind vector are assumed to form a right handed system consisting of a normal component, a tangential component and a vertical component.
Processes in ICON have different numerical stability criteria and therefore ICON makes use of the splitting approach and divides between the dynamical core and tracer advection. A schematic display is given in section 4.5 in figure 4.3 (including the implementations of this work). For the air continuity equation solved in the dynamical core the maximum time step is limited to the speed of sound, whereas the maximum time step for the tracer contiguity equation is limited by the wind speed. Therefore, longer time steps are used for tracer transport and physical parameterizations. Mass consistent tracer transport is achieved by transporting time averaged mass fluxes. It is further divided between fast a slow physics. The latter accounts for convection, cloud cover, radiation, non-orographic wave drag and sub-grid scale orographic drag and is assigned to a third even longer time step. Slow physics then pass tendencies to the dynamic core instead of updating the atmospheric state directly.

4.2. ART module

The ART (Aerosol and Reactive Trace gases) module is an ICON submodule embedded in the official ICON code, and mainly developed at the KIT. The ART module allows the simulation of aerosol emission, transport and removal, gas phase chemistry, aerosol dynamics, aerosol-radiative effects and the impact on clouds (Rieger et al., 2015; Schröter et al., 2018; Weimer et al., 2017). ART considers a variety of aerosols: mineral dust, pollen, volcanic aerosols, sea salt, anthropogenic aerosols and aerosols from biomass burning. It further contains chemistry descriptions for the troposphere and stratosphere as well as aerosol chemistry and dynamics. As explained in the previous section, the ICON model uses a time split method, this is also applied for ICON-ART. Here, the tracer mass fluxes are temporally averaged before entering the transport scheme in the dynamical core. The barycentric mean with respect to the air density ρ_a is used for the treatment of aerosol and gas tracers indicated with a hat. Ψ thereby is a mass specific variable. The Reynolds average is indicated with a bar and the fluctuations are indicated with two apostrophes.

$$\widehat{\Psi} = \frac{\overline{\rho_a \Psi}}{\overline{\rho_a}} \tag{4.6}$$

$$\Psi'' = \Psi - \widehat{\Psi} \tag{4.7}$$

The total time derivative and the continuity equation are given by:

$$\widehat{\frac{\mathrm{d}}{\mathrm{d}t}} = \frac{\partial}{\partial t} + \widehat{\boldsymbol{v}} \cdot \nabla \tag{4.8}$$

$$\widehat{\frac{\mathrm{d}\overline{\rho_a}}{\mathrm{d}t}} = -\overline{\rho_a} \nabla \cdot \widehat{\boldsymbol{v}} \tag{4.9}$$

4.2.1. Gaseous tracers

In ICON-ART gaseous tracers are treated according to Rieger et al. (2015) as their barycentric averaged mass mixing ratio $\widehat{\Psi}_{g,l}$, the ratio of the partial density of a gas l (ρ_l) to the total density.

$$\widehat{\Psi}_{g,l} = \frac{\overline{\rho_l}}{\overline{\rho_a}} \tag{4.10}$$

$$\underbrace{\frac{\partial\left(\overline{\rho_a}\widehat{\Psi}_{g,l}\right)}{\partial t}}_{\substack{\text{spatio-temporal evolution} \\ \text{of gas tracer}}} = \underbrace{-\nabla \cdot \left(\widehat{\boldsymbol{v}}\overline{\rho_a}\widehat{\Psi}_{g,l}\right)}_{\text{advection flux}} \underbrace{-\nabla \cdot \overline{\rho_a \boldsymbol{v}'' \Psi''_{g,l}}}_{\substack{\text{turbulent} \\ \text{flux}}} + \underbrace{P_l}_{\substack{\text{chemical} \\ \text{production}}} - \underbrace{L_l}_{\substack{\text{chemical} \\ \text{loss}}} + \underbrace{E_l}_{\text{emission flux}} \tag{4.11}$$

The spatio-temporal evolution of gas tracers is given in flux form in 4.11. It depends on the advection flux, the turbulent flux, the chemical production and loss and the emission flux.

4.2.2. Aerosol tracers

In ICON-ART aerosols are described in different size modes. Each size mode is represented by a two-moment modal formulation, with the kth moment. This "two-moment"-scheme treats number concentration and mass mixing ratio as two prognostic variables per mode. The specific number concentration $\widehat{\Psi}_{0,l}$ and the mass mixing ratio $\widehat{\Psi}_{3,l}$ represent the zeroth (k = 0) and third (k = 3) moment for a specific mode l and are given by Hesselberg average in the following equations:

$$\widehat{\Psi}_{0,l} = \frac{\overline{\rho_a \frac{N_l}{\rho_a}}}{\overline{\rho_a}} = \frac{\overline{N_l}}{\overline{\rho_a}} \tag{4.12}$$

$$\widehat{\Psi}_{3,l} = \frac{\overline{\rho_a \frac{M_l}{\rho_a}}}{\overline{\rho_a}} = \frac{\overline{M_l}}{\overline{\rho_a}} \tag{4.13}$$

N_l describes the number of particles and M_l the particle mass of mode l. ART uses log-normal distributions to describe the aerosol size distribution. The log normal distributions are given by:

$$\widehat{\psi}_{0,l}(\ln d_p) = \frac{\Psi_{0,l}}{\sqrt{2\pi}\ln\sigma_l} \exp\Big(-\frac{(\ln d_p - \ln d_{0,l})^2}{2\ln^2\sigma_l}\Big) \tag{4.14}$$

$$\psi_{3,l}(\ln d_p) = \frac{\widehat{\Psi}_{3,l}}{\sqrt{2\pi}\,\ln\sigma_l}\exp\Big(-\frac{(\ln d_p - \ln d_{3,l})^2}{2\,\ln^2\sigma_l}\Big) \tag{4.15}$$

for the specific number concentration (equation 4.14) and the mass mixing ratio (equation 4.15). Both are functions of the particle diameters d_p, the standard deviation σ_l and the median diameter of the mode l: $d_{0,l}$ and $d_{3,l}$. The median diameter of an aerosol population can then be expressed by:

$$\ln d_{3,l} = \ln d_{0,l} + 3\,\ln^2\sigma_l \tag{4.16}$$

This finally leads to the transport equations of the Hesselberg averaged specific number concentration and mass mixing ratio given in equations 4.17 and 4.18.

$$\begin{aligned}\underbrace{\frac{\partial(\overline{\rho_a}\widehat{\Psi}_{0,l})}{\partial t}}_{\text{spatio-temporal evolution}} &= -\underbrace{\nabla\cdot(\widehat{\boldsymbol{v}}\overline{\rho_a}\widehat{\Psi}_{0,l})}_{\text{advection flux}} - \underbrace{\nabla\cdot\overline{\rho_a \boldsymbol{v}''\Psi''_{0,l}}}_{\text{turbulent flux}} - \underbrace{\frac{\partial}{\partial z}(v_{sed,0,l}\overline{\rho_a}\widehat{\Psi}_{0,l})}_{\text{sedimentation}} \\ &- \underbrace{W_{0,l}}_{\text{wet deposition}} - \underbrace{Ca_{0,l}}_{\text{coagulation loss}} + \underbrace{Nu_{0,l}}_{\text{nucleation}} + \underbrace{E_{0,l}}_{\text{emission}}\end{aligned} \tag{4.17}$$

$$\begin{aligned}\underbrace{\frac{\partial(\overline{\rho_a}\widehat{\Psi}_{3,l})}{\partial t}}_{\text{spatiotemporal evolution}} &= -\underbrace{\nabla\cdot(\widehat{\boldsymbol{v}}\overline{\rho_a}\widehat{\Psi}_{3,l})}_{\text{advection flux}} - \underbrace{\nabla\cdot\overline{\rho_a \boldsymbol{v}''\Psi''_{3,l}}}_{\text{turbulent flux}} - \underbrace{\frac{\partial}{\partial z}(v_{sed,3,l}\overline{\rho_a}\widehat{\Psi}_{3,l})}_{\text{sedimentation}} \\ &- \underbrace{W_{3,l}}_{\text{wet deposition}} - \underbrace{Ca_{3,l}}_{\text{coagulation loss}} + \underbrace{Nu_{3,l}}_{\text{nucleation}} + \underbrace{Co_{3,l}}_{\text{condensation}} + \underbrace{E_{3,l}}_{\text{emission}}\end{aligned} \tag{4.18}$$

In these equations $\widehat{\boldsymbol{v}}$ is the wind vector and $v_{sed,k,l}$ is the sedimentation velocity of the kth moment of mode l. Wet deposition in ICON-ART describes the scavenging of aerosols by raindrops below clouds. The nucleation of new particles is only relevant for the smallest Aitken mode and condensation of gaseous tracers on existing aerosols is only relevant for the 3rd moment. A more extensive description of the advection scheme and the turbulent flux is given by Rieger et al. (2015) and the references therein. Further details on the implemented sedimentation velocity can be found in Rieger et al. (2015) and Riemer (2002).

4.2.3. Aerosol dynamics

The aerosol dynamics module AERODYN in ICON-ART is introduced by Muser et al. (2020). The new aerosol module allows aerosol dynamic processes, namely nucleation, condensation, coagulation and the generation of internally mixed aerosols. Therefore, a new set of modes is introduced that diverges from previous studies by Hoshyaripour et al. (2019) and Rieger et al. (2015). As described in Muser et al. (2020) there are up to 10 log-normal modes, based on size (Aitken, accumulation and coarse mode) and mixing state (soluble, insoluble and mixed), visualized in figure 4.1. There is an additional insoluble

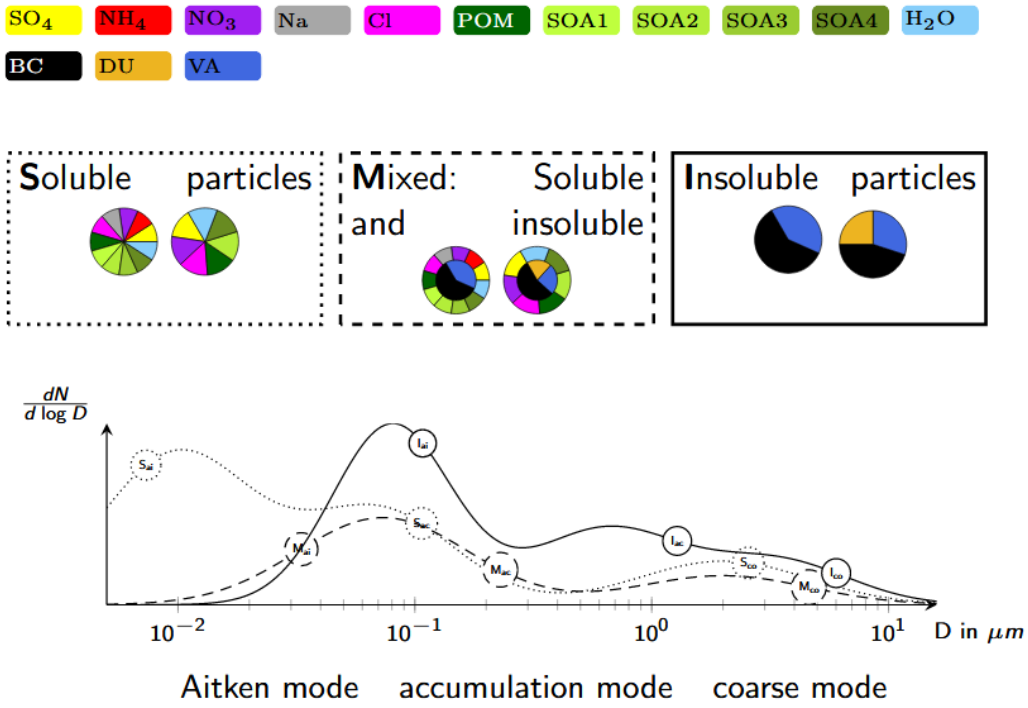

Figure 4.1.: Chemical composition of the soluble, mixed and insoluble modes and particle size distribution (giant mode is not shown). The dotted line represents a particle size distribution of soluble particles, the dashed line of mixed particles, and the solid line of insoluble particles. POM: primary organic matter, SOA: secondary organic aerosols, BC: black carbon. DU: desert dust, VA: volcanic ash. Upper panel adopted from Kaiser et al. (2014). Figure taken from Muser et al. (2020)

mode for the largest particles, the giant mode. These modes can be defined based on the particular application. The solubility of the particles is with respect to water. Soluble substances in ICON-ART are sulfate (SO_4^{-2}), ammonium (NH_4^+), nitrate (NO_3^-), sodium (Na+) and chloride (Cl^-), primary and secondary organic aerosols and water. The insoluble compounds are black carbon, dust and volcanic ash. Aerosol dynamic processes (condensation and coagulation) can combine soluble and insoluble compounds and form mixed particles. In ICON-ART these mixed particles consist of an insoluble core with a soluble shell (illustrated in the middle box in figure 4.1). The bottom of figure 4.1 displays the overlay of the different size distributions for the different modes and outlines the wide range of the particle sizes and mixing states. For each of these size distributions the prognostic number concentration and mixing ratio is calculated. Thereby, the standard deviation is kept constant, while the diameter of the k^{th} moment can change through the aerosol dynamic processes. The flexible design of the AERODYN module enables the user to specify which aerosol species and modes should participate in which process.

Gas-Particle partitioning with ISORROPIA II

ISORROPIA is a thermodynamic model that computes the physical state and composition of inorganic atmospheric aerosols (Nenes et al., 1998). An extension ISORROPIA II (Fountoukis and Nenes, 2007) is coupled with ICON-ART and used in Muser et al. (2020) for the calculation of gas-particle partitioning. ISORROPIA II treats the thermodynamics of inorganic K^+-Ca^{2+}-$Mg^{2+}$$NH_4^+$-$Na^+$-$SO_4^{2-}$-$NO_3^-$-$Cl^-$-$H_2O$ aerosol systems. It further calculates an equilibrium state for these species, namely potassium, sodium, magnesium, calcium, ammonium, sodium, sulfate, nitrate, chloride, water in the gas, liquid and solid phase. Several assumptions are made by Fountoukis and Nenes (2007) to make the model computationally efficient. One assumption is that H_2SO_4 has a low vapor pressure and therefore remains in the aerosol phase after condensation or nucleation. Further, the parameterizations for condensation and nucleation in ICON-ART are independent of ISORROPIA II.

Nucleation

In ICON-ART the nucleation parameterizations of sulfate particles is based on Kerminen and Wexler (1995), where particle nucleate once a critical concentration c_{crit} [μg m^{-3}] of H_2SO_4 is reached, which is given by

$$c_{crit} = 0.16 \exp\left(0.1T - 3.5 \frac{RH}{100} - 27.7\right) \tag{4.19}$$

with the temperature T in Kelvin and the relative humidity (RH) in %. If the H_2SO_4 concentration ($c_{H_2SO_4}$) is above c_{crit}, the excessive concentration nucleates into the soluble Aitken mode. A more detailed description is given by Riemer (2002).

Condensation

As described in section 4.2.3, the gas-particle partitioning for gaseous species is calculated with ISORROPIA II, but ICON-ART uses parameterizations based on Whitby and McMurry (1997) and modified by Riemer (2002) to calculate the condensation of H_2SO_4 onto existing particles. Growth by condensation generates no new particles, therefore, condensation only affects the third moment of the size distribution not the zeroth moment. The condensation rate $\tilde{C}o_{3,l}$ of the third moment in mode l is given by:

$$\tilde{C}o_{3,l} = \frac{6}{\pi}\chi_T \int_0^\infty \chi(d_l)\psi_l(d)\mathrm{d}d_l = \frac{6}{\pi}\chi_T I_l \tag{4.20}$$

I_l is an abbreviation for the integral.

The term χ_T depends solo on the thermodynamic variables and not the particle size and is given in equation 4.21, where M_w is the molar weight of the condensing gas, p_s is the saturation pressure, S_v is

the saturation ratio, ρ_{cond} the density of the condensing material, R^* the universal gas constant and T the temperature.

$$\chi_T = \frac{M_w p_s (S_v - 1)}{\rho_{cond} R^* T} \tag{4.21}$$

Equation 4.20 further contains the size dependent term $\chi(d_l)$, which is different for the near continuum (nc) and free-molecular regime (fm) and given in 4.22 and 4.23, respectively:

$$\chi_{nc}(d_{3,l}) = 2\pi D_{H_2SO_4} d_l \tag{4.22}$$

$$\chi_{fm}(d_l) = \frac{\pi \alpha \bar{c}_{H_2SO_4}}{4} d_l^2 \tag{4.23}$$

$D_{H_2SO_4}$ in equation 4.23 is the diffusion coefficient of H_2SO_4. α is the accommodation coefficient and $\bar{c}_{H_2SO_4}$ is the mean molecular velocity of H_2SO_4.
The size regimes are determinate by the dimensionless Knudsen number:

$$Kn_l = \frac{2\lambda_{air}}{d_l} \tag{4.24}$$

Here, λ_{air} stands for the mean free path of the ambient air. The different regimes are given in table 4.2

Table 4.2.: Size regime and corresponding Knudsen number (Kn)

Regime	Kn	
free-molecular (fm)	>10	free moving particle with respect to the air molecules
transition	1-10	
near-continuum (nc)	0.1-1	
continuum	<0.1	particle are considered suspended in air

With equations 4.22 and 4.23 the integral I_l in equation 4.20 can be written for the corresponding regimes as:

$$I_{l_{nc}} = 2\pi D_{H_2SO_4} M_{1,l} \tag{4.25}$$

$$I_{l_{fm}} = \frac{\pi \alpha \bar{c}_{H_2SO_4}}{4} M_{2,l} \tag{4.26}$$

$M_{k,l}$ responds to the kth moment of the particle size distribution. An I_l valid for all Knudsen regimes is composed of the harmonic mean:

$$I_l = \frac{I_{l_{nc}} I_{l_{fm}}}{I_{l_{nc}} + I_{l_{fm}}} \tag{4.27}$$

Therefore equation 4.20 can be written as:

$$\tilde{C}o_{3,l} = \frac{6}{\pi} \chi_T \frac{I_{l_{nc}} I_{l_{fm}}}{I_{l_{nc}} + I_{l_{fm}}} \tag{4.28}$$

It is assumed that the production rate of H_2SO_4 is much slower than its condensation. Therefore, an equilibrium state is reached in which the condensation rate equals the production rate of the third moment $\dot{M}_3$.

$$\tilde{C}o_3 = \sum_l \tilde{C}o_{3,l} = \dot{M}_3 \tag{4.29}$$

With this equation the mode dependent condensation rate can be written as:

$$\tilde{C}o_{3,l} = \dot{M}_3 \Omega_l \tag{4.30}$$

with the dimensionless coefficient:

$$\Omega_l = \frac{\tilde{C}o_{3,l}}{\tilde{C}o_3} = \frac{\tilde{C}o_{3,l}}{\dot{M}_3} = \frac{I_l}{\sum_l I_l} \tag{4.31}$$

The condensation rate is therefore independent of χ_T but depends on the integral I_l and the production rate of H_2SO_4. This corresponds to a condensed mass of:

$$Co_{3,l} = \frac{\pi}{6} \frac{\rho_{H_2SO_4}}{\rho} \dot{M}_3 \Omega_l \tag{4.32}$$

Here, ρ is the density of the aerosol. The production rate $\dot{M}_3$ is unavailable in ICON-ART and therefore, approximated by the H_2SO_4 concentration $c_{H_2SO_4}$ divided by the model time step Δt:

$$Co_{3,l} = \frac{c_{H_2SO_4}}{\Delta t} \Omega_l \tag{4.33}$$

Coagulation

The coagulation process increases the particle median diameter and reduces the number concentration. The parameterizations for the coagulation terms of the zeroth moment $Ca_{0,l}$ and third moment $Ca_{3,l}$ are based on Riemer (2002), who further references Whitby and McMurry (1997). The application in

ICON-ART is described by Muser (2022). ICON-ART differentiates between intra- and inter-modal coagulation, which means coagulation of particles in the same mode is treated differently than coagulation of particles from different modes. For intra-modal coagulation the resulting particles are assigned to the mode with the larger diameter. For inter-modal coagulation involving the mixed mode the resulting particles are assigned to the mixed mode with the larger diameter. For coagulation of insoluble and soluble particles the resulting particles remain in the insoluble mode, and if the soluble mode reaches a threshold of 5 % the particles are shifted into the mixed mode. This step is done in a separate routine following the coagulation routine.

$$Ca_{0,i} = Ca_{0,ii} + Ca_{0,ij} \tag{4.34}$$

$$Ca_{3,i} = Ca_{3,ij} \tag{4.35}$$

Equations 4.34 and 4.35 describe the coagulation rates for the zeroth and third moment, with $Ca_{0,ii}$ for intra- and $Ca_{0,ij}$ for inter-modal coagulation rates of the kth moment. Here, i and j represent two different modes. Intra-modal coagulation reduces the zeroth moment of the size distribution, but the third moment stays the same. Inter-modal coagulation changes the zeroth and third moment depending on the mixing state and size of the mode i and j. For example, the zeroth moment of the lager mode stays constant during a coagulation process with different sizes, whereas the third moment increases. For the smaller mode the zeroth and the third moment decrease accordingly. The changes for coagulation with different mixing states derive analogously. In ICON-ART only the coagulation due to Brownian motion is considered and electrostatic forces are neglected. The coagulation rate follows Whitby and McMurry (1997) and is valid for a coagulation system with the two modes i and j:

$$Ca_{0,ii} = \frac{1}{2}\int_0^\infty \int_0^\infty \beta(d_1,d_2)\psi_{0,i}(d_1)\psi_{0,i}(d_2)\mathrm{d}d_1 d_2 \tag{4.36}$$

$$Ca_{0,ij} = \int_0^\infty \int_0^\infty \beta(d_1,d_2)\psi_{0,i}(d_1)\psi_{0,j}(d_2)\mathrm{d}d_1 d_2 \tag{4.37}$$

$$Ca_{3,ij} = \int_0^\infty \int_0^\infty d_1^3\beta(d_1,d_2)\psi_{0,i}(d_1)\psi_{0,j}(d_2)\mathrm{d}d_1 d_2 \tag{4.38}$$

For $\psi_{0,l}$ a log-normal distribution is assumed. Here, β is the coagulation coefficient, which is dependent on the particle size. ICON-ART uses analytic solutions of the integrals given in equations 4.36 to 4.38 for the near-continuum and free-molecular regime, which are proposed by Whitby and McMurry (1997). A detailed derivation is given in Whitby and McMurry (1997). A harmonic mean is applied to depict the full-size range. Equations 4.39 and 4.40 show the harmonic means for inter-modal coagulation for the zeroth and third moment in the near continuum (nc) and the free molecular regime (fm).

$$\tilde{C}a_{0,ij} = \frac{\tilde{C}a^{nc}_{0,ij}\tilde{C}a^{fm}_{0,ij}}{\tilde{C}a^{nc}_{0,ij} + \tilde{C}a^{fm}_{0,ij}} \tag{4.39}$$

$$\tilde{C}a_{3,ij} = \frac{\tilde{C}a^{nc}_{3,ij}\tilde{C}a^{fm}_{3,ij}}{\tilde{C}a^{nc}_{3,ij} + \tilde{C}a^{fm}_{3,ij}} \tag{4.40}$$

The solution for intra-modal coagulation is derived analogously.
Furthermore, the coagulation rate $\tilde{C}a_{k,l}$ is converted to the coagulation rate of the mass mixing ratio for k = 3 and number mixing ratio for k = 0, as given in equations 4.41 and 4.42.

$$Ca_{0,l} = \frac{1}{\rho_a}\tilde{C}a_{0,l} \tag{4.41}$$

$$Ca_{3,l} = \frac{\rho}{\rho_a}\tilde{C}a_{3,l} \tag{4.42}$$

4.2.4. Gas-phase chemistry

There are three options in ICON-ART to simulate gas-phase chemistry. The first option is a lifetime approach, for which chemical tracers are depleted or react to other species with a given value for the atmospheric lifetime (Rieger et al., 2015). The second method is a complex chemistry mechanism according to Schröter et al. (2018). This thesis uses the third option, which is a simplified OH-mechanism by Weimer et al. (2017). For this mechanism the following reactions for chemistry and photolysis are used to calculate OH formation and depletion. According to Jacob (1986), the reaction system is given in the following:

$$\mathrm{O_3 + h\nu \xrightarrow{J_{O_3}} O(^1D) + O_2}$$

$$\mathrm{N_2 + O(^1D) \xrightarrow{k_{N_2}} O(^3P) + N_2}$$

$$\mathrm{O_2 + O(^1D) \xrightarrow{k_{O_2}} O(^3P) + O_2}$$

$$\mathrm{H_2O + O(^1D) \xrightarrow{k_{H_2O}} 2\ OH}$$

$$\mathrm{OH + CH_4 \xrightarrow{k_{CH_4}} H_2O + CH_3}$$

$$\longrightarrow ... \longrightarrow \mathrm{CO} + \mathrm{HO_2}$$

$$\mathrm{OH} + \mathrm{CO} \xrightarrow[\mathrm{M}]{\mathrm{k_{CO,1}}} \mathrm{H} + \mathrm{CO_2}$$

$$\mathrm{OH} + \mathrm{CO} \xrightarrow[\mathrm{M}]{\mathrm{k_{CO,2}}} \mathrm{HOCO}$$

In the reaction system k denotes the reaction rate and J the photolysis rate. The OH concentration is then given by:

$$[\mathrm{OH}] = \frac{2[\mathrm{O(^1D)}]\mathrm{k_{H_2O}}[\mathrm{H_2O}]}{\mathrm{k_{CH_4}}[\mathrm{CH_4}] + (\mathrm{k_{CO,1}} + \mathrm{k_{CO,2}}[\mathrm{CO}])}$$

The $\mathrm{O(^1D)}$ concentration is given by:

$$[\mathrm{O(^1D)}] = \frac{\mathrm{J_{O_3}}[\mathrm{O_3}]}{\mathrm{k_{O_2}}[\mathrm{O_2}] + \mathrm{k_{N_2}}[\mathrm{N_2}] + \mathrm{k_{H_2O}}[\mathrm{H_2O}]}$$

ICON-ART uses an online photolysis module that derives the O_3 photolysis rate J_{O_3} according to Weimer et al. (2017). For ozone a climatological value is used. Besides the gases within the OH reaction system additional gases can be included in the mechanism, which can further react with OH e.g. SO_2.

$$\mathrm{OH} + \mathrm{SO_2} \longrightarrow \mathrm{H_2SO_4}$$

4.3. Aerosol-radiation interaction

4.3.1. Theoretical background

This part follows Bellouin and Yu (2022). The solar spectrum ranges from the ultraviolet in to the infrared spectrum (the wavelengths (λ) between 0.25 μmat and 4 μm), covering the entire visible spectrum. Terrestrial radiation emitted by the Earth's surface peaks in the infrared between $\lambda = 8$ μm and $\lambda = 10$ μm. Aerosols can interact with radiation by absorption, scattering and emission of electro-magnetic radiation. Scattering defines a change in the direction of propagation of an electro-magnetic wave due to interaction with an aerosol. There are four scattering regimes depending on the ratio between particle diameter d_p and wavelength λ and is referred to as size parameter x (equation 4.43).

$$x = \frac{\pi d_p}{\lambda} \tag{4.43}$$

For size parameters $x \leq 0.002$ scattering can be neglected, for $0.002 \leq x \leq 0.2$ Rayleigh scattering and for $0.2 \leq x \leq 2000$ Mie scattering is assumed. For size parameters $x > 2000$ geometric optics are applied. Scattering on aerosols is mostly in the Mie scattering regime. The Mie theory is an exact solution of

Maxwell equations for homogeneous spheres, which calculates extinction and scattering efficiencies, the phase function P, the asymmetry parameter and the particle complex refractive index m. The latter depends on the chemical composition of the particle including the mixing state. The real part n_r is the ratio of the velocity of radiation in a vacuum to the velocity of the particle and the imaginary part n_i describes the attenuation during the propagation through the particle.

$$m = n_r - i \times n_i \tag{4.44}$$

Further, Rayleigh scattering can take place on aerosols with diameters smaller than the wavelength. The scattering is predominately elastic and results in an electric polarization of the particle, which then radiates. The amount of scattering is inversely proportional to the fourth power of the wavelength. In this work it is assumed that aerosol scattering follows Mie theory and therefore, this section focuses on Mie theory.

Assuming a single spherical aerosol with a radius r, the probability of scattering radiation at a certain wavelength is given by the scattering cross section σ_{sca} with the unit m^2. Therefore, the scattering efficiency can be written as:

$$Q_{sca} = \frac{\sigma_{sca}}{\pi r^2} \tag{4.45}$$

The maximum values for Q_{sca} occur for the relation r~λ. This concludes that accumulation mode particles scatter solar radiation and coarse mode particles scatter terrestrial radiation most efficiently. Regarding not a single aerosol but an aerosol population, it is useful to calculate the size parameter with the effective radius. The effective radius r_{eff} describes the area-weighted mean radius of an aerosol population with the number size distribution $n(r)$:

$$r_{eff} = \frac{\int_0^\infty r\pi r^2 n(r)dr}{\int_0^\infty \pi r^2 n(r)dr} \tag{4.46}$$

Using the effective radius the scattering efficiency is:

$$Q_{sca} = \frac{\int_0^\infty \sigma_{sca}(r)n(r)dr}{\int_0^\infty \pi r^2 n(r)dr} \tag{4.47}$$

In remote sensing the volume scattering coefficient β_{sca} is commonly used and given by:

$$\beta_{sca} = \int_0^\infty \sigma_{sca}(r)n(r)dr \tag{4.48}$$

Further, the mass scattering coefficient k_{sca} is defined as in equation 4.49 and usually used in modeling. Here, ρ is the particle density.

$$k_{sca} = \frac{1}{\rho} \int_0^\infty \sigma_{sca}(r) n(r) dr \tag{4.49}$$

The scattering of radiation leads to a change in the direction of the propagating waves. The angle between the incident and scattered radiation is called scattering angle and denoted as Θ (equation 4.50), θ_s is the solar zenith angle with respect to the local vertical and azimuth angle Φ_s. Further, θ_v and Φ_v are the zenith and azimuth angles of the scattered radiation.

$$\cos(\Theta) = -\cos(\theta_s)\cos(\theta_v) - \sin(\theta_s)\sin(\theta_v)\cos(\Phi_s \Phi_v) \tag{4.50}$$

In the case of forward scattering $\Theta = 0$ and for backwards scattering $\Theta = -\pi$. The phase function $P(\Theta)$ describes the probability that radiation is scattered with the angle Θ. For an aerosol population with the number size distribution $n(r)$ the phase function reads:

$$P(\Theta) = \frac{\int_0^\infty \sigma_{sca} P(\Theta, r) n(r) dr}{\int_0^\infty \sigma_{sca} n(r) dr} \tag{4.51}$$

Further, $P(\Theta)$ is normalized as shown in equation 4.52, as the probability of being scattered in any direction corresponds to the solid angle of a sphere.

$$\int_0^{2\pi} \int_{-1}^{1} P(\Theta) d\cos(\Theta) d\Phi = 4\pi \tag{4.52}$$

Many radiative transfer codes use the asymmetry parameter g. It is the mean cosine of the scattering angle weighted by the $P(\Theta)$.

$$g = \int_{-1}^{+1} P(\Theta) \cos\Theta d\Theta \tag{4.53}$$

g ranges from -1 to 1 and is +1 for pure forward scattering, -1 for pure backward scattering and zero for symmetric scattering (Rayleigh scattering).

Besides the scattering of radiation, aerosols can also absorb electro-magnetic radiation. Absorption refers to the conversion of radiation into internal energy by the absorber and can be explained with the help of quantum physics as the transition of electrons of the molecule to higher quantized energy levels. It usually results in heating, which further alternates the atmospheric stability, cloud formation and therefore the initial radiative fluxes.

Analog to scattering, the absorption cross section σ_{abs} has the unit m^2. The absorption efficiency can be written as:

$$Q_{abs} = \frac{\sigma_{abs}}{\pi r^2} \tag{4.54}$$

The absorption coefficient β_{abs} is then defined as:

$$\beta_{abs} = \int_0^\infty \sigma_{abs}(r) n(r) dr \tag{4.55}$$

and the mass absorption coefficient is defined as:

$$k_{abs} = \frac{1}{\rho} \int_0^\infty \sigma_{abs}(r) n(r) dr \tag{4.56}$$

Extinction defines the amount of radiation that is either scattered or absorbed. Extinction cross section, efficiency factor, volume and mass specific extinction coefficients can be expressed as the sum of the scattering and absorption.

$$\sigma_{ext} = \sigma_{sca} + \sigma_{abs} \tag{4.57}$$

$$Q_{ext} = Q_{sca} + Q_{abs} \tag{4.58}$$

$$\beta_{ext} = \beta_{sca} + \beta_{abs} \tag{4.59}$$

$$k_{ext} = k_{sca} + k_{abs} \tag{4.60}$$

The column integrated extinction of an aerosol layer is the aerosol optical depth τ and strongly depends on the amount of aerosols, which is given by:

$$\tau = \int_{\text{sfc}}^{\text{toa}} \beta_{ext}(z) dz = \int_{\text{sfc}}^{\text{toa}} k_{ext}(z) \rho(z) dz \tag{4.61}$$

Here, z is the vertical height from the surface to the top of the atmosphere. τ is wavelength dependent. The Ångström exponent α describes the wavelength dependency of τ and is given in equation 4.64, where λ_1 and λ_2 are two different wavelengths.

$$\tau(\lambda_1) = \tau(\lambda_2) \times (\frac{\lambda_1}{\lambda_2})^{-\alpha} \tag{4.62}$$

This leads to:

$$\alpha = -\frac{\frac{log\tau(\lambda_1)}{log\tau(\lambda_2)}}{\frac{log\lambda_1}{log\lambda_2}} \tag{4.63}$$

The Ångström exponent is further used as a first order indication of the effective particle size. Thereby, Rayleigh scattering is associated with large Ångström exponents of 4. In the Mie regime the Ångström exponent varies between $\alpha = 0$-2.5. Coarse particles may even reach negative values. The Ångström exponent can further be applied to τ_{sca} and τ_{abs}, which can be useful to distinguish between aerosol types.
Furthermore, the single scattering albedo ω provides the fraction of extinction due to scattering and is defined by:

$$\omega = \frac{\sigma_{sca}}{\sigma_{ext}} = \frac{\sigma_{sca}}{\sigma_{sca} + \sigma_{abs}} = 1 - \frac{\sigma_{abs}}{\sigma_{ext}} \tag{4.64}$$

ω is independent of the aerosol mass and is 1 for aerosols, which purely scatter radiation and 0 indicates pure adsorption.

4.3.2. Aerosol-radiation interaction in ICON-ART

Radiation is an important driver of weather and climate. NWP models use radiative transfer models to solve the radiative fluxes in the atmosphere based on assumptions of the optical property parameterizations for different atmospheric components (gases, aerosols, clouds) and the surface, as well as how radiation travels through the medium. ICON-ART uses the ecRad model (Hogan and Bozzo, 2018), which is implemented in ICON according to Rieger et al. (2019). The optical properties of cloud particles, aerosols and gases are wavelength dependent. ICON uses the RRTM (Rapid Radiative Transfer Model) optics scheme by Mlawer et al. (1997). The scheme has a spectral range from 0.2–1000 μm divided into 30 spectral bands, with 14 spectral bands in the short wave range and 16 in the long wave. These bands are used for aerosol and cloud particle optical properties, the gas optical properties are further divided into sub-intervals. Only up- and down welling radiation is considered and the optical properties are integrated for all angles. This reduces the necessary optical parameters to the mass extinction coefficient k_{ext}, the single scattering albedo ω and the asymmetry parameter g.
The optical properties of cloud particles depend on the size, shape and amount of water or ice and can be calculated with a complex function for Mie scattering with a given assumption for the particle size and shape. There are several optics parameterizations available in ecRad. The surface optical properties are based on satellite observations and provided in an external parameter file.
For aerosols, the optical properties are directly provided as an input file to the radiation scheme and is discussed in more detail in section 4.5.4. With all these information ecRad calculates reflection, transmission and internal radiation sources for each grid-box and each model level, resulting in the upward and downward welling radiation flux. Further, the radiative heating and cooling is calculated, which feeds back into the dynamics and physics.

4.4. Biomass burning emissions in ICON-ART

The injection height and the emission flux are the two key parameters to correctly simulate biomass burning emissions. In ICON-ART the emission flux of black carbon is based on satellite data from the Global Fire Assimilation System (GFAS) (Kaiser et al., 2012) and the emission height is parameterized via the plume-rise model by Freitas et al. (2006, 2007), and Walter et al. (2016). GFAS is based on the Fire Radiative Power (FRP), which is part of the NASA fire product MOD14. MOD14 includes thermal radiation observations (λ ~3.9 μm-11 μm) of the MODIS instrument (Giglio, 2007; Justice et al., 2011). MODIS (Moderate Resolution Imaging Spectroradiometer) is placed on the two polar orbiting satellites Terra and Aqua. The orbits are timed so that Terra passes from north to south across the equator in the morning and Aqua in the afternoon.

Thermal radiation cannot penetrate clouds, which makes satellite observations of active fires only reliable in cloud-free regions. To overcome these data gaps the fire data is assimilated using a Kalman filter (Rodgers, 2000). It is assumed that the true FRP density is given by the FRP density at time step t, which persists from the previous time step $t-1$ and the observation of the FRP density at time step t. Further, the sampling is limited to a maximum of four times a day. It is assumed that these three to four daily overpasses represent the diurnal cycle of the fire well (Kaiser et al., 2012). The FRP measures the radiative energy released by the fire, which is assumed to be related to the amount of vegetation burned and is proportional to biomass burning emissions (Kaiser et al., 2012). Wooster et al. (2005) propose an universal combustion rate of f(DM) = 0.368 kg MJ^{-1} to link FRP with the dry matter (DM) combustion rate. Heil et al. (2010) find that the combustion rate depends on the land cover and therefore, the vegetation type. GFAS1.0 differentiates between eight land cover classes and can be found in Kaiser et al. (2012). The emission factors for the species relevant for this work are given in table 4.3. The emission factor of a species is then given by:

$$f(s) = \kappa(s) f(DM) \tag{4.65}$$

Table 4.3.: Emission factors $\kappa(s)$ [g(species) kg^{-1}(DM)] for savanna (SA), tropical forest (TF) extra tropical forest (EF), agriculture (AG), peat (PEAT) taken from Kaiser et al. (2012).

Species	κ(SA)	κ(TF)	κ(EF)	κ(AG)	κ(PEAT)
BC	0.46	0.57	0.56	0.42	0.04
OC	3.2	4.3	9.1	4.2	6.0
CO_2	1646	1626	1572	1308	1703
CO	61	101	106	92	210

Plume-rise model

Table 4.4.: Upper and lower heat flux limits depending on biome type taken from Freitas et al. (2006)

Biome type	Upper limit [kW m^{-2}]	Lower limit [kW m^{-2}]
Tropical fores	80.	30.
Woody savanna - cerrado	23.	4.4
Grassland - pasture - cropland	3.3	

At the current state the emission height of biomass burning products is parameterized with the plume-rise model by Freitas et al. (2006, 2007, 2010). The Freitas model is the most commonly used plume-rise model (Kumar et al., 2022) and implemented in a variety of forecasting models for example: the Weather Research and Forecasting with Chemistry (WRF-Chem) and the High-Resolution Rapid Refresh coupled with Smoke (HRRR-Smoke). The Freitas model is an one-dimensional plume-rise parameterization that is usually embedded in a three-dimensional host model. The host model in this work is the ICON-ART model and the implementation is done similar to Walter et al. (2016) in the COSMO-ART model. The Freitas model uses the entertainment model by Latham (1994), in which the equations are based on the first law of thermodynamics and the vertical equation of motion. It further includes cloud microphysical calculations based on Kessler (1969). The entertainment is assumed to be proportional to the vertical velocity in the air and anti-proportional to the radius of the plume. Buoyancy is treated as a virtual source term below the surface. The buoyancy is derived from the energy flux, depending on the vegetation type and the fire size, which is assumed to be 50 ha for the ICON-ART implementation. The fire vegetation type is divided into three categories: forest, woody savanna, and grassland. There is an upper and lower bond for each category defined by table 4.4. A factor of 0.55 suggested by McCarter and Broido (1965) is used to convert the heat flux to convective energy. It is assumed that 0.5 kg of H_2O is released per kg of dry fuel weight. The model has a 100 m grid spacing and a maximum height of 20 km with 200 vertical levels. As mentioned, this one-dimensional model is embedded in the three-dimensional ICON-ART model, which feeds the plume-rise model with the ambient conditions such as temperature, pressure, horizontal winds and humidity. For the lower boundary a theoretical source of boundary is placed below the surface to generate high vertical velocities at the surface. The upper buoyancy is limited by the turbulent and dynamic entertainment, which results in dilution and widening of the plume. In case of condensation, latent heat release further increases the buoyancy. The top of the plume is reached once the vertical velocity is below 1 ms^{-1}. The plume-rise model returns a plume bottom and top height. Between these heights a parabolic emission profile $f(z^*)$ is assumed and illustrated in figure 4.2.

$$f(z^*) = 6z^*(1-z^*) \tag{4.66}$$

The dimensionless height z^* is defined as:

$$z^* = \frac{z - z_{bot}}{z_{top} - z_{bot}} \tag{4.67}$$

z is the model height, z_{top} and z_{bot} are the plume top and bottom heights, respectively. The total emission Q_{tot} is emitted where $0 \leq z^* \leq 1$ .The fraction emitted in a grid cell with the upper bond z^*_{uplev} and lower bond z^*_{lowlev} is given by:

$$\int_{z^*_{lowlev}}^{z^*_{uplev}} Q_{tot} f(z^*) = Q_{tot}[3z^{*^2} - 2z^{*^3}]_{z^*_{lowlev}}^{z^*_{uplev}} \tag{4.68}$$

Additionally, a diurnal cycle is applied for the emission. According to Giglio (2007) and Zhang and Kondragunta (2008), the diurnal cycle depends on the vegetation type and the meteorological conditions. The daily maximum is typically reached between 10:00 and 15:00 local time. Modified from Kaiser et al. (2009) the diurnal cycle can be displayed by a weighted normal distribution, given in equation 4.69, and is normalized afterwards (illustrated in 4.2).

$$d(t_1) = \omega + \frac{1}{\sigma\sqrt{2\pi}} \exp\Big(-\frac{1}{2}\big(\frac{t_1 - t_0}{\sigma}\big)^2\Big) \tag{4.69}$$

In this case ω is a weighting, which is set according to the vegetation type. ω is 0.039 for tropical forests, 0.018 for savannas and 0.003 for grassland. t_1 is the local solar time, t_0 is the expected value of maximum emission set to 12.5 and σ is the standard deviation, set to 2.5. The emissions are maintained constant

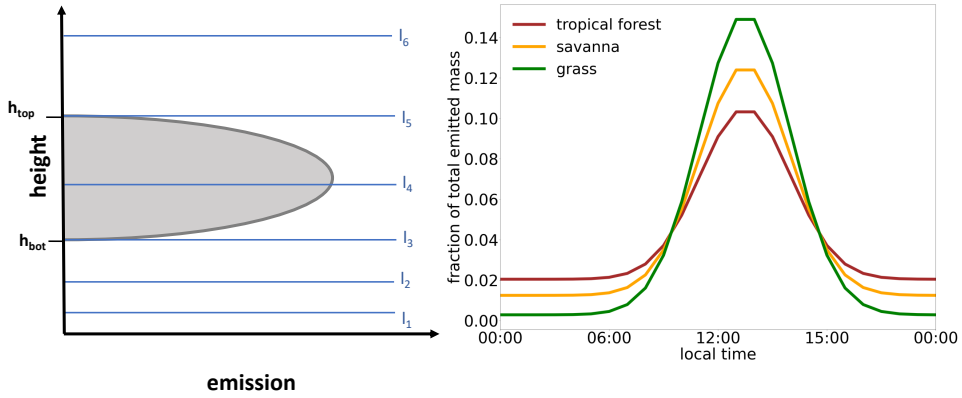

Figure 4.2.: Left: Schematic illustration of the parabolic emission profile, between injection bottom height (h_{bot}) and top height (h_{top}) returned from the plume-rise model. Right: The diurnal cycle of the emission for the different vegetation classes.

over an hour. The emission rate E in kg m^{-2} s^{-1} is calculates for a respective grid cell and is depending on the height z and the time t.

$$E(z,t) = M(t) \times d(t) \times f(z^*,t) \tag{4.70}$$

M is the daily mean emission flux in kg m^{-2} s^{-1} based on the GFAS data. d is the diurnal cycle given by equation 4.69 and f is the parabolic emission profile between the top and bottom injection height.

4.5. Extension of biomass burning emissions

4.5.1. Modification to the biomass burning emissions

So far, the biomass burning emissions only included black carbon as an aerosol source. For this study the emitted biomass burning aerosol consists of the sum of black and organic carbon. Both emission fluxes are taken from GFAS. Further, the emission flux is multiplied by an empirical factor of 3.4. This factor is suggested by Kaiser et al. (2012). Lastly, the assumption that the fire size is constant and 50 ha in every grid cell is replaced by the approach of Val Martin et al. (2012), which is further used by Ke et al. (2021). Here, the fire size per grid cell A_{gc} is given by:

$$A_{gc} = \Delta r \frac{FRP_{gc}}{FRP_{max}} \tag{4.71}$$

Δr is the resolution of the detected fire, in this case the GFAS resolution of 0.1°. FRP_{max} is the maximum FRP and defined as the 99th percentile value of the detected FRP in the fire region. FRP_{gc} is the fire radiative power in the respective grid cell.

4.5.2. Implementation of moisture release

Section 2.2.1 explains how moisture is released by fire and its importance for the plume dynamic. The plume-rise model parameterizes moisture release for the calculation of the injection height. The effect is only considered for the injection height parameterization and the effect on the atmosphere in the host model is neglected. This work extends this and considers the effect of moisture release by the fire on the atmosphere of the host model ICON.

Firstly, the release of combustion moisture is implemented. According to Parmar et al. (2008) an emission ratio of 0.75 $H_2O/(CO+CO_2)$ is a valid assumption for an average biomass. Both CO and CO_2 are emission products provided by GFAS. These emissions are taken and scaled with the emission fraction of 0.75 and emitted in the ICON q_v tracer, the specific humidity tracer. Besides combustion moisture, fuel moisture is considered. The latter is divided into dead and live fuel moisture. Following Nolan et al. (2016), the threshold for high probability of ignition is 101.5 % for live fuels and 14.6 % for dead fuels. This is also in agreement with the findings by Deb et al. (2020) for south-east Australia during the Black

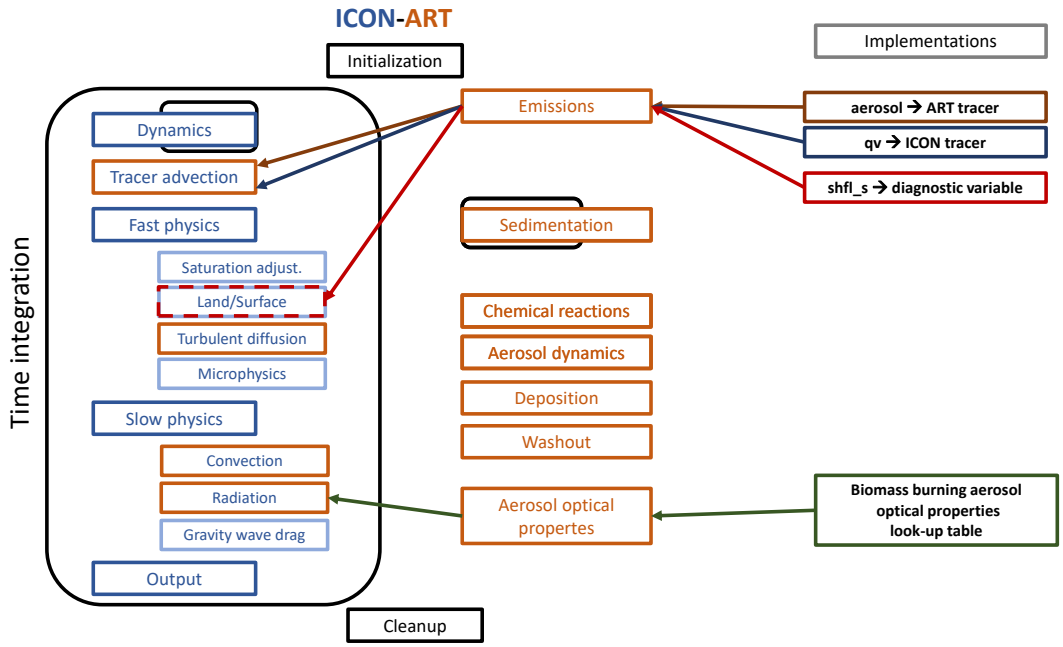

Figure 4.3.: Coupling of the dynamical core, the NWP physics, and ART routines package in ICON-ART, adapted from Rieger et al. (2015) and extended by modifications in this work.

Summer Fires. Deb et al. (2020) find dead fuel moisture contents between 5.3 % and 23.0 % and live fuel moisture between 55.5 % and 119.6 %, depending on the region. Further, it is assumed that 30 % of the fuel is dead and 70 % is live fuel. This leads to a proximate fuel moisture of 75.42 %. This fuel moisture of 75.42 % is multiplied with the GFAS combustion rate. The live to dead fuel ratio is taken from Hines et al. (2010), who provide fuel hazard ratings. 30 % dead fuel moisture corresponds to a very high hazard rating for elevated and near surface fuels. This leads to a moisture emission flux qv_{fire} by the fire in kg m^{-2} s^{-1} of

$$qv_{fire} = (0.75 \times (m_{CO} + m_{CO_2}) + 0.7542 \times m_{load}) \times d(t) \tag{4.72}$$

where m_{CO} and m_{CO_2} are the mass fluxes of CO and CO_2 in kg m^{-2} s^{-1}, respectively and m_{load} is the combustion rate (burned fuel load per square meter per second) with the unit kg m^{-2} s^{-1}. qv_{fire} is further multiplied with the diurnal cycle function $d(t)$. Figure 4.3 gives a schematic illustration where the modifications in the code are made. The GFAS data is read in in the ART part and pre-processed before being emitted into the q_v tracer, an ICON tracer.

The many assumptions made are highlighted in the following. The combustion moisture ratio is a suggested mean, but strongly dependent on the vegetation type and combustion phase. The thresholds for dead and live fuel moisture are plausible upper limits, especially for the dead moisture, which strongly depends on the meteorology. And given that the studied period is affected by severe droughts, the fuel moisture might be overestimated. Further, the GFAS combustion rate is assumed to represent the fuel dry weight.

The implementation is applied for two setups. In a setup with the plume-rise model the moisture is released with the same parabolic distribution as for the biomass burning aerosols. In a plume-resolving setup the moisture is emitted in the lowermost model level. The moisture emission is further weighted with the diurnal cycle function in both setups.

4.5.3. Implementation of heat release

Heat release from the fire is important for convection and plume rise, a detailed explanation is given in section 2.2.2. The GFAS data set provides the FRP, therefore, the radiative fraction of total heat release. The FRP is multiplied by 10 to retrieve the total energy released by the fire, as it is proposed by Val Martin et al. (2012) and further applied in Ke et al. (2021). A factor of 0.55 is applied to convert the total energy to convective energy. The factor is taken from Freitas et al. (2006), following McCarter and Broido (1965) and is similar to the convective fraction 0.518 and 0.52 in Freeborn et al. (2008) and Morandini et al. (2013), respectively. The FRP is weighted with the diurnal cycle function, which is also applied to the emission. The convective fraction is implemented as heat source in the sensible heat flux at the surface. This leads to a sensible heat release by the fire sh_{fire} in W m^{-2} of:

$$sh_{fire} = FRP \times 10 \times 0.55 \times d(t) \tag{4.73}$$

The FRP with the unit W m^{-2} is read, converted to the sensible heat flux, and weighted with the diurnal cycle function $d(t)$ in the ART part. Further This variable is then passed to the land/surface subroutines that calculate the sh_{fire}. The sensible heat flux is then added to the surface sensible heat flux. The workflow is illustrated in figure 4.3.

4.5.4. Implementation of optical properties

The interaction of biomass burning aerosols and radiation is discussed in section 2.2.4 and as described in section 4.3 the necessary input variables for the ICON-ART radiation calculations are the mass extinction coefficient (k_{ext}), the single scattering albedo (ω) and the asymmetry factor (g). These parameters are retrieved using a Mie code developed by Bond et al. (2006) and Mätzler (2002) based on Bohren and Huffman (2008). Studies like Brito et al. (2014) suggest that biomass burning aerosols grow a shell, and therefore are internally mixed. To account for this coating of the particles a core shell ratio can be included in the calculations.

To receive the input parameters a case study is performed. The setup is the same as the setup of the REF experiment, which is explained in section 6.1, but only lasts for 24 hours. Important for this section is that 6 % of the aerosol mass is emitted in the insoluble Aitken mode and 94 % in the insoluble accumulation mode. The particles emitted in the Aitken mode have a median number diameter $d_n = 20$ nm and standard deviation $\sigma = 1.7$ and the particles in the accumulation mode have a $d_n = 70$ nm with $\sigma = 2.0$. Further, a

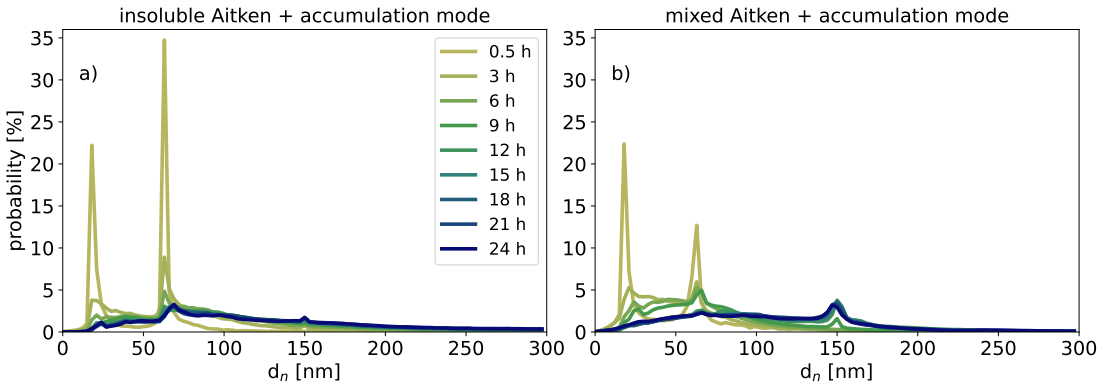

Figure 4.4.: Temporal evolution of the probability density function of the median number diameter d_n in a grid cell exceeding a mass mixing ratio of 10^{-3} μg kg^{-1} in the a) insoluble Aitken and insoluble accumulation mode and the b) mixed Aitken and mixed accumulation mode.

simplified OH-chemistry is used and nucleation, condensation and coagulation is enabled.

The input parameters needed for the Mie calculations are the median diameter, the shell-to-core fraction and the inorganics-to-H_2O fraction. Figure 4.4 shows the probability density function (PDF) of d_n in a grid cell exceeding a mass mixing ratio of 10^{-3} μg kg^{-1} for the insoluble and the mixed mode in figure 4.4 a and b, respectively. The different colors represent different simulation times. Both cases show three peaks, at 20 nm, 70 nm, and 150 nm. The peaks at 20 nm and 70 nm are at the emission diameters and decrease over time, while the peak at 150 nm increases over time, especially for the mixed mode. This can be explained by particle growth due to condensation and coagulation. Based on these PDFs a median number diameter of $d_n = 20$ nm is chosen for the smaller Aitken mode, and $d_n = 150$ nm for the larger accumulation mode. These values are consistent with findings by Brito et al. (2014), Levin et al. (2010), and Sakamoto et al. (2015). Further, the shell-to-core and inorganics-to-H_2O fractions are calculated for every grid cell exceeding an aerosol threshold of 10^{-3} μg kg^{-1} in the respective mode and displayed in the PDFs in figure 4.5. For the smaller Aitken mode, the shell-to-core fraction peak shifts towards a faction of 0.1 over time. This is similar for the accumulation mode, but over time the probability of fractions larger 0.5 increases as well. Measurements by Brito et al. (2014) suggest soluble-to-insoluble fractions of 0.07 and 0.12 for two different measurement episodes. Based on these results, it is decided on a shell-to-core fraction of 0.1. This is further within in the ranges reported by Reid et al. (1998b). Furthermore, the inorganics-to-H_2O fraction for the Aitken mode and the accumulation mode show several peaks for the different time steps. Over time the fraction declines especially in the accumulation mode. Still, it is decided on an inorganics-to-H_2O fraction of 0.75. The results of the Mie calculations are presented and discussed in section 6.3.4.

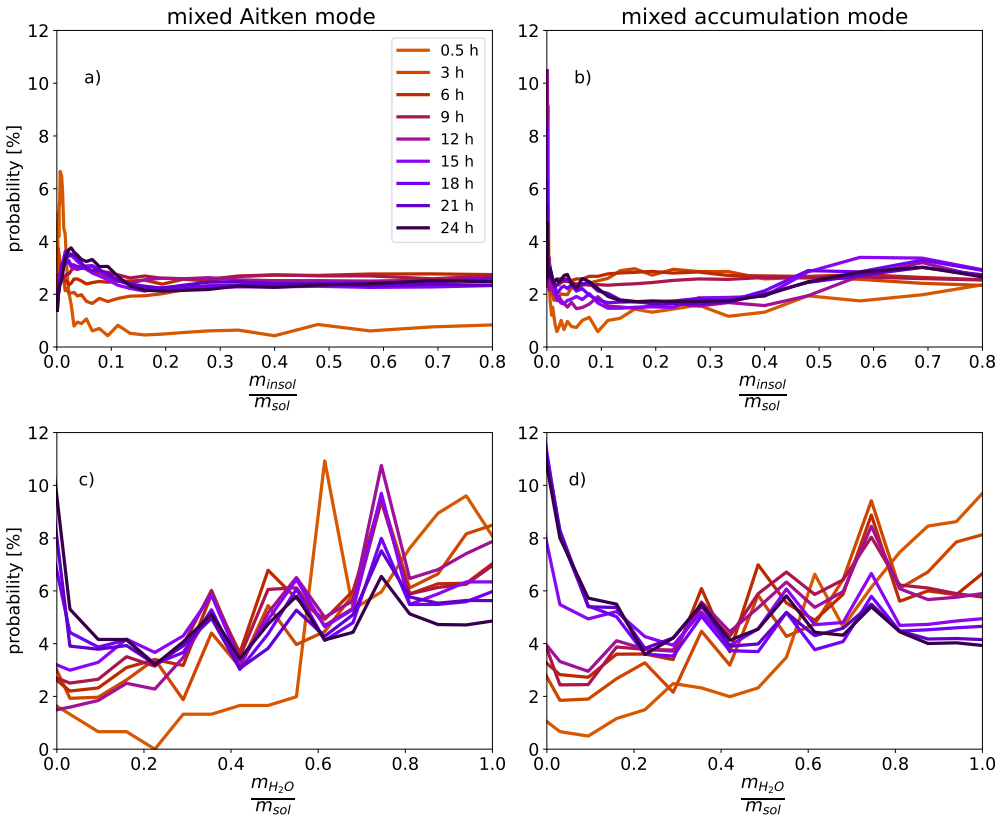

Figure 4.5.: Temporal evolution of the probability density function of the insoluble-to-soluble mass fraction ($\frac{m_{insol}}{m_{sol}}$) in a grid cell exceeding a mass mixing ratio of 10^{-3} μg kg^{-1} in the a) mixed Aitken mode and b) mixed accumulation mode. The H_2O-to-soluble mass fraction ($\frac{m_{H_2O}}{m_{sol}}$) is shown for c) the mixed Aitken and d) mixed accumulation mode.

5. Plume-resolving simulations

5.1. Simulation setup

Firstly, the plume-resolving experiment, further referred to as PR and plume-parameterizing experiment, further referred to as PP are compared. The area of the domains is shown in chapter 6 figure 6.1 in the black box. The grid spacing in PR is 0.6 km and in PP 6.6 km. Both simulations have 125 vertical levels from the surface to a maximum height of 30 km. The level thickness increases with height. The simulations start on the 29th of December 18:00 UTC, which corresponds to 05:00 Australian Eastern Daylight Time (AEDT) (on the 30th of December) and last for 24 hours. The following results will be displayed in AEDT. Boundary conditions are read in every 30 min for PR. The simulations do not consider atmospheric chemistry, nucleation or condensation, but coagulation. In both cases the aerosol mass is emitted in the insoluble accumulation mode with a median number diameter $d_n = 70$ nm and a standard deviation of $\sigma = 2.0$. The emission fluxes for aerosols and the parameterizations of moisture and heat release are based on GFAS (CAMS, 2021). The first difference is in physics schemes. In experiment PP with the coarser grid spacing, convection is parameterized. The convection parameterization scheme for sub-grid moist convection is based on Bechtold et al. (2014) and Tiedtke (1989). The scheme mixes heat, moisture and momentum and thereby converts potential energy into kinetic energy and produces precipitation as a result of atmospheric instability. Further, PP uses the plume-rise model. The sensible and latent heat release by the fire is parameterized to get the aerosol injection height. The plume-rise model determines the sensible heat flux according to the vegetation type and the scaling in equation 4.71. Both remain constant in a given grid cell throughout the simulation. The fuel consumption, and therefore the parameterized moisture release is also assumed to be constant. In contrast convection is resolved in PR. Aerosols and the moisture released by the fire are emitted in the lowermost grid cell. The heat release by the fire is enabled as a sensible heat flux from the surface. In PR the heat and moisture release

Table 5.1.: Overview of the performed experiments.

Experiment	Grid spacing	plume-rise model	moisture release	sensible heat release
PP	6.6 km	✓	×	×
NoP	0.6 km	×	×	×
PR	0.6 km	×	100 %	100 %
PR_HEAT$^-$	0.6 km	×	100 %	64 %
PR_HEAT$^+$	0.6 km	×	100 %	136 %
PR_H2O$^+$	0.6 km	×	2000 %	100 %

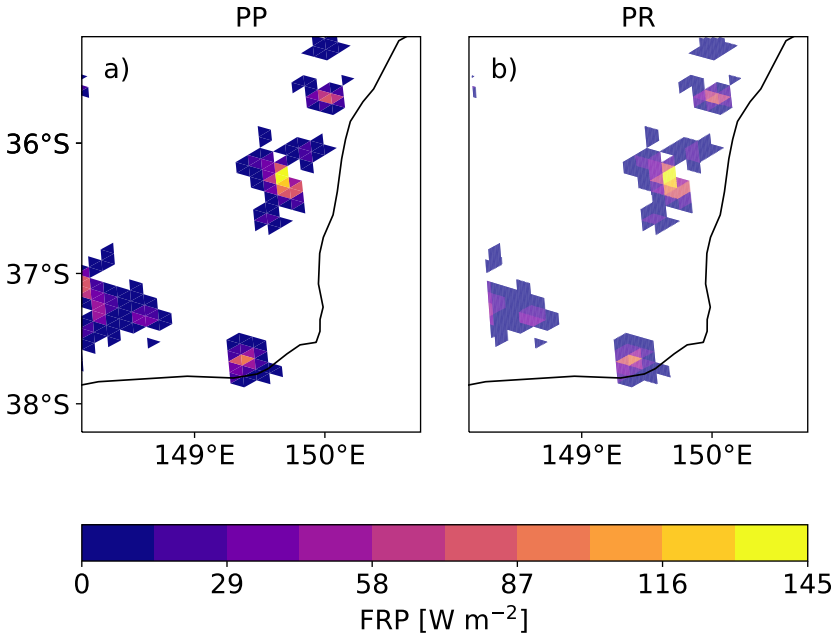

Figure 5.1.: Display of the GFAS fire radiative power (FRP) (CAMS, 2021) remapped to the corresponding ICON domains for a) the 600 m grid spacing and b) the 6.6 km grid spacing on the 30th of December 2020. Generated using Copernicus Atmosphere Monitoring Service information [2022].

is scaled with the diurnal cycle of the fire.

The PP and PR experiments use very different approaches to illustrate the buoyancy caused by the fire; a rough comparison is made here. In case of PR the maximum sensible heat flux by the fire is given in equation 4.73. With a maximum fire radiative power (FRP) of approximately 145 W m^{-2} the maximum sensible heat flux from the fire is ~797.5 W m^{-2}. The plume-rise model assumes a maximum total heat flux of 80 kW m^{-2}, which is multiplied with a factor 0.55 for the convective fraction and scaled with the area burned (~5×10^5 m^2) and the area of the grid cell (~4.3×10^7 m^2). This results in a sensible heat flux of 511 W m^{-2} and is therefore in the same order of magnitude as in the PR experiment. To test the sensitivity of the sensible heat release two experiments are performed. In the first experiment the sensible heat flux by the fire is decreased by 36 % to match the plume-rise model (PR_HEAT$^-$) and in the second experiment the sensible heat flux is increased by 36 % (PR_HEAT$^+$).

The implementation of the moisture release by the fire is explained in section 4.5.2 and calculated according to equation 4.72. Based on the GFAS input data a maximum moisture emission flux of $qv_{fire} = 1.4\ 10^{-4}$ kg m^2 s^{-1} is calculated. The plume-rise model assumes a fuel moisture of 10 %, a combustion moisture of 0.5 kg per kilogram of burned fuel and a fuel consumption of 10 kg m^2 s^{-1}. Again a mean area of 5×10^5 m^2 is burned in a grid cell with ~4.3×10^7 m^2. This results in a qv_{fire} of 0.07 kg m^2 s^{-1} and is therefore by a factor of 20 larger than the qv_{fire} in PR. An additional experiment is proposed, repeating PR with 20 times the moisture emission (PR_H2O$^+$). Additionally, an experiment

without heat and moisture release is performed, and named NoP, as no plume rise is expected. Figure 5.1 displays the FRP remapped from the GFAS data to the ICON grid for the different domains in PR with 0.6 km grid spacing and PP with a grid spacing of 6.6 km. The colored areas display active fires. The FRP has the same maximum value of 144.8 W m^{-2} and the same distribution for both setups. For PR there is a gap at the western border of the domain between 37°S and 37.6°S, because the domain is slightly smaller. The lighter colors in PR result from the finer grid spacing and white edge colors between the triangles, and is therefore an artifact of the plot. The emission of aerosols and moisture is proportional to the FRP. Therefore, the maximum emission is expected to be in the center of the domain, placed with the highest FRP. The FRP is further important for the plume-resolving simulations, as it determines the sensible heat release.

5.2. Results

Figure 5.2 displays the isosurfaces of the biomass burning aerosol concentration for five time steps between the 30th of December 08:00 AEDT and the 30th of December 20:00 AEDT. At 08:00 AEDT the plumes remain shallow, three hours later the plumes start to rise. The other three images show the spreading of the plume towards the south-east. The plume reaches the edge of the domain before the 30th of December 17:00 AEDT. By 20:00 AEDT, most of the plume is transported out of the domain, and aerosol emissions continue to decrease as night falls.

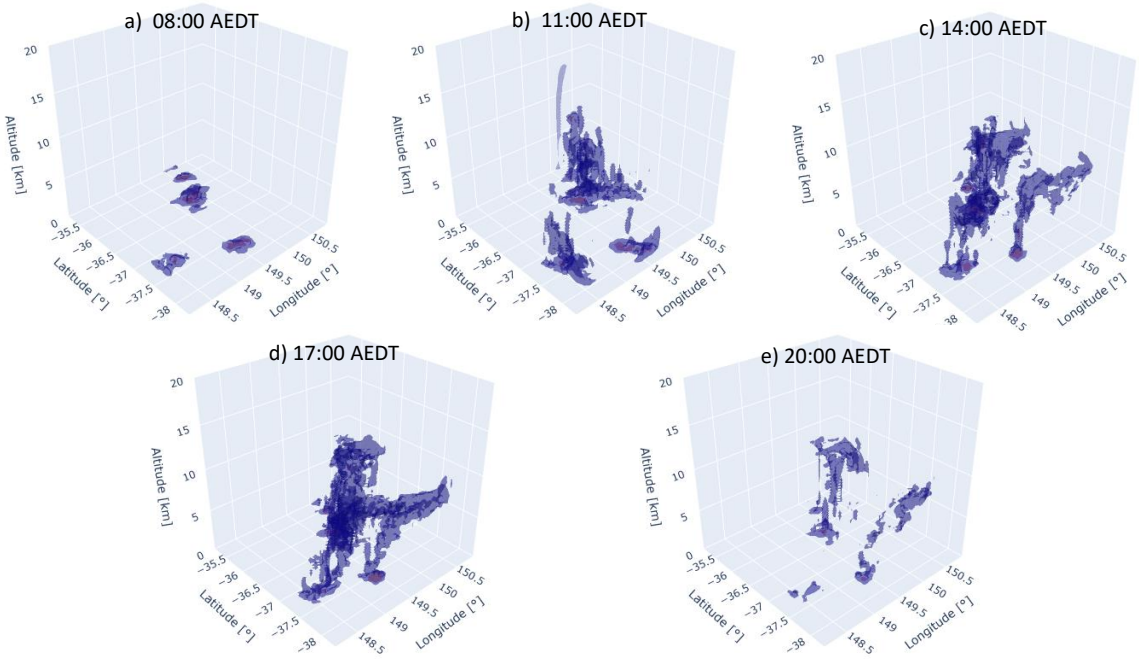

Figure 5.2.: Three-dimensional distribution of the plume in experiment PR, with the isosurfaces of 10 μg kg^{-1} in purple and 100 μg kg^{-1} in orange, for the 30th of December a) 08:00 AEDT, b) 11:00 AEDT, c) 14:00 AEDT, d) 17:00 AEDT, and e) 20:00 AEDT.

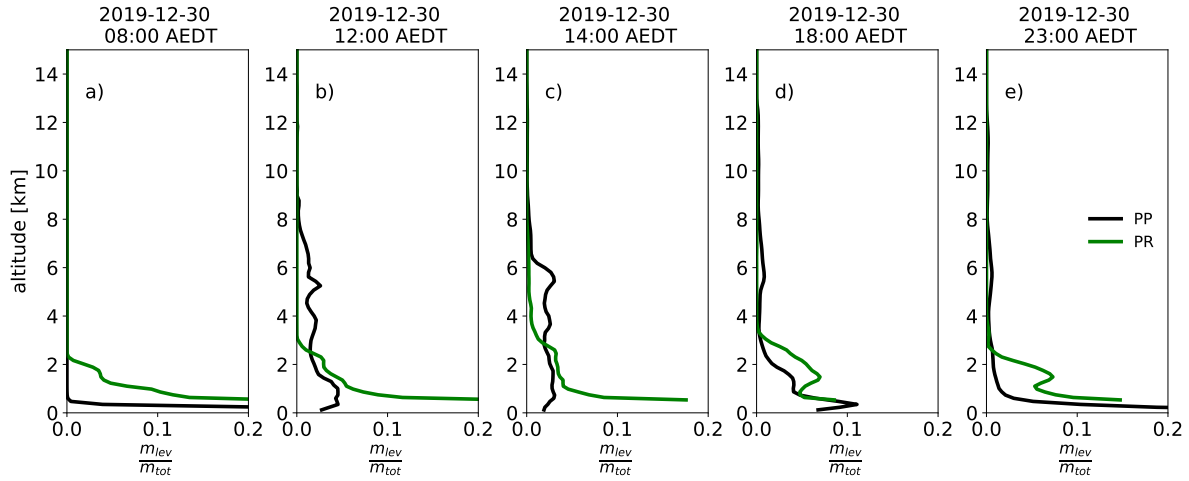

Figure 5.3.: Normalized vertical profiles of mean aerosol mass in every level above the fire area on the 30th of December. Experiment PP in black and PR in green. Different time steps are displayed: a) 08:00 AEDT, b) 12:00 AEDT, c) 14:00 AEDT, d) 18:00 AEDT, and e) 23:00 AEDT.

In the next step the plume height of the plume-parameterizing experiment PP is compared to the plume-resolving simulation. Therefore, the mean vertical profile of the biomass burning aerosol above the fire area is displayed in figure 5.3. In order to the compare the vertical profiles of experiments PR and PP the profiles are normalized to the total aerosol mass m_{tot}. In figure 5.3 a, PP starts with most of the aerosol mass in the lowermost model layer, during the day aerosols reach altitudes above 8 km and the mass peaks at 5.4 km and 5.8 km in figure 5.3 b and c. The normalized aerosol mass in the lowermost model level decreases for the PP experiment during the day. In the evening, figure 5.3 d and e, most of the aerosol mass is again below 2 km, thus there is a local peak around 6 km. In the plume-resolving experiment PR, aerosols reach up to 2.1 km from the simulation start. The height of the aerosol masses increases as well during the day. Aerosols reach altitudes above 6 km (figure 5.3 c), but most aerosols remain below 3 km.

In figure 5.4 the plume top height is displayed for PP, PR and the sensitivity experiments PR_H2O$^+$ and PR_HEAT$^+$. The plume is defined as every grid point that exceeds an aerosol mass mixing ratio of 1 μg kg^{-1}. The first row displays the plume top height at 18:00 AEDT. The distribution of the plume top height is similar in PR, PR_H2O$^+$ and PR_HEAT$^+$. The largest top heights are at the center of the domain moving south-east-east. In PR_H2O$^+$ the area of plume top heights above 12 km is larger than in PR, and again larger in PR_HEAT$^+$. There are two additional smaller features of elevated plumes further south. In PP the plume top height is widely increased, especially the plume developing from the fires at the western border of the domain. The plume is also moving south-east from the fires. The second row displays the plume top height at 20:00 AEDT and outlines the transport of the elevated plume out of the domain. This illustrates that for the experiments PR_H2O$^+$ and PR_HEAT$^+$ the elevated aerosols remain in the domain longer compared to experiment PR. In the bottom row at 22:00 AEDT, aerosols

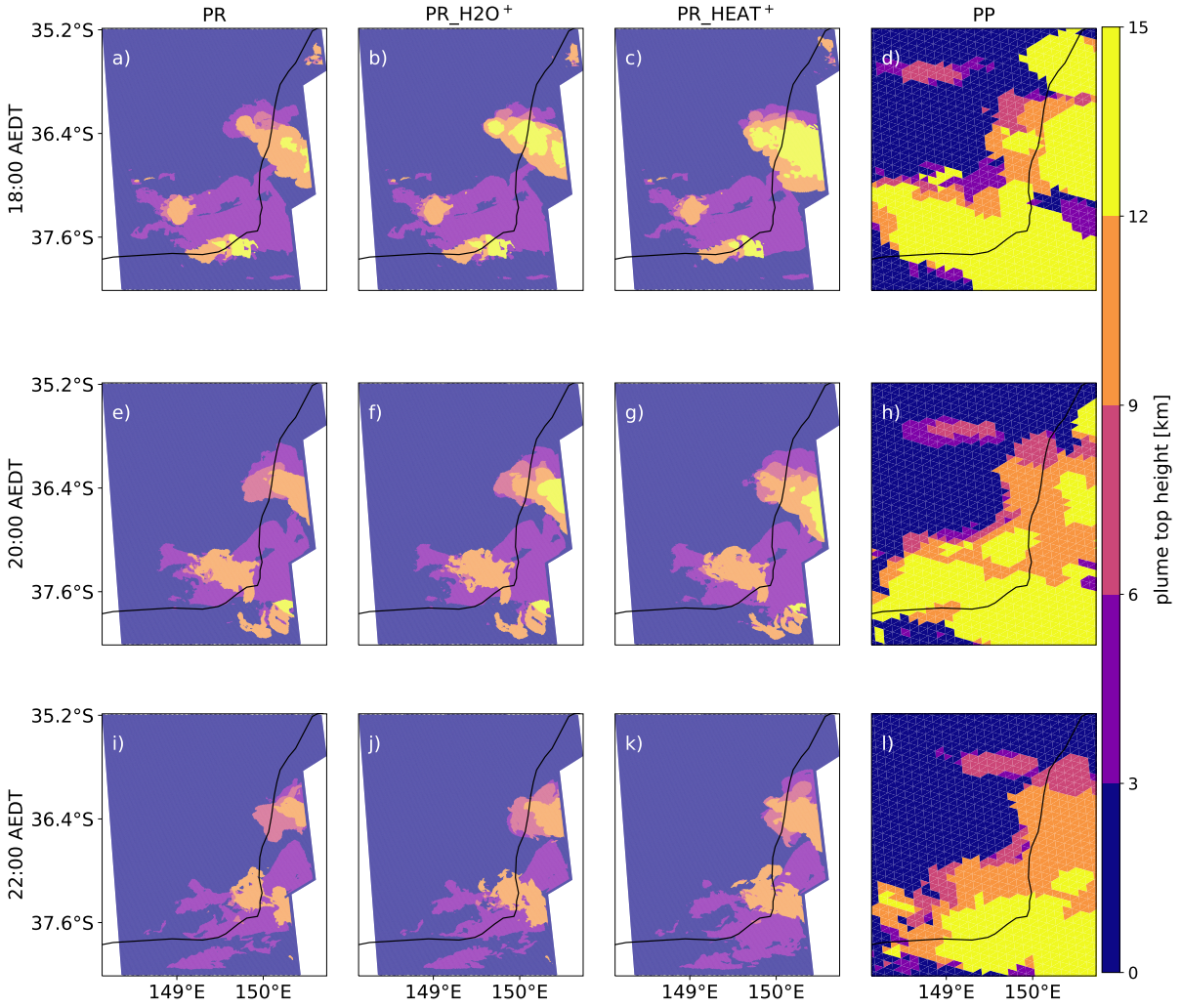

Figure 5.4.: Aerosol plume top height on the 30th of December 18:00 AEDT for a) experiment PR, b) PR_H2O$^+$, c) PR_HEAT$^+$, and d) PP, at 20:00 AEDT for e) PR, f) PR_H2O$^+$, g) PR_HEAT$^+$, and h) PP and at 22:00 AEDT for i) PR, j) PR_H2O$^+$, k) PR_HEAT$^+$, and l) PP.

above 12 km are already transported out of the domain in the experiments PR, PR_H2O$^+$, PR_HEAT$^+$. In PP aerosols are largely distributed above 12 km in the south-east of the domain.

Next, it is analyzed if sensible heat and moisture release by the fire enables moist convection. Figure 5.5 displays the column integrated aerosol concentration and the liquid water path (LWP) and ice water path (IWP) in the area of the aerosol plume for the 30th of December, 16:00 AEDT. The column integrated aerosol mass is similar in all experiments. The largest column concentrations are around 36.5°S and 150.0°E. The columns in this area also have the largest variations. This is underlined by the maximum values, which are 0.8 g m^{-2}, 1.1 g m^{-2}, 1.0 g m^{-2} and 1.5 g m^{-2} for PR, PR_H2O$^+$, PR_HEAT$^+$ and

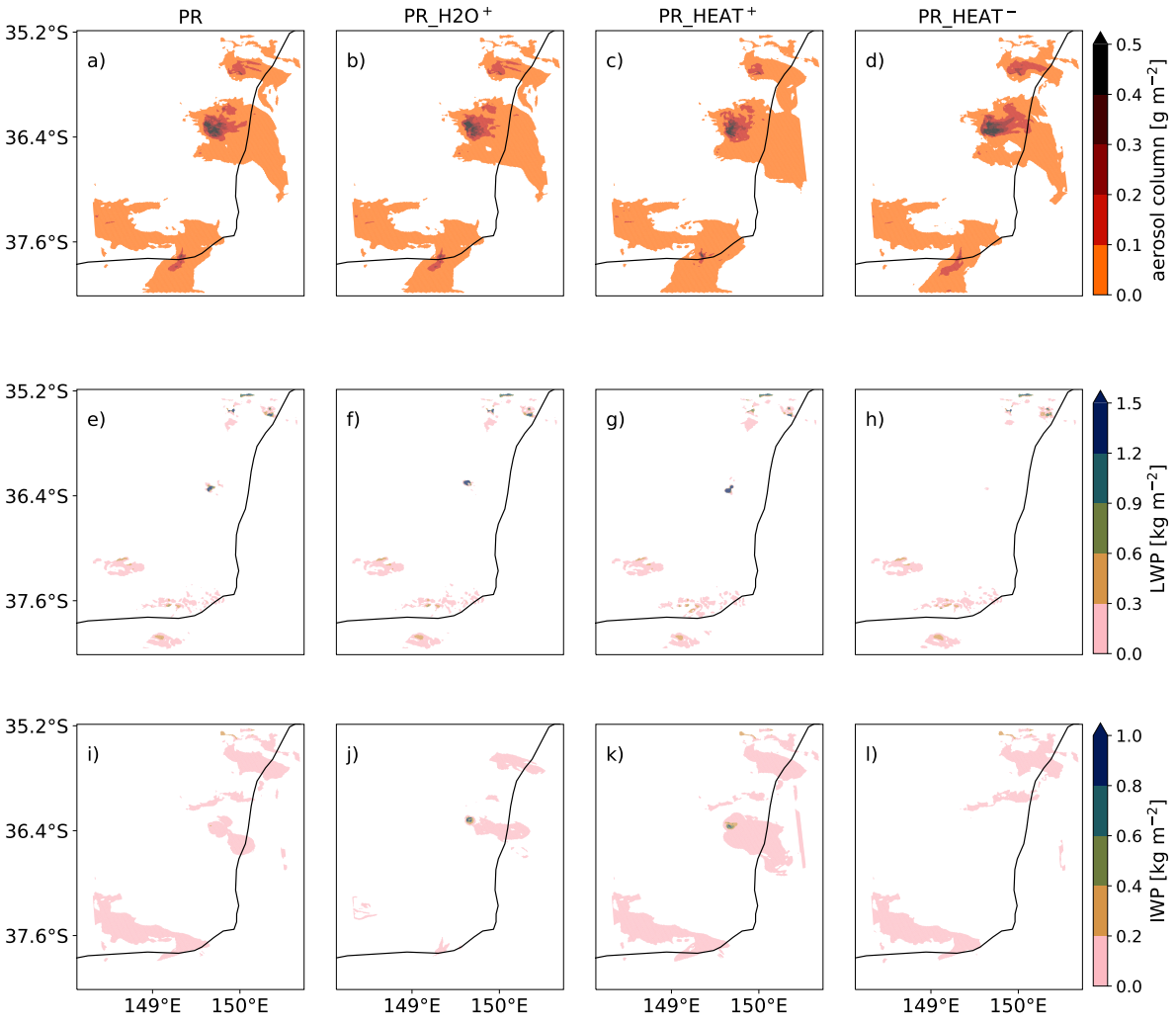

Figure 5.5.: Column integrated aerosol mass in the top row for a) experiment PR, b) PR_H2O$^+$, c) PR_HEAT$^+$, and d) PR_HEAT$^-$, the LWP in plume area for e) PR, f) PR_H2O$^+$, g) PR_HEAT$^+$, and h) PR_HEAT$^-$, and IWP in the plume area for i) PR, j) PR_H2O$^+$, k) PR_HEAT$^+$, and l) PR_HEAT$^-$. All shown for the 30th of December at 16:00 AEDT.

PR_HEAT$^-$, respectively. With reduced sensible heat release (PR_HEAT$^-$) the peak concentration is highest and the plume spreads mostly eastward.

The second row displays the LWP in the plume area, the overall pattern is again similar for all experiments. It shows liquid clouds at the north-eastern boundary of the domain and in the southern part of the domain. Here, the area around 36.5°S and 150.0°E shows the biggest differences again. In the experiments PR, PR_H2O$^+$ and PR_HEAT$^+$, cloud water is simulated that correlates with the location of the fire and the smoke plume. In experiment PR_HEAT$^-$, cloud water is rare. The third row of figure 5.5

shows the IWP in the area of the plume. The overall pattern is again similar in all experiments. The area around 36.5°S and 150.0°E is again noteworthy. Experiments PR, PR_H2O$^+$ and PR_HEAT$^+$ show cloud ice, which is not simulated in PR_HEAT$^-$. In this region the IWP reaches to up to 0.74 kg m^{-2}, 1.25 kg m^{-2} and 1.33 kg m^{-2} for PR, PR_H2O$^+$ and PR_HEAT$^+$, respectively.

In the next figure the impact of moisture and heat release by the fire and their sensitivity on the plume height is analyzed and compared to the plume-parameterizing simulation. Figure 5.6 displays the plume top height and the plume mass weighted height. Here the plume is defined as every grid point that exceeds an aerosol mass mixing ratio of 50 μg kg^{-1}. This threshold is 10 times higher than the threshold used for figure 5.4. The higher concentration threshold has little effect on the mass weighted height. For the plume top height the effect is also small, but reduces fluctuations. At around 08:00 AEDT, the plume top height in PP increases from 1.0 km to a plume top height of 13.9 km at 15:00 AEDT. The top height starts decreasing around 19:00 AEDT to 11.8 km at the end of the simulation. The plume top height

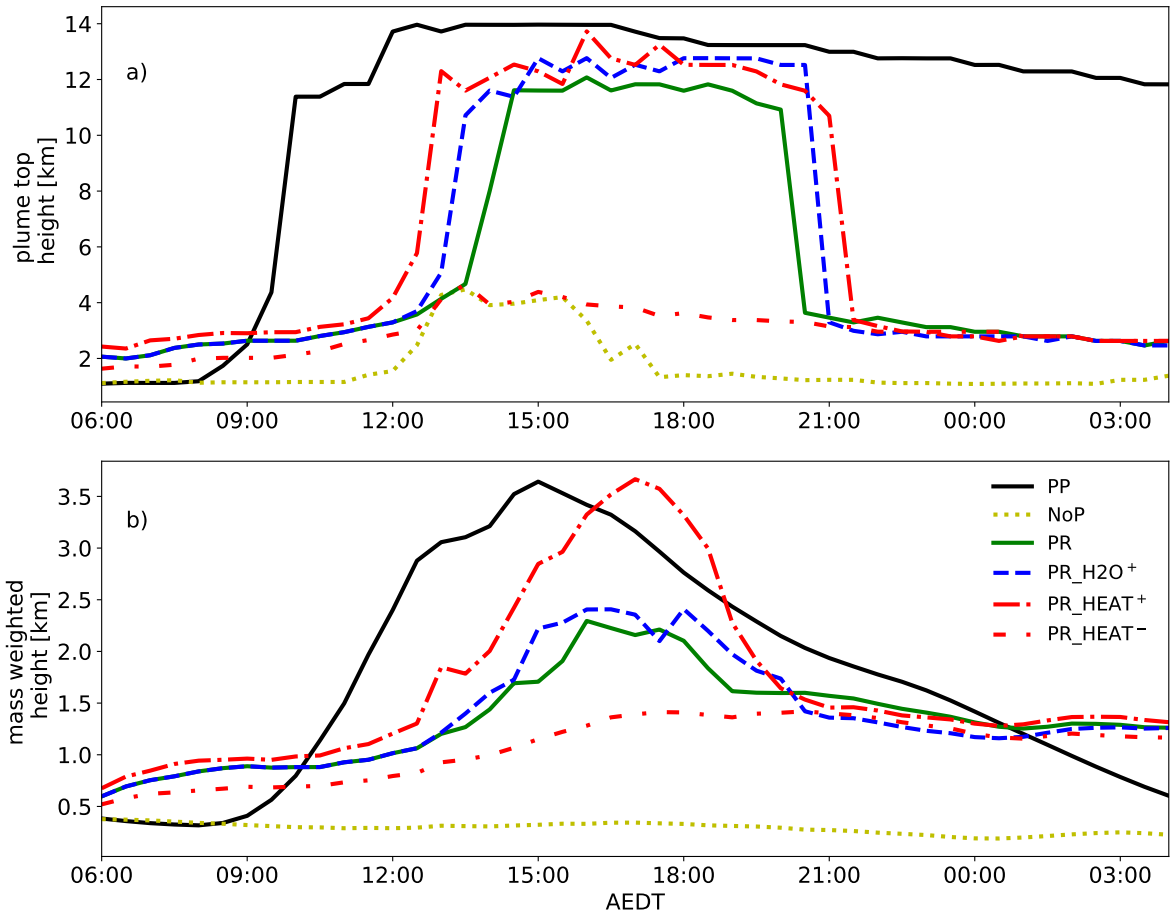

Figure 5.6.: Temporal evolution of a) the plume top height and b) mass weighted height for the different experiments. The plume is defined as grid cell exceeding 50 μg kg^{-1}. The black line displays the PP experiment, yellow dotted displays NoP, green displays PR, blue dashed displays PR_H2O$^+$, red densely dashed dotted displays PR_HEAT$^+$, and red loosely dashed dotted displays PR_HEAT$^-$.

in NoP is below 1.5 km throughout the simulation except between 12:00 and 17:30 AEDT. During this time the plume rises to a maximum height of 4.5 km. Experiment PR has a larger plume top height of 2 km from the beginning onward. The plume top height increases steeply at 13:00 AEDT to a maximum height of 12.1 km. At 20:00 AEDT the plume top height declines to 3.6 km and slightly decreases till the simulation ends. The profile of experiment PR_H2O$^+$ shows a similar trend to experiment PR. There is also a steep increase and decline, but the increase already starts at 12:00 AEDT with a maximum height of 12.8 km and declines at 21:00 AEDT. The sensitivity tests for the sensible heat release show two diverging profiles. Increasing the sensible heat release in PR_HEAT$^+$ shows a similar profile to PR and PR_H2O$^+$, but the initial plume top height is 2.4 km. There is a steep increase at 11:00 AEDT with a maximum height of 13.2 km and a steep decline at 22:00 AEDT. Experiment PR_HEAT$^-$ shows no steep increase nor decline. The initial plume top height of 1.6 km increases to 4.4 km at 14:00 AEDT and declines constantly to 2.5 km at the end of the simulation.

Figure 5.6 b shows the mass weighted height for the different experiments, to not only describe the top heights reached but evaluate how high the majority of the aerosols is transported. In experiment PP, the mass weighted height increases steeply after 09:00 AEDT to 3.7 km at 15:00 AEDT and then decays steadily. The mass weighted height in experiment NoP remains below 0.7 km throughout the whole simulation with slightly increased heights between 12:00 and 20:00 AEDT. In PR, the mass weighted height increases constantly from the start of the simulation till 16:30 AEDT and remains around 2.3 km till 18:00 AEDT. There is a decay afterwards to 1.3 km at the end of the simulation. Experiment PR_H2O$^+$ shows a similar profile to PR, with a slightly steeper increase to a maximum mass weighted height of 2.4 km and a decay to 1.2 km. Experiment PR_HEAT$^+$ shows a steep increase from 12:00 to 17:00 AEDT, with a maximum altitude of 3.7 km and a steep decay till 21:00 AEDT to 1.3 km. The mass weighted height in experiment PR_HEAT$^-$ increases till 18:00 AEDT from 0.5 km to 1.4 km and re-

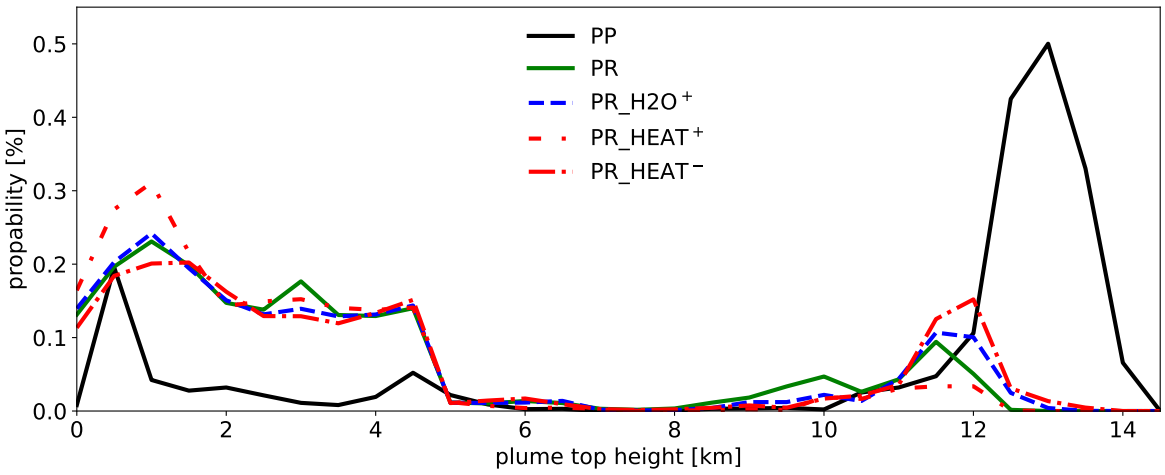

Figure 5.7.: Probability density function plume top heights at 18:00 AEDT, experiments PP, PR, PR_H2O$^+$, PR_HEAT$^-$ and PR_HEAT$^+$in black, green, blue dashed, red loosely dash dotted and dense dash dotted, respectively.

mains around this height afterwards.

Figure 5.7 displays the probability density function of the plume top heights at 18:00 AEDT. The plume is defined as every grid point that exceeds an aerosol mass mixing ratio of 1 μg kg^{-1}. Experiment PP displays 3 peaks, 2 local peaks at 0.5 km and 5.0 km. The largest peak is at 13.0 km. The experiments PR, PR_H2O^{+}, PR_HEAT^{+}, and PR_HEAT^{-} show similar trends to each other. The probability of plumes between 0.0 km and 5.0 km is high with a peak at 1.0 km and decreases rapidly for top heights up to 8.0 km. The experiments PR, PR_H2O^{+}, PR_HEAT^{-}, and PR_HEAT^{+} peak again at 11.5 km, 11.5 km, 12.0 km and 12.0 km, respectively. PR_HEAT^{-} shows the largest differences with the most pronounced peak at 1.0 km and only a small increase around 12.0 km.

Discussion

First, some general uncertainties should be discussed, starting with the GFAS data set. The GFAS data is based on the MODIS FRP, which is impacted by clouds, dense aerosol plumes, and overpass times. Figure 5.5 shows that both a dense aerosol plume and clouds are simulated in the area of the fires. This agrees with satellite observation and is shown in chapter 7 and further indicates possible sources of errors. MODIS is a polar orbiting satellite and it is assumed that the 3-4 overpasses a day, which corresponds to an 6-8 hours of observation, represent an adequate diurnal cycle of the fire. However, it is possible that fire peaks are not captured and therefore underestimated. This problem has been outlined before, for example by Li et al. (2021a). The emission fluxes provided by GFAS are directly related to the FRP and include the uncertainties of the measured FRP, and the uncertainties that relate to the assumed species-specific emission fluxes.

The implementation of the moisture release depends on three inputs from GFAS with further uncertainties in the weighting factors. It is assumed that the combustion rate is equal to the dry fuel weight, which is a rough approximation. Further, a fuel moisture of over 70 % is high compared to other publications, for example Clark et al. (2004) assume fuel moisture contents of 7 % to 20 %. Nevertheless, the moisture release is 20 times smaller in comparison to the plume-rise model and given that measurements are rare and mostly limited to laboratory studies, this implementation is based on my best available understanding.

The sensible heat release relies only on the GFAS FRP and a weighting factor, therefore the sources of errors are assumed to be smaller compared to the moisture release. In comparison to the plume-parameterizing simulation the maximum sensible heat flux is increased. Figure 5.1 outlines that this is only the case for a small fraction of the fire area. According to measurements on Texas grass fires by Clements et al. (2007), maximum sensible heat fluxes of 28.5 kW m^{-2} are reached within the smoke plume, with the estimated near-surface heat fluxes in the order of 1 MW m^{-2}. This suggests that the implemented sensible heat flux and the sensitivity experiment increasing sh_{fire} by 36 % are not unrealistically high.

The comparison of the plume-parameterizing and the plume-resolving simulations relay on very dif-

ferent assumptions. The buoyancy source in the plume-rise model is based on the vegetation type and the burned area, which remains unchanged throughout the simulation. The moisture emission in the plume-rise model is also constant. The variations in the emission height at a fixed location are therefore caused by the temporally variations in atmospheric stability. Based on this the plume-rise model returns an injection height, which can be hundreds of meters above the ground. The weighting function of the diurnal cycle is only applied for the aerosol emission. In comparison, the plume-resolving simulation determines the buoyancy through the FRP and moisture release and both are weighted with a diurnal cycle. the sensible heat and moisture release affect the meteorology thus, the atmospheric stability. The aerosols are constantly emitted in the lowermost model level. The elevation of the plume is determined by the atmospheric stability and the buoyancy created by sensible and latent heat release.
It is shown that these two different approaches lead to comparable plume top heights (outlined in figure 5.4 and 5.6 a) and both capture the diurnal cycle well (figure 5.3 and 5.6). In all experiments the aerosol masses remain lower during the night, while the atmosphere is more stable, and increase during the day as the atmosphere becomes unstable. Larger differences between PP and PR are occurring in vertical distribution. As displayed in figure 5.3 the majority of the aerosol mass in PR remains below 3 km and the mass weighted height in 5.6 b indicates lower aerosol masses during the day for PR. This is reasonable, as the aerosol masses are constantly emitted in the lowermost model level and buoyancy is largest during the day. Heat and moisture release elevate aerosol masses in PR compared to PP during the morning and evening. Despite the reduction in heat and moisture release due to the diurnal cycle, sufficient buoyancy is generated. This buoyancy is not a result of the background meteorology, as demonstrated by the comparison to NoP in Figure 5.6. In PP the aerosols are injected in the lowermost level during the night and because the plume-rise model does not impact the host model's meteorology the plume remains low.
The sensitivity study is designed to test the variability between the assumptions made in the plume-resolving simulation and the plume-parameterizing simulation. Figure 5.4 shows large differences in the distribution of the plume top heights between the plume-resolving simulations and PP, especially in the bottom half of the domain. In the plume-resolving simulations, the largest plume top height overlap with the areas of largest FRP. In PP the plume top heights are additionally elevated over a large area, originating from the fires at the western boundary of the domain. Figure 5.1 shows that the emissions at the western boundary of the domain are reduced for the plume-resolving simulations. The FRPs in this area are partly half of the FRPs in the center of the domain, which directly affects the buoyancy in PR, PR_H2O$^+$, PR_HEAT$^+$, and PR_HEAT$^-$. his effect is weaker in PP. In the plume-rise model, the GFAS FRP does not directly affect the heat released by the fire but serves as a scaling factor for the burned area. The pronounced elevation of the plumes in PP results in a narrow range of simulated plume top heights. Figure 5.7 shows that most plumes reach top heights above 10 km, with only a few remaining low. Notably, experiment PP already incorporates the scaling factor for the burned area proposed by Val Martin et al. (2012) to address the underestimation of the dynamic range of plume heights. The plume-rise model parameterizes moist convection, and the high probability of plumes above 10 km

implies that pyro-convective clouds are parameterized in most of the fire area. The plume-resolving experiments have a wider range of plume top height. There is a high probability for plumes to have any top height below 5 km and then again for heights above 8 km. The fast vertical transport of hot and moist air masses above 5 km is likely to cause cloud formation (liquid and ice) and create additional buoyancy lifting the aerosol masses above 8 km, creating this gap. Figures 5.4 and 5.5suggest that in the plume-resolving simulations, moist convection occurs only in the center of the domain. It should be noted that aerosol-cloud interaction is not accounted for. Therefore, cloud ice is formed through homogeneous freezing, which requires temperatures below 235.15 K (-38°C) (Hoose and Möhler, 2012). This temperature is reached above the fire area around 7 km. Based on figure 5.5 it can be concluded that the plume rise above 12 km is driven by moist convection. The absence of clouds in experiment PR_HEAT$^-$ therefore leads to the hypothesis that there is not enough buoyancy for moist convection when reducing the sensible heat flux. This is underlined by the lower plume top and mass weighted height (figure 5.6). Further, the spreading of the aerosol plume in the center of figure 5.4 c is less circular and denser. This indicates that in contrast to PR, PR_H2O$^+$, PR_HEAT$^+$ the plume is not lofted to higher levels with different wind patterns. The LWP and IWP placed within the plume area in figure 5.5 is smallest in PR and largest in PR_HEAT$^+$. This shows that even without additional moisture release there is sufficient available moisture for pyro-convective clouds. The additional moisture in experiment PR_H2O$^+$ leads to more cloud ice in that region, but the impact on the plume height is small compared to the sensible heat release, as outlined in 5.6 b.

This increase in cloud formation is not generally observed. The fires at the western border of the domain and the south-eastern coast create noise in the LWP and IWP but changes are neglectable.

For PR_HEAT$^-$ there is little cloud formation in the areas of the fires, therefore hardly moist convection. This implies that the triggering of moist convection causes this steep increase in plume top height, as seen in figure 5.6. An increase in heat and moisture release enables moist convection earlier in the day which transports more aerosol masses over a longer time period to elevated heights. Additionally, it can be concluded that the plume height is more sensitive to the release of sensible heat than the release of moisture by the fire. The total effect a typical moisture release is smaller, although the up-scaling factor for the moisture emission of 20 is nearly 15 times the scaling factor of the sensible heat releases (factor 1.34). This agrees with other findings e.g. Luderer et al. (2006) and Thurston et al. (2015). Overall ICON-ART is able to simulate pyro-convection and even pyro-cumulus formation with a grid spacing of 600 m and resolved convection with the implemented sensible heat and moisture release, for this real case scenario. Nevertheless, the fine grid spacing is computationally expensive and limits the domain to a comparably small area. This is outlined by figure 5.4, which shows that the elevated plume is transported out of the domain within hours. The elevated aerosol masses in the plume-resolving experiments (figure 5.4) are transported out of the domain between 18:00-22:00 AEDT, this matches the steep decline in plume top height in figure 5.6. To overcome this limitation, a plume-parameterizing setup with a larger

domain is used in the following and extended by including sensible heat release, moisture release and aerosol-radiation interaction, to see if this improves the representation of the plume evolution.

6. Limited area simulations with plume-rise model

6.1. Simulation setup

In a next step the implemented features (moisture and sensible heat release by the fire and aerosol-radiation interaction) are tested in limited area mode simulations with parameterized convection and the plume-rise model. Although the plume-rise model considers buoyancy through sensible and latent heat release, there is no feedback to the atmospheric dynamics in the host model. Through the parameterized emission height the aerosols are injected in elevated levels. The aim is that the implementations extend the range of plume heights and make it possible to simulate reported emissions up to the lower stratosphere. Therefore, a set of five experiments is performed. The domain reaches from south-east Australia to New Zealand. The area of the domain is displayed in figure 6.1. The grid spacing is approximate 6.6 km and boundary conditions are read in every 3 hours. The domain is 30 km high with 70 vertical levels increasing with height. The simulations start on the 30th of December 2019 00:00 UTC and continues for nearly three days (till 1st of January 2020 22:00 UTC). The chemical tracers CH_4, C_2H_6, C_3H_8, CH_3COCH_3, CO, NH_3, NO_2, SO_2, DMS, HNO_3 are initialized with CAM-Chem data (Buchholz et al., 2019; Emmons et al., 2020). A simplified OH-chemistry mechanism is used to simulate atmospheric

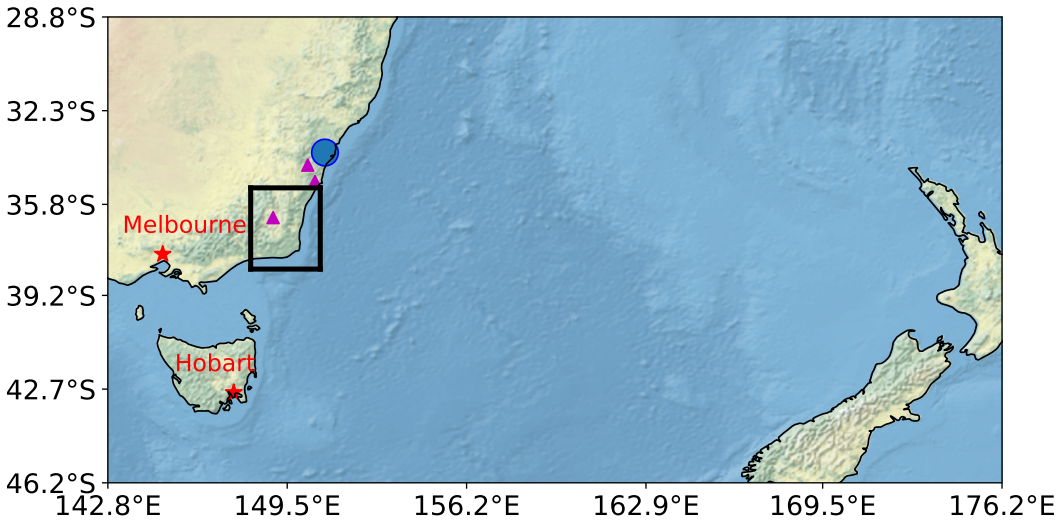

Figure 6.1.: Display of the simulated domain. The black box outlines the domain of the plume-resolving simulation. The red stars make Melbourne and Hobart, the locations of the radiosonde launches. The blue circle displays the area of the air quality measurements and the magenta triangles display the locations of AWS used in 6.3.4.

Table 6.1.: Overview of the performed experiments.

Experiment	Moisture release	Heat release	Aerosol-radiation interaction
REF	×	×	×
H2O	✓	×	×
HEAT	×	✓	×
ARI	×	×	✓
ALL	✓	✓	✓

chemistry (Weimer et al., 2017). This mechanism further includes C_5H_8, CO_2 and OCS. In the simulation, the formation of new particles through nucleation is possible. Particle coagulation and condensation of gaseous species is enabled. ISORROPIA II is used to calculate the gas to particle partitioning. The inorganic soluble species accounted for in these simulations are H_2O, SO_4, NO_3 and NH_4. The emission of the biomass burning aerosols is done as explained in section 4.4. 6 % of the aerosol mass is emitted in the smaller Aitken mode and 94 % in the accumulation mode. This is consistent with the findings from McClure et al. (2020). The particles are emitted in the Aitken mode with a median number diameter $d_n = 20$ nm and standard deviation $\sigma = 1.7$ and in the accumulation mode with $d_n = 70$ nm and $\sigma = 2.0$.
The emission fluxes for aerosols and the parameterization of moisture and heat release are again based on GFAS data (CAMS, 2021). For this setup the fire emission data from GFAS and the background chemistry are read in every day at 00:00 UTC. The FRP of the GFAS data set is remapped to the ICON grid and displayed from the 30th of December to the 1st of January in figure 6.2. The GFAS emission flux is proportional to the FRP, therefore figure 6.2 indicates not only the grid cells with a detected fire but also the locations of higher and lower emission fluxes. On the 30th of December the FRP reaches up to 144 W m^{-2}, on the 31st up to 47 W m^{-2} and on the 1st of January up to 10 W m^{-2}.
The first simulation is a reference simulation (REF), which is set up as explained above. The second experiment is named H2O and includes the moisture release by the fire. The third experiment is also based on the REF setup but includes sensible heat released from the fire and is further referred to as HEAT. The fourth experiment, ARI, is again based on REF but includes aerosol-radiation interaction. The last experiment is the ALL experiment that includes heat and moisture release from the fire as well as aerosol-radiation interaction. All the experiments are summarized in table 6.1. In the following, the results are displayed in Australian Eastern Daylight Time (AEDT), which corresponds to UTC + 11 hours, although eastern part of the domain is in a different time zone, New Zealand Daylight Time (NZDT), which corresponds to UTC + 13 hours.

6.2. Evaluation

Firstly, the meteorological situation is evaluated. Therefore, the ICON-ART REF simulation is compared to Automated Weather Stations (AWS) and radiosonde data from Melbourne and Howard airport. The AWS data is purchased from the Bureau of Meteorology's "Climate Data Services" division

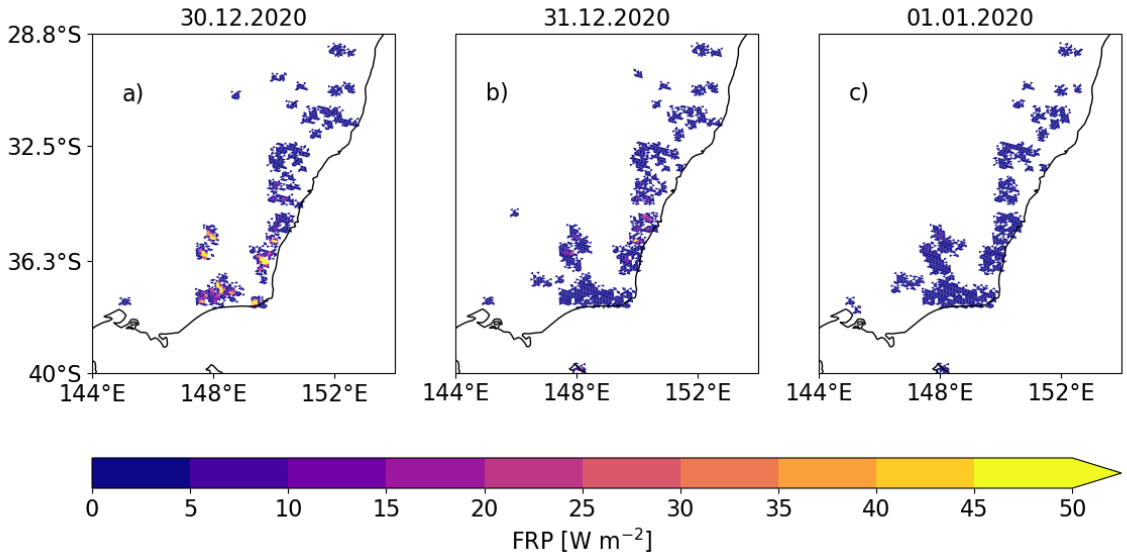

Figure 6.2.: Display of the GFAS fire radiative power (FRP) (CAMS, 2021) remapped to the ICON grid on the a) 30th, b) 31st of December 2019 and c) the 1st of January 2020. Generated using Copernicus Atmosphere Monitoring Service information [2023].

(BOM,2020d) in January 2020 and converted from the original text format to netCDF for this work by Dr. Jeremy Silver (jeremy.silver@unimelb.edu.au). The radio sounding data is downloaded from the web page of the University of Wyoming (`https://weather.uwyo.edu/upperair/sounding.html`, last access: 14.02.2024). Figure 6.3 shows the radio soundings at Melbourne and Hobart for the specific humidity and temperature in comparison with the ICON model two days after the simulation started. Overall, the soundings are in good agreement with the simulation. In Melbourne the temperature profile is in very good agreement with the soundings, only above 15 km there are some differences up to 5°C. These differences can result from the horizontal transportation of the radiosonde, which moves it to a different grid cell. Unfortunately, coordinates of the radiosondes are not provided. The specific humidity profiles are also in good agreement with the soundings in Melbourne. The simulation underestimates the specific humidity below one kilometer. The measurements between 2-7 km are noisy, this is presumably caused by measurement errors, e.g. passing through a cloud.

The temperature profile of ICON and the radiosonde in Hobart are in very good agreement. The simulated specific humidity from the ground to 4 km is approximately 1 g kg^{-1} above the measurements. The fast decline measured between 4-5 km is captured well. More radiosonde measurements are compared to the ICON simulation in appendix A.1 to A.4 and are generally in good agreement. The relative humidity patterns in figure 6.4 are also captured well. There are again single differences between measurement and simulation, exceeding 70 % relative humidity, but the mean differences are 11.0 % and 3.8 % for the respective time step. Based on all this, it can be concluded that ICON captures the meteorological condition agreeably.

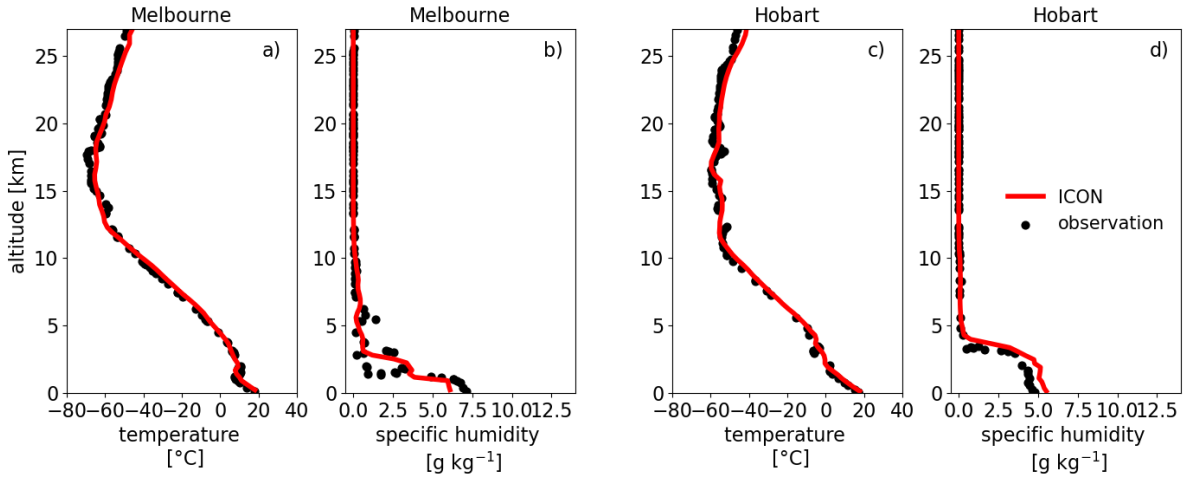

Figure 6.3.: Comparison of radio soundings (black dots) and ICON simulated (red lines) a) temperature in Melbourne, b) specific humidity in Melbourne, c) temperature in Hobart and d) specific humidity in Hobart on the 1st January 2020 11:00 AEDT.

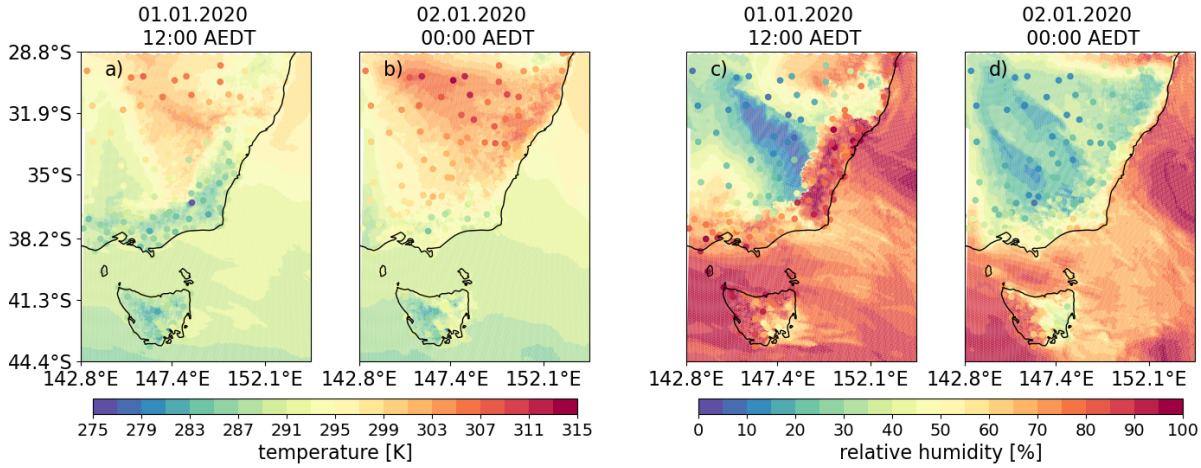

Figure 6.4.: Measurements of automated weather stations (colored dots) compared to REF variables in the lowermost model level (filled contours). a) temperature and b) relative humidity on the 1st of January 2020 12:00 AEDT and c) temperature and d) relative humidity on the 2nd of January 00:00 AEDT.

In the next step the emission flux is evaluated. Therefore, air quality measurements from CAR's National Air Pollution Monitor Database (NAPMD) are used (CAR 2021; Riley et al., 2020). Figure 6.5 displays the three-hourly mean of PM2.5 concentration measured by the air quality monitors and the three-hourly mean aerosol concentration in the respective grid cell. All stations are located close to Sydney, a region that was strongly affected by bushfire smoke in December 2019. The region is marked in figure 6.1 with the blue circle. The six graphics in figure 6.5 show some differences between measurements and simulation in terms of the timing of the peak values, but the order of magnitude of the concentrations agrees well. The simulation underestimates the concentration in the first 12 hours, which can be ex-

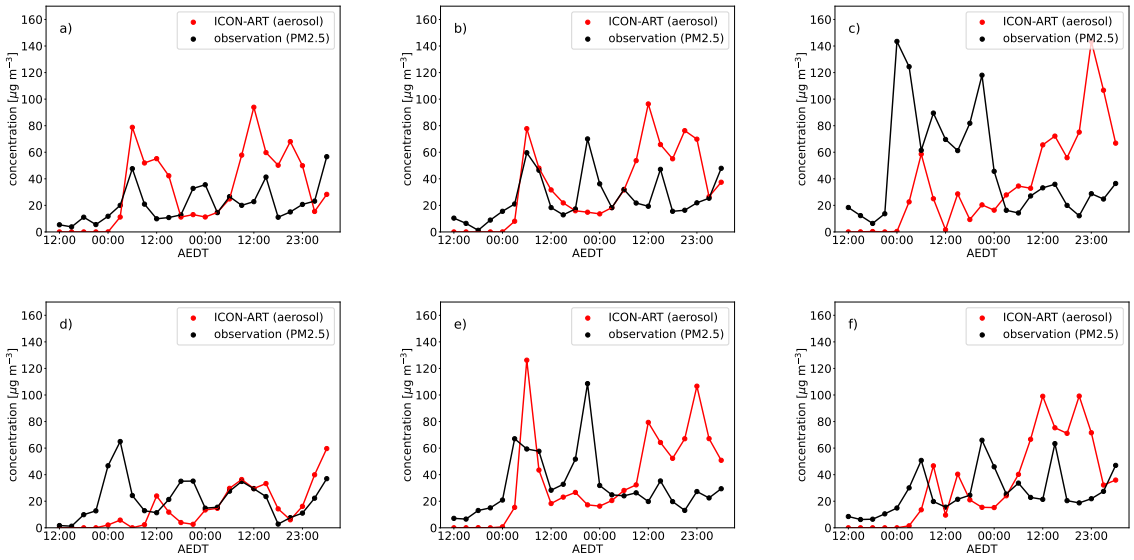

Figure 6.5.: Comparison 3-hourly mean PM2.5 air quality measurements and simulated ICON-ART organic and black carbon at 6 different locations. Detailed information about the stations can be found in appendix A.1 and A.2 for the stations-ids 32, 42, 45, 13, 373 and 369.

plained by a lack of background aerosol and the time it takes for the particles to be transported from the simulated fire area to the location of the measurements. As analyzed above, the meteorology agrees well with the measurements overall, but with larger differences at individual points. This can explain shifts, missing and overestimated of peak values due to slight shifts of the simulated plume compared to the real one. Further, it has to be noted that the simulation only accounts for biomass burning aerosols, whereas the measurements account for all particles smaller than 2.5 μm. Nevertheless, it is concluded that the concentration magnitude of the observations and simulation agree well. Therefore, the GFAS black and organic carbon with the suggested factor of 3.4 is a valid assumption for the biomass burning emission flux in this study.

6.3. Experiments and results

6.3.1. Reference simulation

Figure 6.6 displays the spreading of the aerosol plume for different time steps. The isosurfaces indicate different aerosol mass mixing ratios. 12 hours after simulation start, the plume is close to the emission source and mainly distributed in height. In the following 12 hours the plume is transported to the south-east-east by the passing cold front (explained in section 3.2). The plume in figure 6.6 c and d shows the lifting of the plume by the cold front as it reaches New Zealand. In figure 6.6 e parts of the plume are already transported out of the domain. Further, the plume heights and concentrations close to the source decrease, this agrees with the declining FRP assimilated by GFAS, shown in figure 6.2.

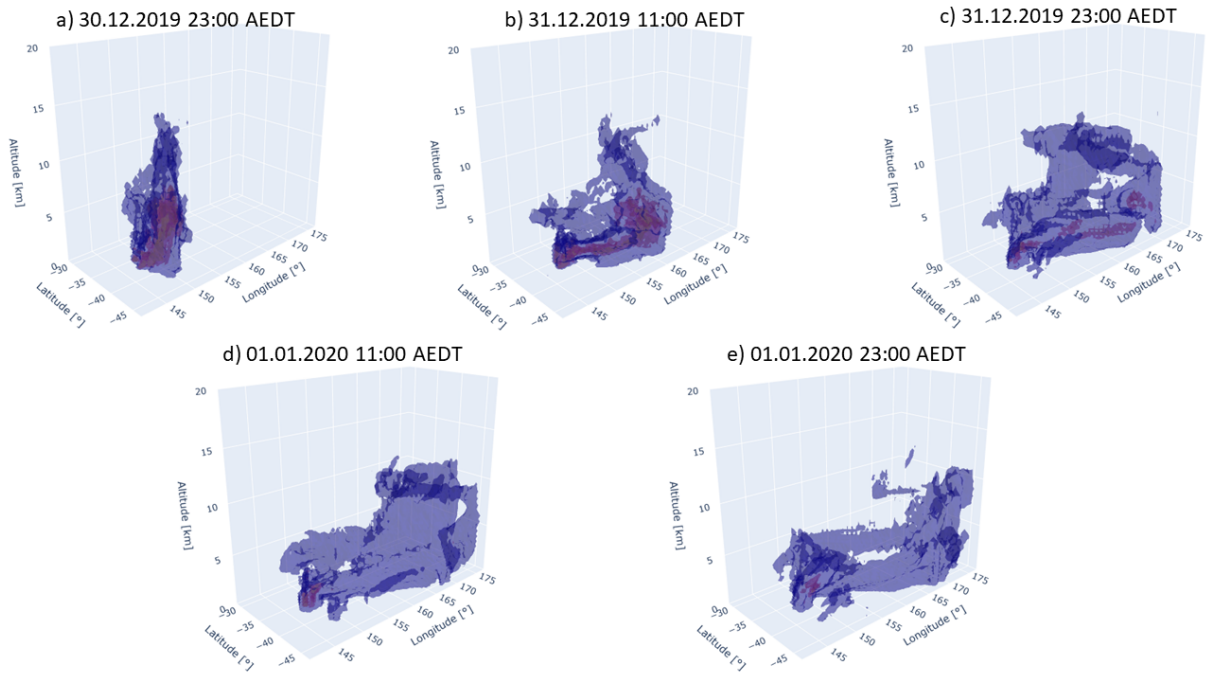

Figure 6.6.: Mass mixing isosurfaces of the biomass burning aerosols in the REF experiment. The purple isosurface is at 10 μg kg^{-1}and the orange one at 500 μg kg^{-1}. a) on the 30th of December 23:00 AEDT, b) 31st of December 11:00 AEDT, c) 31st of December 23:00 AEDT, d) 1st of January 12:00 AEDT, e) 1st of January 23:00 AEDT.

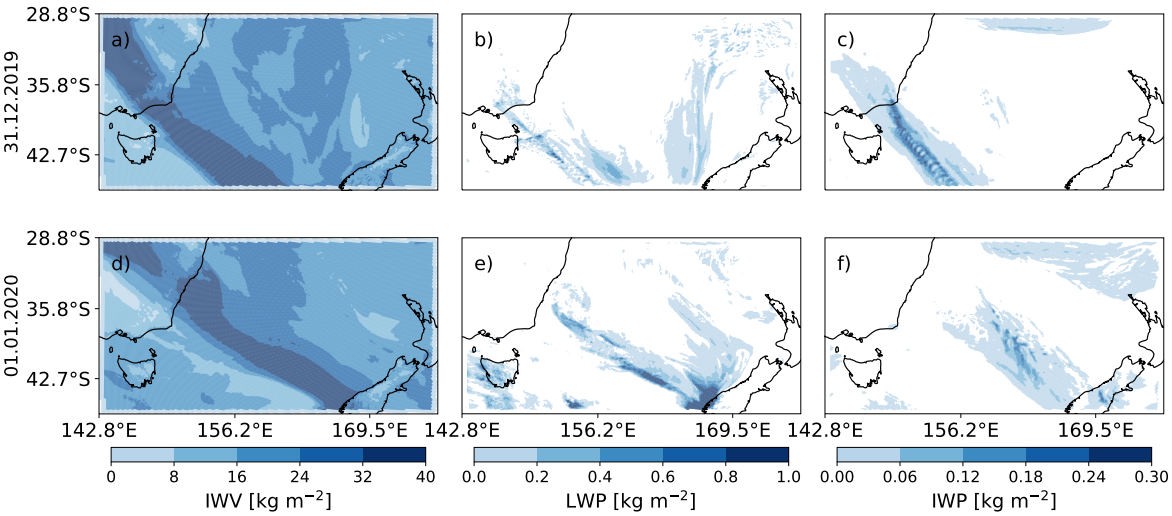

Figure 6.7.: Display of the a) IWV, b) LWP, and c) IWP on the 31st December 11:00 AEDT and d)-f) on the 1st January 11:00 AEDT respectively.

With the passing cold front comes a moisture band and convective clouds, this is shown in figure 6.7. It shows the column integrated water vapor (IWV), LWP, and IWP on the 31st of December 11:00 AEDT

and the 1st of January 11:00 AEDT, respectively. The positions of the cloud and the moisture band correlate well with the passing cold font shown in the weather charts in figure 3.3.

6.3.2. Impact of moisture release

This section focuses on the impact of moisture release by the fire on the plume evolution and cloud formation. The theoretical hypothesis is that additional moisture released by the fire can lead to more widespread super saturation and therefore increase cloud formation. Figure 6.8 displays the mean vertical profiles above the fire location on the 30th of December 15:00 AEDT. In figure 6.8 a the aerosol concentrations show two peaks for both experiments, one at around 5 km and one at approximately 1 km. It is notable that the lower peak in the H2O experiment is more pronounced compared to REF and the upper peak is smaller in H2O. Figure 6.8 b displays the difference in water vapor content (WVC) (H2O-REF), the profile is similar to the aerosol profile. The maximum increase is 1.2 g m^{-3} at around 5 km. Figure 6.8 c displays the sum of liquid water content (LWC) and ice water content (IWC). Between 4.5 km and 7 km there is a clear increase in the H2O experiment, with a maximum difference of 0.0065 g m^{-3} at 6 km. Figure 6.8 d shows a positive temperature difference (H2O-REF) between 5 and 10 km, with a peak of 0.03 K at 5.7 km. Below 5 km the mean temperature decreases up to -0.14 K at the surface layer. Figure 6.8 e displays the mean vertical wind above the fire area, which is positive between the surface and 15 km in both experiments, with small increases for the H2O experiment between 1.8 and 11 km. There are two peaks, one at 2.6 km, where the vertical wind is increased by 0.007 m s^{-1}, and the other at 8.7 km, where the vertical wind is increased by 0.008 m s^{-1} for H2O.

Figure 6.9 displays Hovmöller diagrams within the aerosol plume. This means that for every time step the aerosol column is calculated and for grid points that exceed an aerosol column threshold of 0.05 g m^{-2} the mean vertical profile is calculated. As the plume spreads the grid points that exceed the threshold

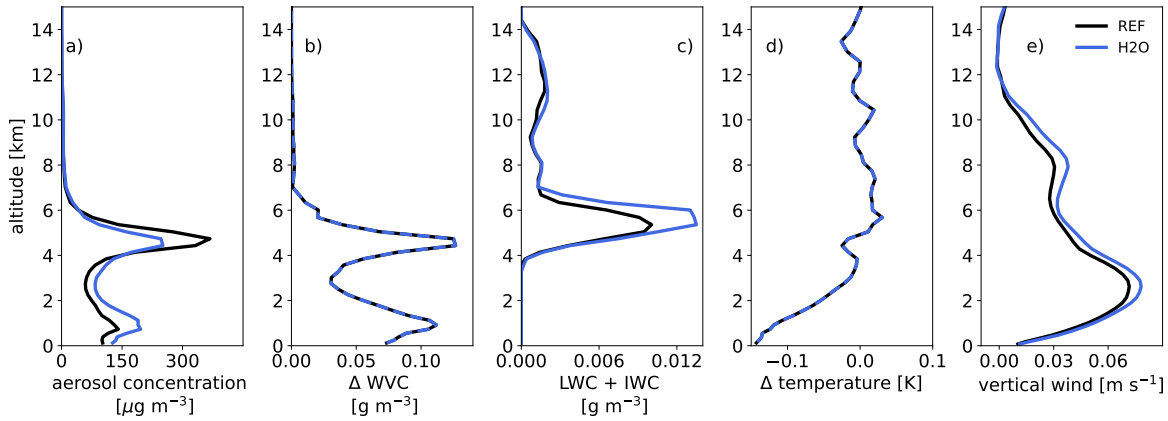

Figure 6.8.: Mean vertical profiles above grid cells with a fire on the 30th of December 15:00 AEDT for a) the aerosol concentration, b) difference in WVC, c) the sum of LWC and IWC, d) difference in temperature, and e) the vertical wind. The H2O experiment is displayed in blue and REF in black.

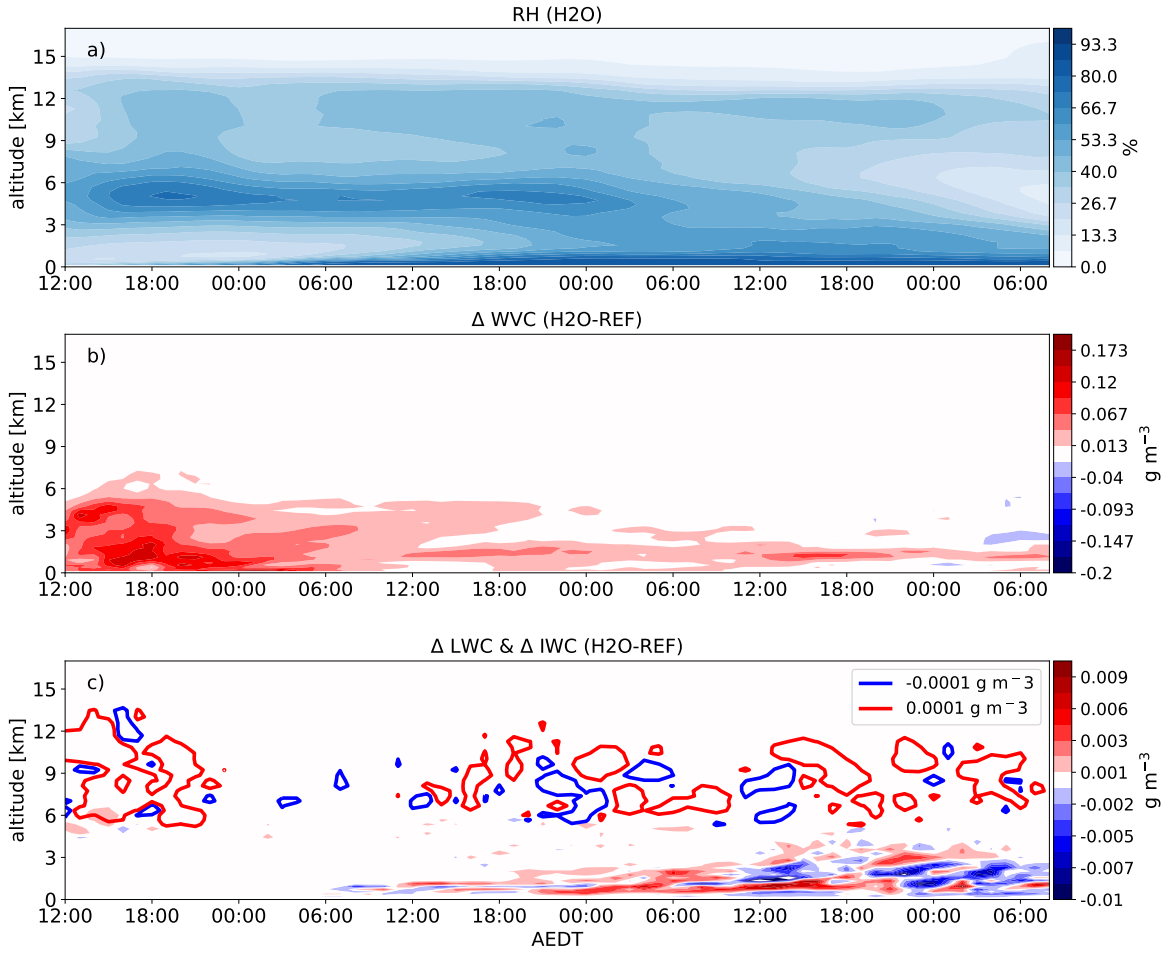

Figure 6.9.: Hovmöller diagram, averaged in plume area (grid cells that exceed an aerosol column of 0.05 g m^{-2}) for a) the relative humidity of the H2O experiment, b) the difference (H2O-REF) in WVC, and c) difference in LWC (filled contours) and IWC (contour lines).

increase and it is averaged over a larger area.

Figure 6.9 a shows the Hovmöller diagram of the relative humidity (RH) for H2O. RH is highest in the layers close to the surface. At the beginning of the simulation the relative humidity between 1.7 km to 6.2 km exceeds 50 %. Figure 6.9 b shows the in-plume difference in WVC (H2O-REF). There is an in-plume increase below 6 km throughout the simulation. The largest increases are recorded during the first 14 hours between the surface and 6 km. Figure 6.9 c shows an increase in LWC within the first 6 hours of the simulation at an altitude of 5-7 km. Afterwards changes in LWC remain below 4 km. The IWC increases between 6 km to 13 km altitude during the first 12 hours as well and throughout the rest of the simulations the changes appear noisy.

Discussion

Figures 6.7 and 6.9 outline that the mid-level moisture band, mentioned in section 3.2, is captured well in the model. The implemented moisture emission increases the WVC in the plume and above the fire area by up to 0.02 and 0.12 g m^{-3}, respectively. This is up to one order of magnitude lower then observations by Clements et al. (2007) and Kiefer et al. (2012), who report mass mixing ratio increases of 0.5-3.5 g kg^{-1} in the plume compared to ambient conditions. Based on the vertical profiles in figure 6.8, the variable qv_{fire} is released in regions with high relative humidity and pre-existing clouds. This release leads to supersaturation and the formation of additional clouds. The moisture emission below 3 km does not affect cloud formation. The Hovmöller diagram in figure 6.9 a indicates that the air is considerably dryer below 3 km. This is supported by figure 6.9 b and c, which show that the emission of qv_{fire} increases the WVC below 4 km and the LWC and IWC above 4 km during the first 24 hours of the simulation. The surface relative humidity (RH) increases as the plume moves over the ocean, where enhanced moisture flux from the surface to the atmosphere raises the RH in the lowest model layers. (figure 6.9 a). These processes take place in considerable distance from the fires. Nevertheless, the emission of qv_{fire} increases the WVC in these levels and therefore impacts the LWC.

The latent heat release through additional cloud formation leads to small increases in the temperature and the decreases below the clouds during the day. The latter is due to the reduction of solar radiation reaching the surface. The vertical wind increases in H2O, but the largest increases do not correlate with the altitudes of increased cloud formation. The wind increases most strongly at altitudes with initially high wind speeds and thus below the cloud layer. This indicates that cloud formation does not only increase due to the emission of qv_{fire}, but convection contributes as well. The averaged increase of the vertical wind above the fire is overall small. It is hypothesized that additional cloud formation would increase buoyancy and thus the plume height. However, figure 6.8 a shows a decrease in aerosol concentration at the upper peak and an increase below. Despite the vertical wind increasing above the fire, additional cloud formation reduces solar radiation, stabilizing the atmosphere. This stabilized atmosphere is then used to calculate the injection height, resulting in a reduced initial aerosol injection height. While the technical reasons for this are understood, in reality, pyro-convective clouds form from strong convection driven by latent heat from cloud formation. Clouds formed through additional moisture release do not result from pronounced updrafts and thus have little impact on plume height.

The impacts of moisture emission by the fire are strongest close to the source. This is outlined by the Hovmöller diagrams in figure 6.9. Although, it can be expected that the magnitude of the differences decreases over time, as the plume spreads and ambient air entrains. Further, the emissions decrease over time (as shown in figure 6.2). The changes in IWC only show a pronounced increase in the first 6 hours of the simulation. This underlines again that the impact of moisture release is strongest close to the source. Other changes in IWC are small and indicate a shift in cloud ice formation rather than a systematical change. The changes in LWC can be connected with the increased WVC in these areas but appear noisy.

The initially emitted moisture is small compared to the total water vapor mass in the plume and also entrained from the ambient air.

6.3.3. Impact of heat release

The simulation accounts for sensible heat release by the fire, which is expected to warm the air near the surface and create additional buoyancy. This buoyancy lifts the plume higher. While this effect is most pronounced near the fire source, it is anticipated to influence plume transport by increasing the initial plume height. This hypothesis is tested in the following analysis.
First, figure 6.10 displays a Hovmöller diagram of the mean vertical distribution within the plume. The calculation is the same as explained in section 6.3.2. The top image, figure 6.10 a displays the difference in mean temperature (HEAT-REF). The largest differences are near the surface within the first 1.5 hours. The in-plume mean difference increases up to 0.97 K. As in figure 6.9 the effects weaken over time. Nevertheless, there is an evident increase in temperature by up to 0.5 K within the first 24 hours between 5 and 11 km. Below and above this increase the temperature decreases. The largest decrease is around 15:00 AEDT close to the surface with -0.79 K. From 18:00 AEDT onwards the surface temperature in HEAT increases again compared to REF. In figure 6.10 b the changes in LWC and in IWC concentrations are displayed. The clearest differences are visible during the first 12 hours. The LWC increases by up to 0.02 g m^{-3} and the IWC by up to 0.01 g m^{-3}. Afterwards the differences in the IWC are isolated and small. The differences in LWC are in the same order of magnitude as the peak at the beginning of the simulation but positive as well as negative. The changes remain below 4 km. Figure 6.10 c displays the difference in aerosol concentration HEAT-REF and shows an obvious increase above 5 km from the start of the simulation onward. The maximum increase is 18.7 g m^{-3}. The HEAT experiment also shows increased aerosol concentrations near the surface. Between these periods of increase, the aerosol concentrations decrease. After 12 hours, the aerosol concentrations close to the surface continue to decrease. The difference in in-plume vertical wind velocity is shown in Figure 6.10 d, indicating a clear increase of up to 0.11 m s^{-1} for the HEAT experiment within the first 6 hours of the simulation, from the ground up to 12 km. As the plume spreads, the changes in in-plume vertical wind velocity become small.
Figure 6.11 a displays the ground temperature in REF 4 hours after the simulation start. The peak temperature is 39.5°C. Figure 6.11 e outlines the temperature changes in the fire area, which increase by up to 18 K in the HEAT experiment. Further, the temperature decreases by up to 13.0 K in the plume area. The plume top height in the REF experiment (figure 6.11 b) reaches a maximum of 14.4 km. This is 3.0 km lower than the maximum plume top height in the HEAT experiment (figure 6.11 f). The plume in REF remains closer to the source. In the HEAT experiment the plume is distributed more widely and transported further south-east. Figure 6.11 c displays the sum of LWP and IWP in REF. There are clouds at the east coast of Australia reaching over the ocean. Further, there are clouds along the NSW-VIC border and along the southern border of the domain. The HEAT experiment in figure 6.11 g has a similar pattern to REF, but with a pronounced increase in LWP and IWP in the fire areas, especially around

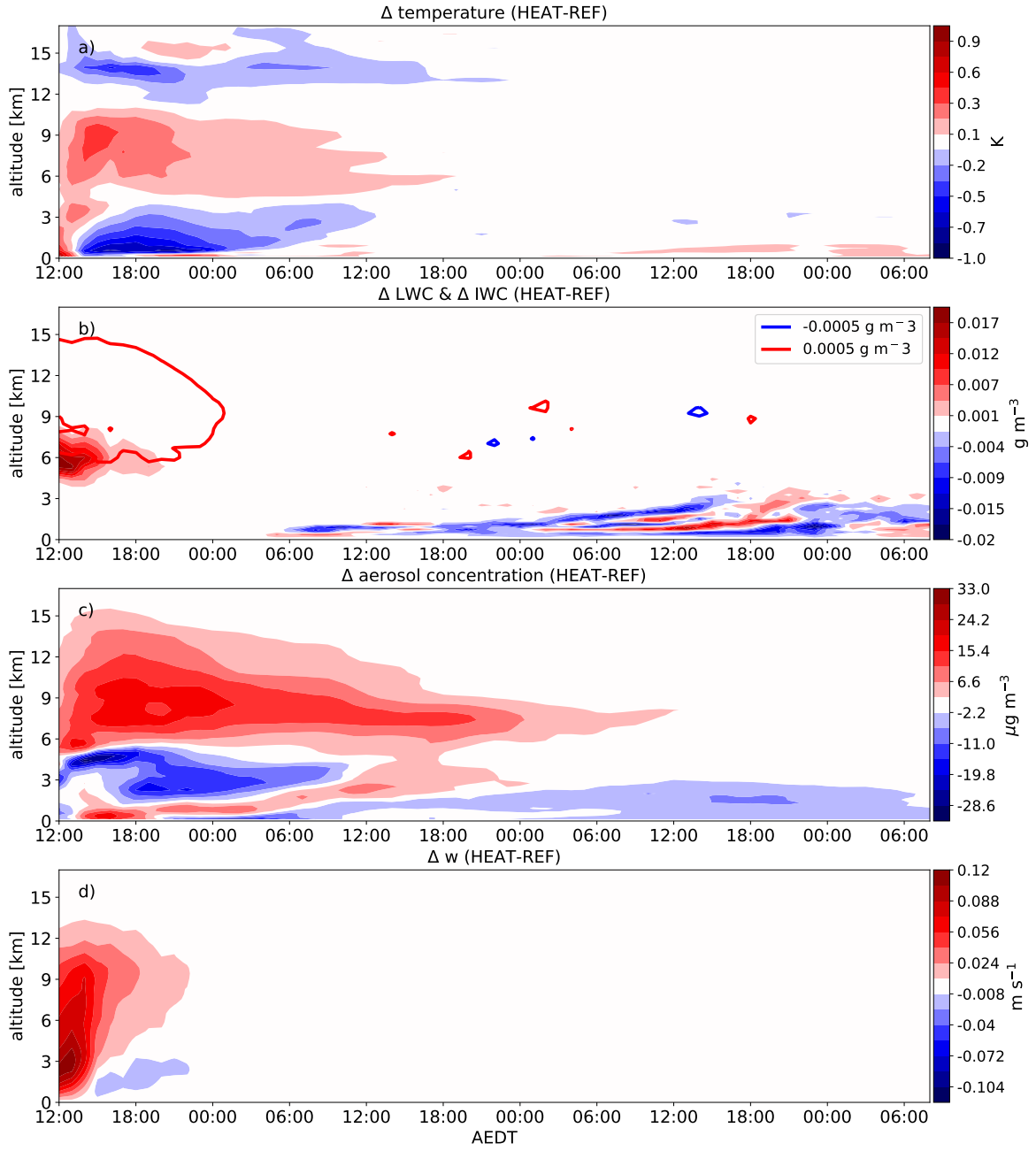

Figure 6.10.: Hovmöller diagram, averaged in plume area (grid cells that exceed an aerosol column of 0.05 g m^{-1}) for the difference (HEAT-REF) in a) temperature, b) LWC (filled contours) and IWC in (contour lines), c) aerosol concentration, and d) vertical wind velocity.

148.6°E and 36.3°S. Figure 6.11 d and h display the aerosol column for REF and HEAT towards the end of the simulation. In both cases the maximum concentrations are close to the fire source with 0.8 g m^{-2} and 1.0 g m^{-2} for HEAT and REF. Both plumes spread eastwards and south-eastwards reaching south New Zealand. But there is a clear difference in aerosol load north-west of New Zealand. High aerosol

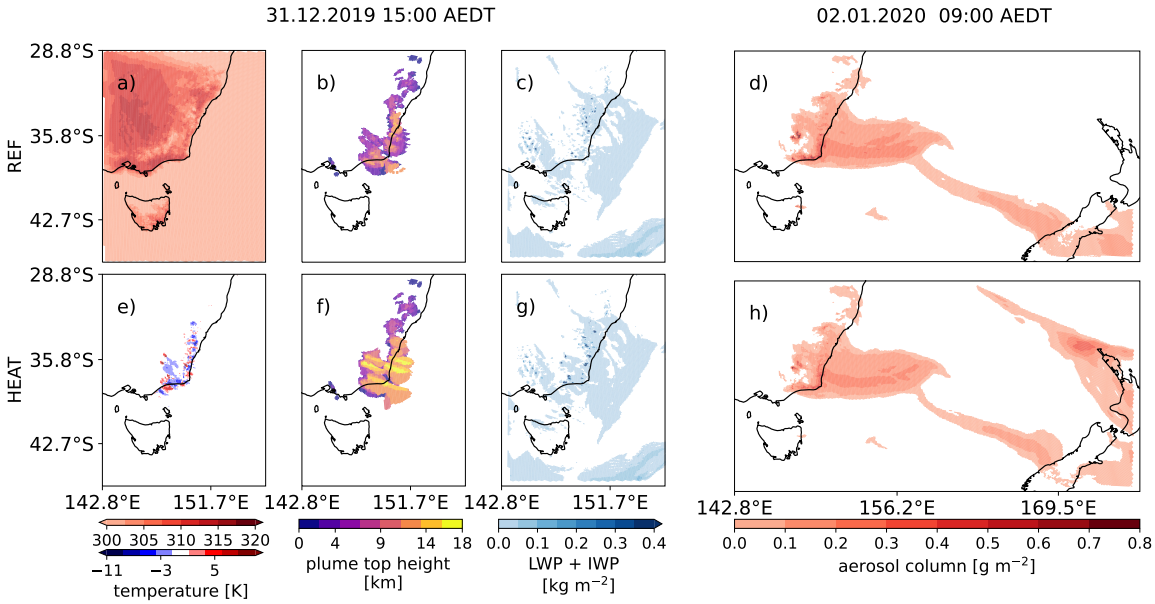

Figure 6.11.: The first row displays the REF experiment a) temperature at in the lowermost level, b) plume top height, and c) LWP+IWP on the 31.12.2019 at 15:00 AEDT, and d) the aerosol column on the 02.01.2020 at 09:00 AEDT. The second row shows e) the temperature difference (HEAT-REF), f) plume top height, g) LWP+IWP in the HEAT experiment on the 31st 15:00 AEDT, and h) the aerosol column on the 02.01.2020 at 09:00 AEDT.

loads are simulated in the HEAT experiment, but not simulated in REF.

Discussion

Figures 6.10 and 6.11 show the impacts of the implemented sensible heat release on the temperature and thereby the atmospheric stability, which leads to changes in cloud formation. It further increases the aerosol plume height and thereby impacts the transport. The shown effects on the temperature result from different processes. First, sh_{fire} increases the temperature above the fire areas. This creates a positive buoyancy and increases the vertical wind speed (in-plume mean by up to 0.11 m s^{-1}). The Hovmöller diagram for the in-plume vertical wind difference (HEAT-REF) shows strong updrafts at the beginning of the simulation, which in combination with sufficient ambient moisture increase the LWC and IWC, as outlined in figures 6.10 b and 6.11 g. Second, according to Grabowski and Morrison (2021) condensation of 1 g kg^{-1} water vapor mixing ratio corresponds to a change of 2.5 K air temperature and freezing of 1 g kg^{-1} cloud water mixing ratio to 0.3 K. In a coarse approximation the peak in-plume increase in LWC and IWC are 0.2 and 0.1 g m^{-3}, respectively. This corresponds to a warming of 0.075 K for condensation and 0.076 K for the freezing. The in-plume warming in the area of increased cloud formation is below 0.4 K, this indicates that latent heating makes about 37.5 % of the warming. Third, the pyro-convective clouds modify the radiative flux, by trapping terrestrial radiation and reducing the solar radiation that reaches the surface. This decreases the temperature above and below the clouds (displayed

in figure 6.10 a). Figure 6.11 d outlines the information lost in the Hovmöller diagrams due to the averaging. It further shows increases and decreases in the surface temperature by up to 10 K caused by the heat release on the one hand and the reduction of solar radiation on the other. Referring again to figure 6.4, the simulated and measured temperature show selective differences of up to ± 10 K. Some of these stations are close to the fires and could be impacted by either effect. Further, temperature increases near the surface in figure 6.10 a correspond to increased cloud formation. The changes in the LWC indicate a shift in cloud patterns. It appears that the LWC decreases during the night and increases during the day. This would match the diurnal cycle of the heat release, which peaks during the early afternoons. Further, the atmosphere is generally most unstable in the afternoons, which could favor convective cloud formation, which then stabilizes the atmosphere during the night. As discussed in section 6.3.2 the atmospheric stability strongly impacts the calculated injection height. Therefore, the increased plume heights in figure 6.10 c and 6.11 e do not solely result from the sh_{fire} induced buoyancy, but also from initially larger injection heights calculated by the plume-rise model. Thus, there are increased aerosol concentrations close to the surface at the beginning of the simulation. This can be explained by atmospheric stabilization due to increased cloud formation, similar to what is shown in section 6.3.2. This effect could exceed the increased buoyancy in areas with low FRP.

The impact of sh_{fire} within the plume is strongest during the first 12 h. There are again two reasons, the spreading and dilution of the plume over time and the strongest FRP during the first day of the simulation. Thus, these initial effects have a strong impact on the plume transport. This is outlined by the distribution of the aerosol load at the end of the simulation in figure 6.11 d and h. Further, it should be noted that cloud formation does not necessarily require additional moisture release by the fire but is also possible with strong buoyancy if the ambient atmospheric conditions are right.

It should be highlighted that the moisture and heat released by the fire impact the plume height in two ways. First, they impact the atmospheric state, which modifies the plume transport and second, this modified atmospheric state is used by the plume-rise model to calculate the injection height. It can be argued that moisture and heat released from the fire is already accounted for in the plume-rise model, but this still leads to an underestimation of the emission height (later shown in chapter 7). Further, this setup does not resolve convection, therefore it is consistent that the injection height is parameterized, as convection cannot be calculated explicitly. The experiments H2O and HEAT outline the impacts of moisture and heat release by the fire on the atmospheric state, including changes in temperature, cloud formation and winds. This fire-atmosphere interaction is not accounted for in the REF experiment.

6.3.4. Impact of aerosol-radiation interaction

Firstly, the results of the Mie calculations based on section 4.5.4 are shown in figure 6.12. For all modes the extinction is highest for the smallest wavelength bin (200-263.2 nm) and declines afterwards. The accumulation mode has maximums of $k_{ext} = 4.8$ m^2 g^{-2} in the insoluble mode and $k_{ext} = 5.7$ m^2 g^{-2} in the

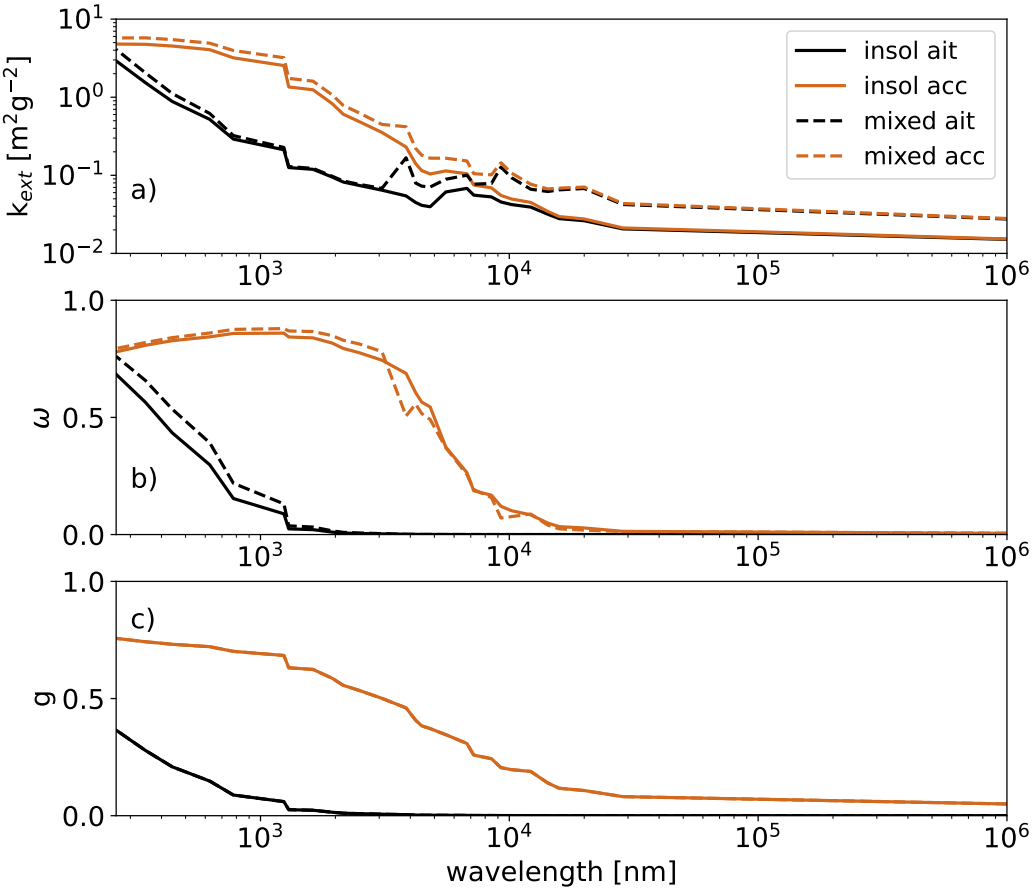

Figure 6.12.: Optical properties of soot containing modes at ecRad wavelengths. a) mass extinction k_{ext} in m^2 g^{-2}, b) single scattering albedo ω, and c) asymmetry parameter g unit-less. The black lines show the Aitken mode and the brown lines the accumulation mode. Solid and dashed lines show the insoluble and mixed mode, respectively.

mixed mode. The smaller Aitken mode peaks with $k_{ext} = 2.9$ m^2 g^{-2} in the insoluble and $k_{ext} = 4.1$ m^2 g^{-2} in the mixed mode. As discussed in section 2.2.4 the extinction can be approximated with a power law relationship of the negative Ångstrom parameter. The Ångstrom parameter usually decreases with size (Schuster et al., 2006). Khalizov et al. (2009) and Lefevre et al. (2018) show that for wavelengths (λ) between 200 nm and 1100 nm extinction enhances when soot particles are covered by a soluble shell. This is in agreement with the extinction coefficients calculated for this work. In Trentmann (2001) the extinction coefficient is approximately 5.8 m^2 g^{-2} for $\lambda = 200$ nm and decays to 0.15 at $\lambda = 4000$ nm assuming a number median diameter of 280 nm. Values from Trentmann (2001) are in good agreement with the extinction coefficient of the accumulation mode up to $\lambda = 1000$ nm, afterwards the values are between those of accumulation and Aitken mode. This is also the case for extinction coefficients collected by Reid et al. (2005a). The extinction in the short wave and near IR spectrum is up to two orders

of magnitude higher than in the IR spectrum, therefore, aerosol-radiation interaction dominates in the solar spectrum.

The single scattering albedo ω in the accumulation mode is between 0.8 and 0.9 for the insoluble and mixed mode in the short wave spectrum and then sharply declines in the near IR to 0.006 at $\lambda = 10^6$ nm. This implies that in the short wave most of the radiation is scattered and in the IR radiation is almost completely absorbed. In the Aitken mode ω declines from 0.684 to 0.003 in the insoluble and from 0.760 to 0.001 in the mixed mode within the short wave spectrum and declines to 0 in the IR for both compositions. This means that the Aitken mode absorbs radiation more efficiently than the accumulation mode. These values are in good agreement with Ohneiser et al. (2023) for organic and black carbon. Other studies discussed in Reid et al. (2005a) are in good agreement with the values of the accumulation mode as well.

The asymmetry parameter g is approximately the same for both compositions in the Aitken and accumulation mode, respectively. In the accumulation mode g declines from 0.76 to 0.45 within the short wave spectrum and further to 0.04 in the long wave. In the Aitken mode g declines from 0.36 to 0.00 within the short wave spectrum. Therefore, the scattering within the short wave spectrum is mostly forward, whereas in the long wave it is mostly symmetrical. Based on the aerosol-radiative properties, aerosol-radiation interactions are simulated. It is anticipated that these interactions predominantly influence the plume downstream. The absorptive nature of the aerosols is expected to induce local warming and lofting of the plume, which can semi-directly impact cloud formation.

Figure 6.13 shows the Hovmöller diagram created in the same way as figure 6.10. The top image displays the difference in temperature (ART-REF) within the plume. Between 3 and 11 km the temperature generally increases. The peak increase in temperature is 0.53 K. On the 31st of December from 6:00 to 18:00 AEDT, there is a further increase from the ground levels up to this layer. From the 1st of January at 09:00 AEDT till the end of the simulation the temperature increases between 1 and 3 km within the plume. Above and below this warming the temperature decreases. The maximum decrease is 1.0 K, close to the surface within the first 6 hours.

Figure 6.13 b displays the changes of LWC and IWC. During the first day of the simulation, there are no evident changes in LWC within the plume. In general, the changes in LWC are primarily below 3 km. The peak increase of 0.43 g m^{-2} (38.04 %) is reached during the day of the 31st of December. Followed by the maximum decrease of 0.46 g m^{-2} (38.32 %) during the night. Between 09:00 to 12:00 AEDT the following day the LWC slightly increases, followed again by a decrease over night. Towards the end of the simulation, the LWC increases when it becomes day again. For the IWC there are three distinguished areas of increase, all between 6 and 12 km altitude. The first lasts from 12:00 to 00:00 AEDT on the 30th of December, the second from 12:00 to 06:00 on the 31st of December and the last from 12:00 to 00:00 AEDT on 1st of January. The peak increase is 0.004 g m^{-3} and there are only small decreases by up to 0.001 g m^{-3}. Within these peaks the IWC increases by up to 26.0 % for the ARI experiment. The areas of decrease are at the beginning of the simulation, above and below the increased IWC. Figure

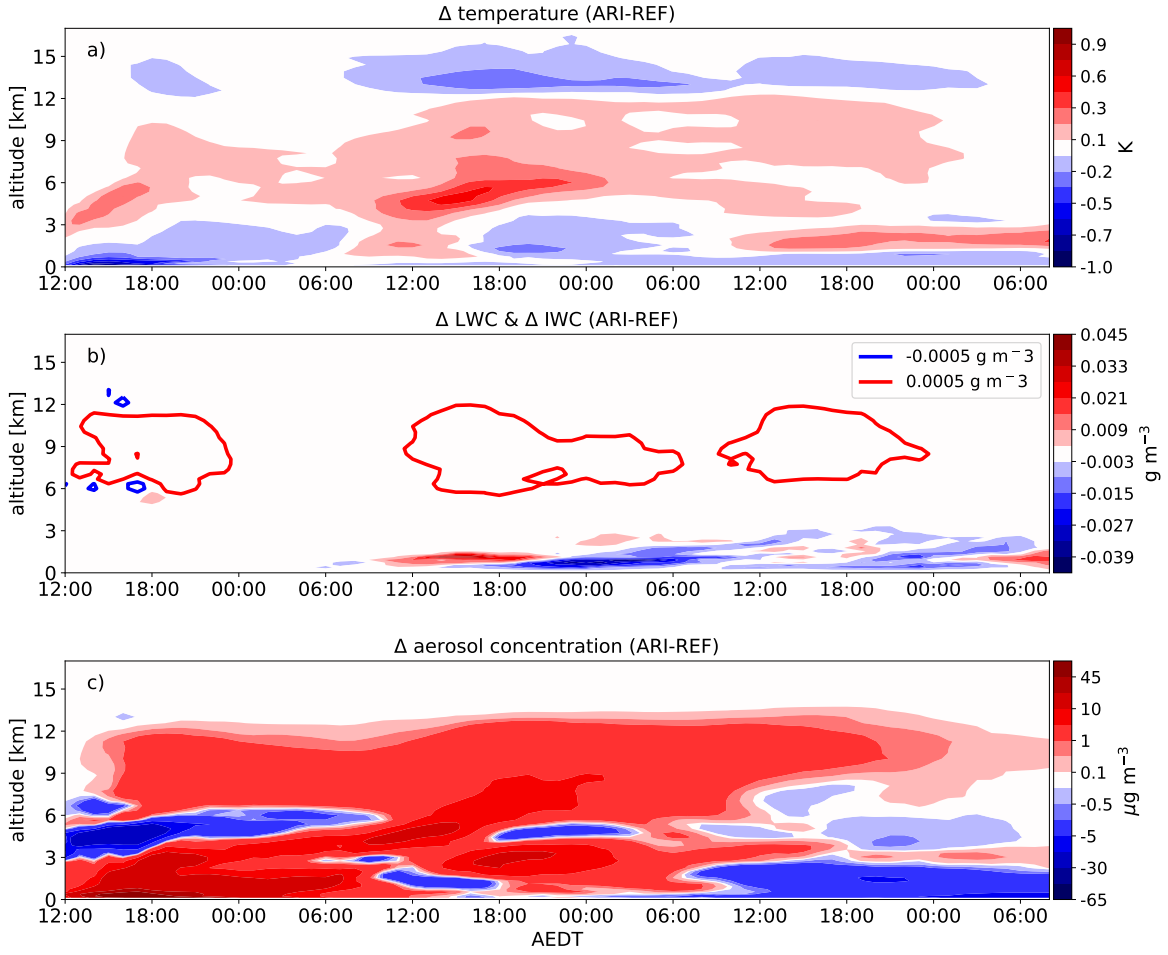

Figure 6.13.: Hovmöller diagram, averaged in plume area (grid cells that exceed an aerosol column of 0.05 g m^{-1}) for the difference (ARI-REF) in a) temperature, b) LWC (filled contours) and IWC in (contour lines) and c) aerosol concentration.

6.13 c displays the differences in the mean vertical profile of the aerosol concentration within the plume. Overall, the aerosol concentration is increased in the ARI experiment in comparison to REF. At the beginning of the simulation, the aerosol concentration increases in ARI by up to 63 μg m^{-3}. Throughout the simulation the aerosol concentration is increased above 7 km. The aerosol concentration decreases between 3 km and 5 km from the simulation start for 24 hours and from the surface up to 3 km from the 1st of January to 09:00 till the end of the simulation.

Figure 6.14 display the temperature difference at a given height (z) and the change in wind direction and speed with the arrows for ARI-REF. The last column shows the probability density functions of a certain vertical wind velocity in the plume for REF and ARI. Figure 6.14 a displays the level at approximately 300 m above the ground, where the maximum of mean the vertical profile of the aerosol concentration is reached. This is only 5 hours after the start of the simulation. The plume is still concentrated close to the

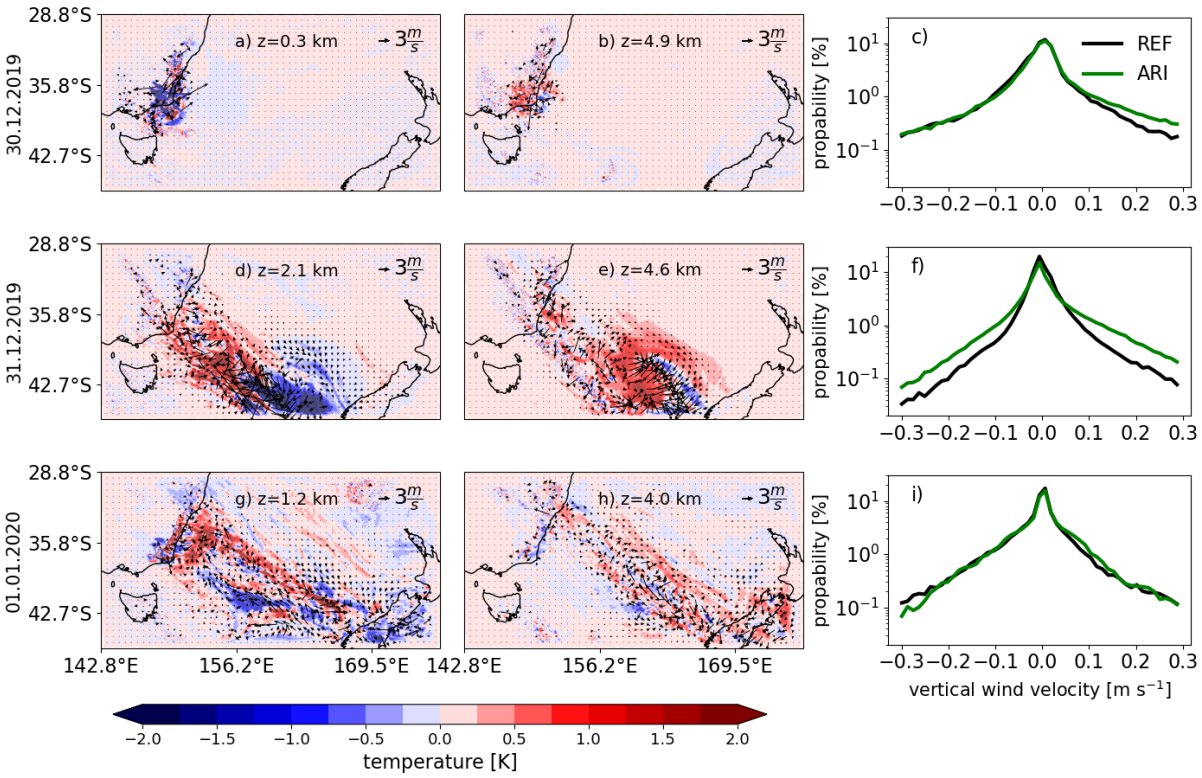

Figure 6.14.: Temperature difference (ARI-REF) and the change in wind direction and speed on the 30th December 16:00 AEDT at a) 0.3 km, b) 4.9 km, on the the 31st December 16:00 AEDT at d) 2.1 km, e) 4.6 km, and on 1st January 16:00 AEDT at g) 1.2 km, and h) 4.0 km. The last column shows histograms of the probability of a certain vertical wind velocity in the according experiment, REF in black, ARI in green, c) on the 30th December 16:00 AEDT, f) the 31st December 16:00 AEDT, and i) 1st January 16:00 AEDT on the bottom.

fires along the coast. There is some noise but overall, the temperature is decreased. The mean decrease within the plume is -0.72 K. The maximum decrease is -12.1 K, but there are also local increases by up to 8.67 K. The wind direction and speed change along with the temperature decrease. The horizontal wind speed changes by up to 17.3 m s^{-1}. Figure 6.14 b displays the same time step but at a height of 4.9 km. This level is at a local maximum of the mean vertical profile of the aerosol concentration. The temperature difference (ARI-REF) here is mainly positive. The in-plume mean increase is 0.30 K. There is again some noise, with maximum increases of 3.4 K and decreases by up to 2.1 K. The wind speeds change by up to 10.4 m s^{-1}. The probability density function in figure 6.14 c shows that for the ARI experiment the probability of downdrafts remains the same but probability of updrafts increases in the plume. Figure 6.14 d displays the altitude of 2.1 km. This is 800 m above the maximum aerosol concentrations. One day and 5 hours are simulated and the plume spreads south-eastwards. There are two distinctive

signals in the temperature difference, one area of increase closer to the Australian coast with a maximum increase of 4.4 K and an area of temperature decrease further south-east, with a maximum decrease of 5.7 K. The wind speed changes by up to 18.2 m s^{-1}. In terms of wind direction, it appears that there is an inflow towards the area of temperature decrease. Figure 6.14 e displays the altitude of 4.6 km, at a local peak of the mean vertical profile of the aerosol concentration. The temperature increases in most parts of the domain, with maxima of up to 2.6 K. The wind speeds increase by up to 11.3 m s^{-1}. The changes in wind direction appear to flow out of the area of temperature increase. The probability density function of in-plume vertical velocity shows that in the ARI experiment the probability of higher up- and downdrafts is increased. The increase is stronger for the updrafts. Figure 6.14 g displays the height of 1.2 km that is the height of the maximum of the mean vertical profile of the aerosol concentration. The temperature difference is noisy with increases east of the Australian coast by up to 5.7 K and decreases over New Zealand by up to 4.2 K. The in-plume mean temperature decreases by 0.1 K. The wind speed changes by up to 9.0 m s^{-1}. The changes in wind directions are noisy but there is some convergence slightly west of New Zealand. Figure 6.14 h displays the temperature difference at another local maximum of mean vertical profile of the aerosol concentration. The temperature mainly increases with maximum increases of 4.3 K. The in-plume mean increase of 0.3 K. There are some areas of decrease especially over the Australian coast with up to 2.4 K. The wind speeds change by up to 9.6 m s^{-1}, with no systematic changes in the wind direction. The probability density function in figure 6.14 i shows that for the ARI experiment the probability of downdrafts between -0.3 and -0.2 m s^{-1} are decreased in the plume and updrafts especially in the range of 0.5 to 1.5 m s^{-1} are increased.

Figure 6.15 displays the temporal evolution of the 2m-temperature and short wave (SW) net flux at the surface. The three rows display different locations, where temperature measurements of AWS are available. The locations of the AWS are displayed in figure 6.1 with the magenta triangles. Figure 6.15 a shows a similar temperature profile for REF and ARI. This profile agrees with the top temperatures measured during the day and the minimum temperatures during the night are captured well. The maximum temperature of the third day is overestimated in both simulations, in REF by 8.1 K and in ARI by 7.1 K. The aerosol column peaks in the afternoon of the 31st of December with a maximum value of 2.0 g m^{-2}, declines around midnight, and remains around 0.25 g m^{-2} afterwards. Figure 6.15 b shows the corresponding SW net flux at the surface and the sum of LWP and IWP. During the first day the SW net flux declines quickly in ARI compared to REF, which leads to a maximum decrease of 609.3 W m^{-2}. During the second day the SW flux is reduced in both experiments. On this day there are clouds present. On the third day the SW flux in the ARI experiment is clearly reduced by up to 478.1 W m^{-2}. In figure 6.15 c the initial temperature in both simulations is overestimated by 5.0 K. With the increase of aerosol column, the temperature in ARI declines compared to REF by almost 1 K. The temperature on the second day is overestimated by both simulations, in ARI by 6.9 K and in REF by 7.9 K. During the third day the differences between ARI and REF are largest. The temperature is reduced by 7.4 K in the ARI experiment. The aerosol column is largest on the first day with 1.1 g m^{-2} and between 0.25 and 0.55 g

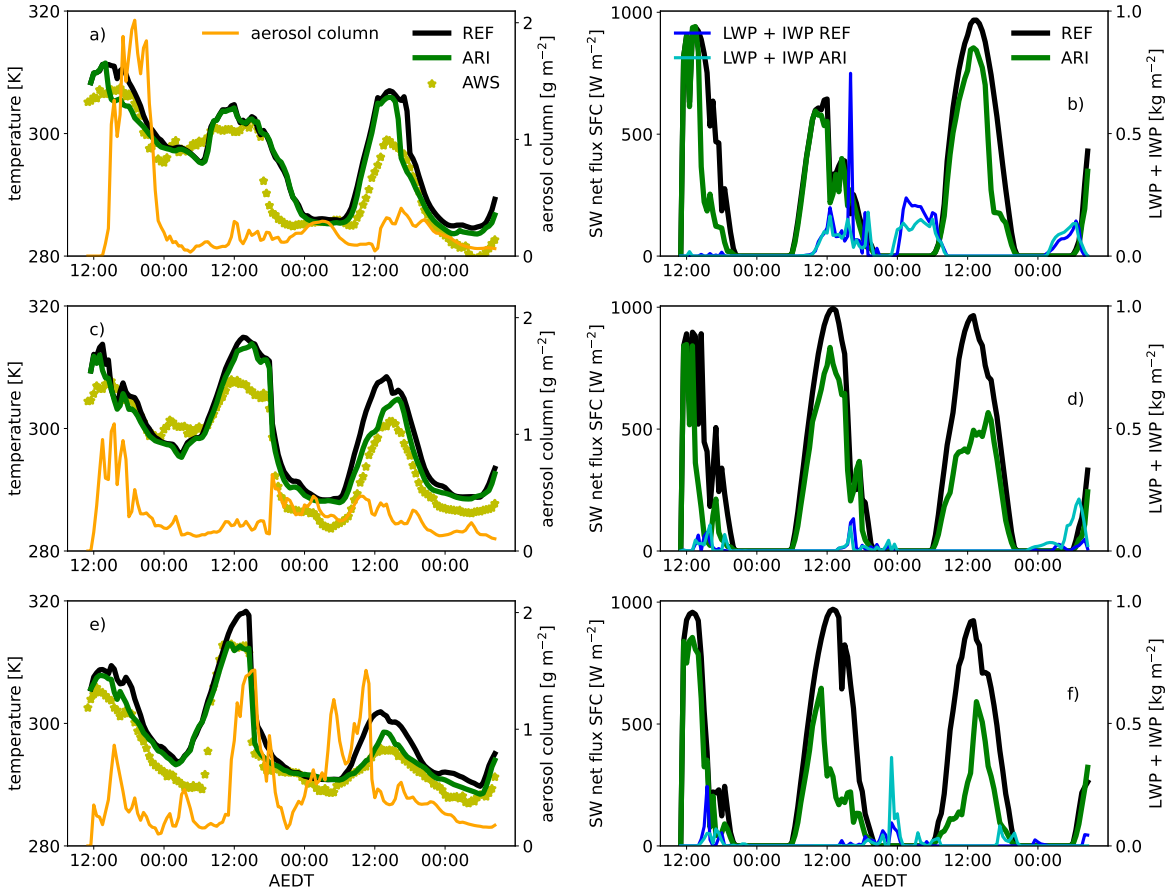

Figure 6.15.: Temporal evolution of the 2m-temperature (REF in black, ARI in green), aerosol column in ARI in orange in the first column and in the second column sum of LWP and IWP (REF in blue, ARI in turquoise) and short wave net flux at the surface (REF in black, ARI in green), for three different locations a) and b) at 148.9725°E, 36.2939°S, c) and d) at 150.2670°E, 34.3335°S, and e) and f) at 150.4217°E, 34.5253°S), marked in figure 6.1 with the magenta triangles. The green stars show the AWS data.

m^{-2} the rest of the simulation. Figure 6.15 d shows that the ARI experiment reduces the SW net flux at the surface at all three days by up to 715.3 W m^{-2}, 258.5 W m^{-2} and 530.2 W m^{-2}, respectively. The sum of LWP and IWP reach to up to 0.15 kg m^{-2} in the afternoons of the first two days. The peak decreases in SW flux are simulated while LWP and IWP are below 0.05 g m^{-2}. At the third location 6.15 e the 2m-temperature in ARI fits the measurements well. On the second day the maximum temperature of the AWS measurement is 312.9 K and the simulated temperatures are 313.1 K and 318.3 K for ARI and REF. The temperature during the night fits well in both cases. During the third day the ARI experiment overestimates the peak temperature by 2.7 K and the REF experiment by 5.0 K. The aerosol concentration has three peaks, with a maximum concentration of 1.51 g m^{-2} on the second day. The SW net flux at the surface in figure 6.15 f is reduced in the ARI experiment at all three days by up to 592.2 W m^{-2}, 760.9 W m^{-2} and 714.0 W m^{-2}, respectively. The LWP and IWP reach a maximum of 0.37 kg m^{-2} during the second night. Clouds are simulated on all days in the afternoon.

Last, it is analyzed how strong the aerosol-radiative forcing changes at top of the atmosphere (TOA).

Therefore, figure 6.16 a and c display the difference in short wave net flux at the top of the atmosphere (ARI-REF) at 13:00 AEDT on the 31st of December and the 1st of January. In figure 6.16 a there are large areas of noise. The maximum decrease in SW net flux is up 594.9 W m^{-2} and the maximum increase is 491.1 W m^{-2}. These maximum values are part of the noise, but there are three systematical changes detectable. One area of decrease spreads south-eastwards from the coast, another area of decrease is in the southern center of the domain and south-west to this is a clear signal of increase. Figure 6.16 b displays the aerosol column as well as the 0.005 kg m^{-2} isoline of the sum of LWP and IWP of the REF and ARI experiment. The aerosol plume spreads south-eastwards, the area of the plume there is also cloud band. There is another cloud (ice) band spreading north to south along 165°E. The LWP+IWP is similar in REF and ARI except for clouds simulated in ARI the southern center of the domain, which are not simulated in REF. Analog to plot 6.16 a, figure 6.16 c shows the differences in SW net flux TOA for the 1st of January 13:00 AEDT. There is a lot of noise in the areas of the clouds. Beside the noise the SW net flux mostly increases, with selective decreases in the plume area. Figure 6.16 e outlines that clear sky and plume areas are limited to the Australian coast and south-east of New Zealand. In these areas the SW net flux mostly decreases.

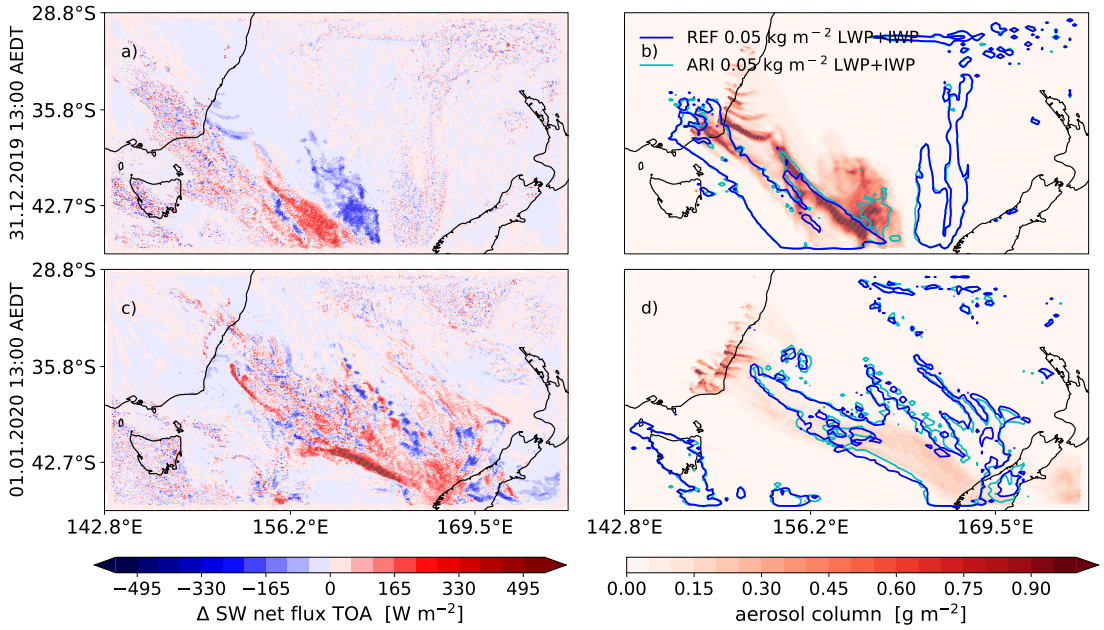

Figure 6.16.: a) and c) difference in short wave net flux at the top of the atmosphere (ARI-REF) b) and d), aerosol column (filled contour) and the sum of LWP and IWP (REF in blue and ARI in turquoise) at 13:00 AEDT on the 31st of December top row and the 1st of January bottom row.

Discussion

The ARI experiment includes aerosol-radiation interaction, this can impact the radiative fluxes directly and semi-directly through cloud formation. The experiment does not include the indirect aerosol-radiation effect and therefore, the impact of aerosols on the cloud microphysics. The direct aerosol effect is outlined in figure 6.15 and 6.16, both show that aerosol-radiation interaction impacts the radiative fluxes. The scattering and absorption of solar radiation by the aerosols reduces the SW net flux at the surface, as shown in figure 6.15 b, d and e. The SW net flux TOA depends on the underlying albedo. The areas of decreased SW net flux in figure 6.16 a and c can be connected to the plume in clear-sky conditions. The scattering by the aerosol increases the SW flux back to the TOA. This is especially the case over the ocean. Ocean water has low albedos down to 0.04 (Feng et al., 2015). This means the ocean absorbs solar radiation efficiently. The dependence on the underlying albedo on the SW net flux is outlined by high aerosol concentrations in clear sky conditions over Australia, which hardly decrease and even increase selectively. The latter is the case when the aerosol layer scatters less radiation than the surface reflects. Note, that the smaller Aitken mode particles absorb SW radiation more efficiently. The concentration of Aitken mode particles is largest close to the emission source as they grow within hours (figure 4.4) and are shifted to the larger accumulation mode. Further, figure 6.16 shows that the areas of increased SW net flux TOA are placed in areas with overlapped plume and clouds. Clouds generally have high albedos with up to 0.7 (Kondratyev, 1969), depending on the wavelength and optical thickness of the cloud. If the aerosol layer is placed above clouds the reflected radiation is reduced. This is seen as an increase in SW net flux at the top of the atmosphere. It is noteworthy that changes in cloud cover also impact the SW net flux. This is outlined by figure 6.16 d in the southern center of the domain. There are clouds simulated in the ARI experiment, which are not simulated in REF. The effect of the radiative feedback of these clouds is hard to determine as it overlaps with the plume. The dependency of the aerosol forcing on the underlying albedo is reported in literature as well. As shown by Chang et al. (2021), Heinold et al. (2022), and Sellitto et al. (2022), who report different forcing effects for clear sky and all sky conditions for the Black Summer Fires. Statistical analysis and correlations between the changes in radiative fluxes, aerosol plume and cloud feedback are hard to calculate due to the strong noise. The noise is dominant in cloud areas and created by small disturbances in cloud patterns.

The impact of aerosol-radiation interaction on the atmospheric stability and therefore cloud formation is referred to as the semi-direct aerosol effect. The impact on temperature is shown in the figures 6.13 a, 6.14 and 6.15. Figure 6.15 shows that there is an impact of aerosol-radiation interaction on the 2m-temperature. This effect is again strongest in clear sky conditions because more radiation reaches the surface. The ARI experiment is an improvement in the representation of the 2m-temperature compared to the three AWS, especially in figure 6.15 e. The simulated temperature in REF is generally overestimated. The comparison with the AWS has some challenges. The evident changes of over 7 K in the 2m-temperature due to aerosol-radiation interaction strongly depends on the aerosol concentration.

Comparing individual points is challenging because minor deviations between the simulated and actual plume can result in significant discrepancies. Additionally, the aerosol emission flux and height, which are crucial for plume transport, are subject to considerable uncertainties. Consequently, deviations from the actual plume are unavoidable. It is noteworthy that at all three locations, the aerosol concentration increases during the initial hours, suggesting that the temperature in the grid cells is likely already influenced by an aerosol plume at the start of the simulation. Additionally, there is an overestimation of both the initial and measured temperatures, which may be attributed to the initial meteorological conditions that do not account for the radiative effects of biomass burning aerosols.
The temperature in the ARI experiment is reduced by up to 7 K, this is again in the same order of magnitude as the discrepancies of single AWS measurements and the simulated temperature in REF, displayed in figure 6.4. Measurements close to the fire could therefore not only be impacted by the heat release of the fire and the reduction of solar radiation by clouds as discussed in section 6.3.3, but also by the direct aerosol effect.
Figure 6.14 outlines the complexity of the temperature changes caused by aerosol-radiation interaction. It appears that due to aerosol-radiation interaction the top of the plume heats during the day, while the layers below cool. This can be explained with the scattering and absorption of solar radiation by the uppermost aerosols, and the dimming below. This effect is most obvious at the beginning of the simulation while the plume is more concentrated and denser. It gets more complex, as the plume develops. The plume has a three-dimensional structure as shown in figure 6.6. The plume top rises as it spreads further south-east, but the aerosol concentrations below remain high. In figure 6.14 d, the concentrations are high in the whole area of the temperature changes, but there is a warming effect closer to the Australian coast and a cooling effect closer to New Zealand. This is due to the elevation and the overlaying aerosols closer to New Zealand. It is noteworthy that these strong temperature differences are not represented in the Hovmöller diagram in figure 6.13, due to the averaging. Figure 6.14 could indicate a systematic change in wind direction during the first two days, which shows an inflow at the bottom of the plume, an updraft in the plume, and an outflow at the top of the plume. This is not detectable on the last day of the simulation. On the third day the horizontal wind changes appear mostly noisy. However, it is evident that the aerosol-radiative effects impact the temperature and wind fields within and close to the plume and a lofting of the plume is induced.
The averaging in the Hovmöller diagram figure 6.13 indicates that temperature wise there in a stabilization below 3 km within the plume, as the temperature increases above and decreases below, except for the 31st of December. The stabilization of the lower atmosphere at the beginning of simulation results in smaller injection heights from the plume-rise model for the ARI simulation. Nevertheless, over time the aerosol masses loft themselves in the ARI simulation as shown in the Hovmöller diagram in figure 6.13 c. The can be explained by the temperature increase at the plume top, which creates buoyancy and causes the warmed layers to ascend. Further, the total aerosol mass is increased in ARI. The self-lofting of the plume counteracts the deposition. The stabilization of the atmosphere during the night reduces

liquid cloud formation (strato-cumulus) below 4 km. The destabilization on the 31st of December results in the biggest in-plume increase in LWC and IWP. It is noteworthy that aerosol-radiative effects increase cloud formation during the day, the temperature increase in the plume is therefore not solely caused by the aerosol-radiative effects but also include the latent heat release as well as the cloud radiative effects. The in-plume differences in the Hovmöller diagram in figure 6.13 remain in the same order of magnitude. This indicates that although the plume spreads and dilutes the aerosol-radiative effect impacts the whole plume.

6.3.5. Impact of moisture and heat release by the fire and aerosol-radiation interaction

This section analyzes the effect of the three implementations: moisture release, sensible heat release and aerosol-radiation interaction combined in the ALL experiment and compares the five experiments all

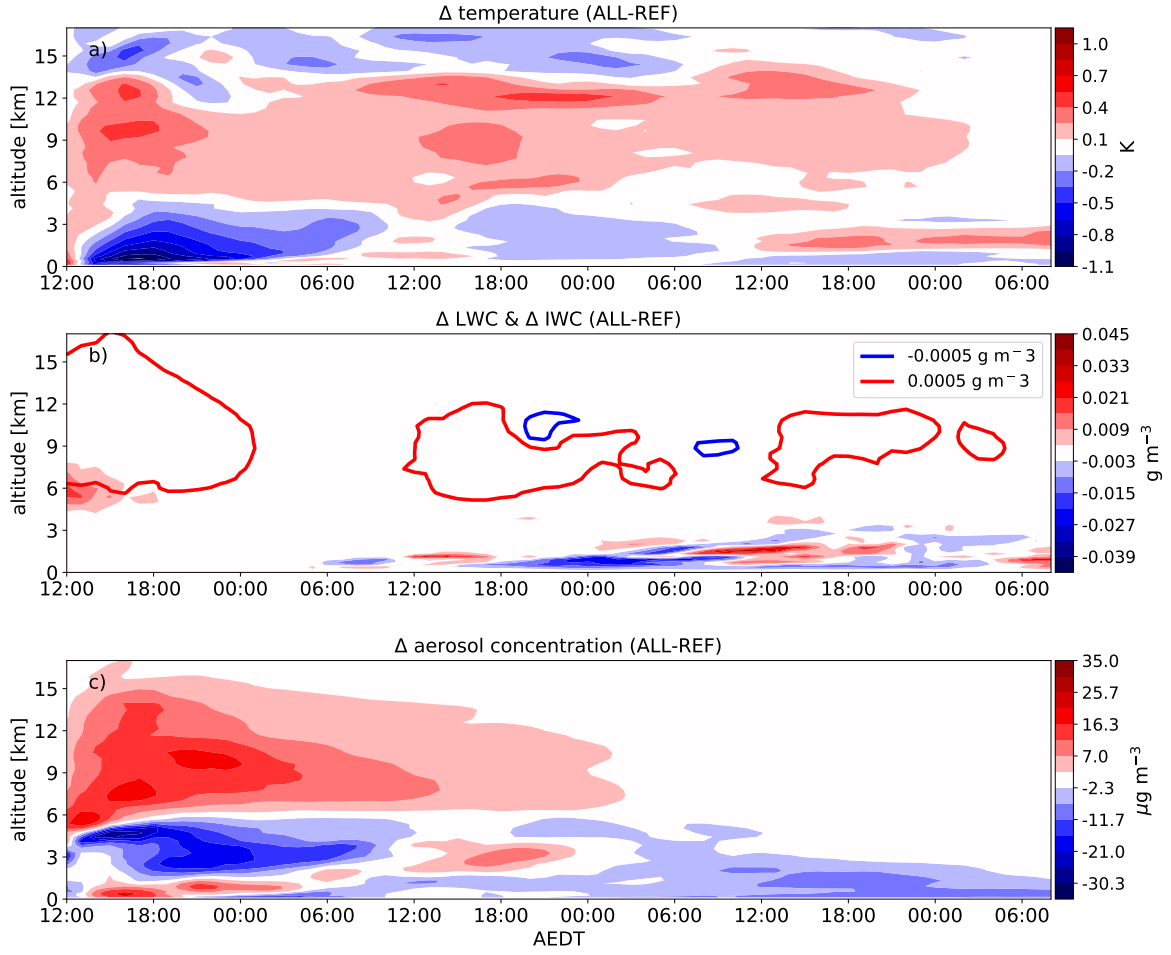

Figure 6.17.: Hovmöller diagram, averaged in plume area (grid cells that exceed an aerosol column of 0.05 g m^{-1}) for the difference (ALL-REF) in a) temperature, b) LWC (filled contours) and IWC in (contour lines) and c) aerosol concentration.

together. Firstly, figure 6.17 shows a Hovmöller diagram analog to figure 6.10. The top figure displays the temperature difference of ALL-REF within the plume. The temperature in the plume rises between 3 and 12 km during almost the whole simulation. During the first simulation hour the temperature is increased continuously from the ground up to 12 km. During the day of the 31st of December, the near surface temperature increases as well. From 12:00 AEDT onward to the 1st of January the temperature increases between 1 km and 3 km as well. The maximum in-plume mean increase is 0.66 K. Above 12 km the temperature generally decreases. The largest decrease of up to 1.1 K is in the late afternoon of the 30th of December close to the surface. The near surface temperature further decreases during the night on the 31st of December. Figure 6.17 b displays the differences in in-plume mean LWC and IWC. There is an increase in LWC between 5 km and 8 km and in IWC between 6.5 and 17 km during the first 12 hours. Differences in LWC remain below 5 km throughout the rest of the simulation. The LWC seems to increase during the day, with a maximum increase of 0.04 g m^{-3} on the 1st of January around 12:00 AEDT. Further, the LWC decreases during the day. The largest decrease is 0.03 g m^{-3} around 00:00 AEDT on the 1st of January. The IWC increases on the 31st of December and the 1st of January. The maximum increase in IWC is at the beginning of the simulation with 0.024 g m^{-3}. The decreases are smaller with a maximum decrease of 0.001 g m^{-3} around 21:00 AEDT on the 31st of December. The bottom Hovmöller diagram displays the in-plume mean differences of the aerosol concentration. There is a dominant increase from the start of the simulation onward above 5km. The effect is strongest (+19.9 g m^{-3}) within the first 12 hours. Below 5 km the aerosol concentration mainly decreases, with a maximum decrease of 31.5 g m^{-3} within the first 6 hours around an altitude of 5 km. There is a near surface increase in the afternoon of the 30th of December.

Figure 6.18 a displays the plume top height. The plume top height is defined as the highest level that reaches an aerosol optical depth above 0.005 at the wavelength of 550 nm. In the REF experiment, it reaches an altitude of 13.9 km after 3 hours and declines afterwards to 10.8 km at the end of the simulation. The top height in the H2O experiment increases from 12.6 km to 14.9 km during the first 5 hours and declines to 11.2 km at the end of the simulation. In the HEAT experiment, the initial plume top height is already at 15.9 km and increases to a maximum of 18.0 km after 7 hours. The plume top height slightly decreases till a rapid decline to 13.5 km at 1st of January 02:00 AEDT. The ARI experiment starts with a plume top height of 11.2 km and reaches the same altitude as REF but 2 hours later and remains around this height till the end of the simulation. The ALL experiment starts with a plume top height of 15.9 km, the same as the HEAT experiment and reaches 20.0 km after 8 hours. The maximum top height of 20.8 km is reached on the 31st of December at 21:00 AEDT. All experiments show sudden in- and decreases in the order of 500 m. 500 m corresponds to the level thickness at these altitudes. The bottom figure 6.18 displays the plume mass weighted height for the different experiments. Here, the plume is defined as every grid cell that exceeds an aerosol mass mixing ratio of 0.05 μg kg^{-1}. The mass weighted height in REF is 2.9 km at the beginning of the simulation and reaches a maximum of 3.8 km after 4 hours and a minimum of 1.7 km at the end of the simulation. The mass weighted height of the

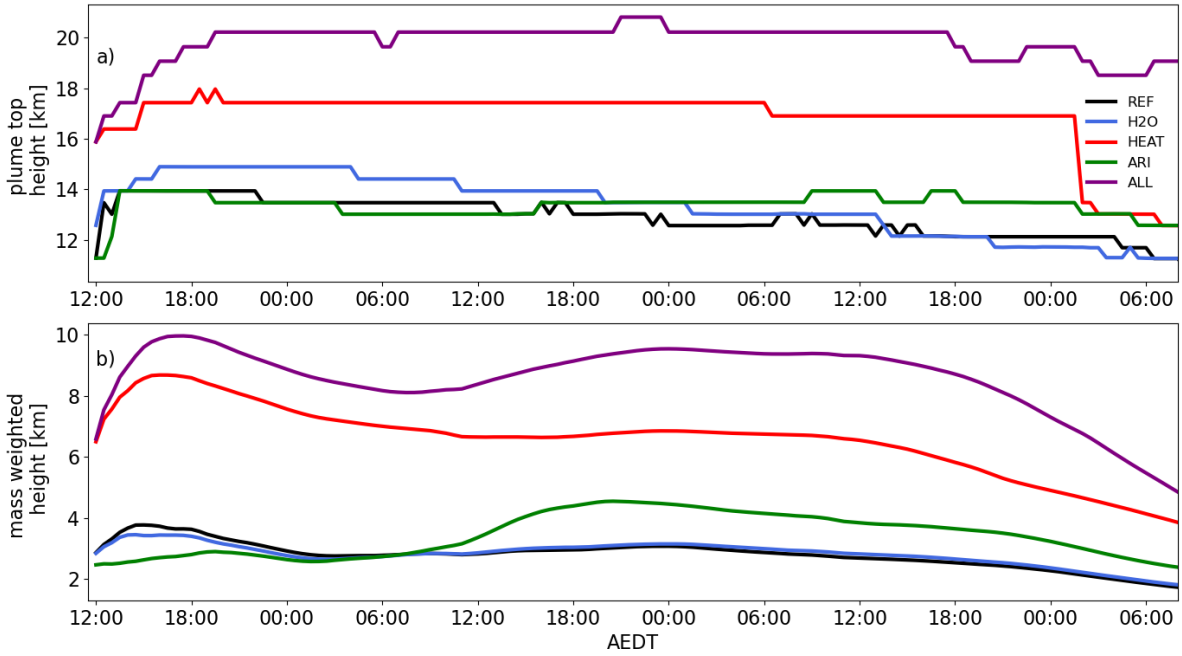

Figure 6.18.: Temporal evolution of a) the plume top height, defined as the highest level that reaches an aerosol optical depth above 0.005 at the wavelength of 550nm and b) mass weighted height of the plume. Here, the plume is defined as every grid cell that exceeds an aerosol mass mixing ratio of 0.05 μg kg^{-1}. REF is in black, H2O in blue, HEAT in red, ARI in green, and ALL in purple.

H2O experiment starts at 2.8 km and increases to a maximum of 3.4 km after 3.5 hours. The plume is also lowest at the end of the simulation with 1.8 km. In the HEAT experiment, the mass weighted height starts higher at 6.5 km and peaks with 8.7 km after 5 hours. This experiment shows a clear decrease throughout the simulation with a minimum of 3.8 km at the end of the simulation. In the ARI experiment the mass weighted height starts lowest at 2.5 km. Reaching a small peak of 2.9 km after 9.5 h. The maximum height is reached on the 31st of December at 22:00 AEDT. The plume is lowest at the end of the simulation with a height of 2.4 km. The highest mass weighted height in the ALL experiment starts at 6.6 km and peaks after 7.5 hours with 10.0 km, before declining and reaching 9.5 km again around 00:00 AEDT on the 1st of January. After 18:00 AEDT the plume decreases to 4.7 km.

Discussion

The ALL experiment includes moisture and heat release as well as aerosol-radiation interaction and therefore combines different processes. The heat release increases the near surface temperature, creating buoyancy and convective clouds, as discussed for the HEAT experiment. Additionally, WVC increases due to emission of qv_{fire}, this is likely to further drive cloud formation. The aerosol-radiative effect at the beginning of the simulation is presumably smaller than in ARI, as the additional cloud formation overlaps with the aerosol plume. The Hovmöller diagrams on the first day is similar to those in the HEAT analysis. Later on it shows similar features to the ARI experiment. The effect of H2O is small

in comparison. Therefore, sh_{fire} and qv_{fire} emission affect the early stage of the plume and the aerosol-radiative effects become dominant as the plume evolves. The temperature decreases above and below the plume throughout the simulation. This is caused by the aerosol- and cloud-radiative effects that trap terrestrial radiation and dim the solar radiation. This effect stabilizes the atmosphere below the plume and can lead to reduced injection heights in areas of low FRP, as discussed in section 6.3.3.
Figure 6.18 displays the plume top and mass weighted height and shows increases in both during the first 6 hours (except for the mass weighted height in the ARI experiment). Further, there is a general decrease in plume heights for all experiments not considering aerosol-radiation interaction after the first 12 hours. There are three explanations for the sinking of the plumes. First, the atmosphere is most unstable during the day of the 30th of December. Therefore, the plume-rise model returns the largest injection heights on this day. Second figure 6.2 outlines that the FRP and therefore the emissions, as well as the implemented effects of sensible heat and moisture release are largest on the 30th of December. The ARI effect is also strongest for high aerosol concentrations. Parts of the plume are transported out of the domain within 24 hours, therefore the plume height reduces over time. The lofting of the plume, especially for the HEAT, ALL, and ARI experiment transports aerosols to levels with higher wind speeds, which transport the elevated aerosols out of the domain even faster. This explains the steep decline in plume top height in the HEAT experiment towards the end of the simulation. Further, the mass weighted height of all the simulations decreases during the last 15 hours. This decrease is stronger for elevated plumes. The plume heights in ALL and HEAT show the largest decrease, and have the largest elevation. It should be noted that all experiments impact the parameterized emission height through the changes in the atmospheric variables. For H2O and ARI the emission height is reduced due to a stabilization of the atmosphere. But overall, the REF and H2O experiment are very close in plume top and mass weighted height. The aerosol-radiation interacting in ALL and ARI displays a slight lofting and sinking with the diurnal cycle for the first two days. The lofting due to aerosol-radiative effects appears to be stronger in the ALL experiment. The initial lofting due to sensible and latent heat release transports more aerosols above clouds, which increases the aerosol-radiative effect. This is in quantitative agreement with Ohneiser et al. (2023), who find increasing lofting rates with height, by up to several kilometers a day depending also on the AOD of the aerosol layer. A qualitative comparison is difficult as parts of the elevated plume are transported out of the domain within a day.

7. Comparison to observations

7.1. Observational data

In this chapter the experiments are compared to observations. First, the simulated aerosol optical depth (AOD) is compared to the MAIAC AOD. Then, height retrievals performed with the NASA 3D wind retrieval algorithm are compared to the plume and cloud top heights in the experiments. Next, the modeled biomass burning aerosol backscatter is compared to the attenuated backscatter of CALIPSO and finally an analysis of the radiative fluxes in comparison with CERES data is done.

MAIAC stands for Multi-Angle Implementation of Atmospheric Correction and is described in detail in Lyapustin et al. (2011a,b, 2012, 2018). MAIAC is based on MODIS L1B data, which contains calibrated and geolocated at-aperture radiances for 36 bands between the wavelengths of 0.4 µm to 14.4 µm. The special resolution is 1 km in the nadir, degrading to 4.8 km in the scan along direction. MAIAC is an advanced algorithm, which uses time series analysis in combination with a pixel- and image-based processing to receive a better accuracy of cloud detection, aerosol retrievals, and atmospheric correction. The time series analysis characterizes the surface background. The MODIS L1B data is gridded on a fixed 1 km resolution grid, following the area-weighted method by Wolfe et al. (1998). This returns observations of the same grid cell over time, comparable to geostationary satellite observations. Further, data is stored in achieve memory for 4 days at the poles and 16 days at the equator to help retrieve the surface bidirectional reflectance distribution function (BRDF) from an accumulated set of multi-angle observations. This enables the detection of seasonal and rapid surface changes. The MAIAC data used in this work is downloaded from: `https://search.earthdata.nasa.gov/search/granules?p=C2324689816-LPCLOUD&pg[0][v]=f&pg[0][gsk]=-start_date&q=maiac&tl=1702297807.628!3!!` (Lyapustin, 2023).

The NASA 3D wind retrieval algorithm is based on stereo imaging and developed by Carr et al. (2018, 2019, 2020). Stereo imaging uses geometric parallax for the feature height retrieval. The fusion of geostationary (GEO) and low-earth orbit (LEO) satellites produces high quality three-dimensional (3D) atmospheric motion vectors (AMV) with a multi-platform, multi-angle stereoscopic technique. The term "3D Winds" primarily signifies the positioning of horizontal AMVs three-dimensionally in the atmosphere. Observation of the parallax of a feature when observed from two different vantage points (or stereo) provides direct information about its height. This method is independent of atmospheric models and thermal structures compared to other AMV retrievals. Further, the stereo technique has advantages over the passive thermal IR approach in determining a feature's height, as it avoids the thermal infrared

(IR) techniques for height assignments, which are subject to large uncertainties. For this study the LEO-GEO retrieval is used. The LEO satellite data used is the Terra and Aqua MODIS Level 1B data in the blue band (459-479 nm) with 500 m resolution. For the GEO satellite the blue band data (430-480 nm) from Himawari-8 is used. The Advanced Himawari Imager (AHI) is a geostationary weather satellite operated by the Japan Meteorological Agency with 16 channels and a resolution of 0.5-2 km depending on the channel (1 km resolution for blue band channel). AHI has a temporal resolution of 10 min, which is used to determine the movement of the feature. The MODIS data is then used to calculate the parallax and get the AMVs and height. The MODIS data is downloaded from `https://ladsweb.modaps.eosdis.nasa.gov/search/order/1/MODIS` (MODIS Characterization Support Team, 2017) and the AHI data from `https://noaa-himawari8.s3.amazonaws.com/index.html` (noaa-himawari8, 2024). Access to the code was granted to me by Dr. Jim Carr (jcarr@carrastro.com).
The CALIPSO (Cloud-Aerosol Lidar and Infrared Pathfinder Satellite Observation) satellite combines an active lidar instrument with passive infrared and visible images to analyze the vertical structure of thin clouds and aerosol layers globally. CALIPSO was launched with the cloud profiling radar system on the CloudSat satellite in 2006. The data used here is the total attenuated backscatter at 532 nm, which is part of the Level 1 data. The attenuated backscatter profiles are derived from the calibrated, range-corrected, laser energy normalized, baseline subtracted lidar return signal. The horizontal resolution ranges from 0.33 km to 5 km and vertically from 30 to 300 meters, depending on the Altitude. The data used here is downloaded from `https://asdc.larc.nasa.gov/project/CALIPSO`, (NASA/LARC/SD/ASDC, 2017a).
For the validation of the radiative fluxes data from CERES (Clouds and the Earth's Radiant Energy System) is used. This project provides data on the Earth's radiation budget based on satellite observations. There are seven CERES instruments on five different satellites: TRMM, Terra, Aqua, S-NPP, NOAA-20. The instrument is an arrow field-of-view scanning radiometer with nadir footprint size of 10-14 km depending on the satellite. This enables high special resolution and clear-sky observations for cloud feedback studies. It measures broad band radiances of 0.3-5 μm in the short wave and of 5-35 μm in the long wave. The data used is hourly level 3b data downloaded from `https://ceres-tool.larc.nasa.gov/ord-tool/jsp/SYN1degEd41Selection.jsp` (NASA/LARC/SD/ASDC, 2017b).

7.2. MAIAC AOD

Figure 7.1 and figure 7.2 display the Aerosol Optical Depth (AOD) at 550 nm observed by MAIAC and simulated in the experiments. The scattered points in the simulations show the AOD for available MAIAC observations. The contoured lines display the simulated AOD for the whole domain. Figure 7.1 a contains MAIAC retrievals from the 31st of December 2019 00:15 UTC till 04:25 UTC. The simulations show the AOD at 550 nm at 03:00 UTC on the same day. The MAIAC AOD shows the maximum values at the south-east coast of Australia with a maximum AOD of 4.3. The AOD is further increased

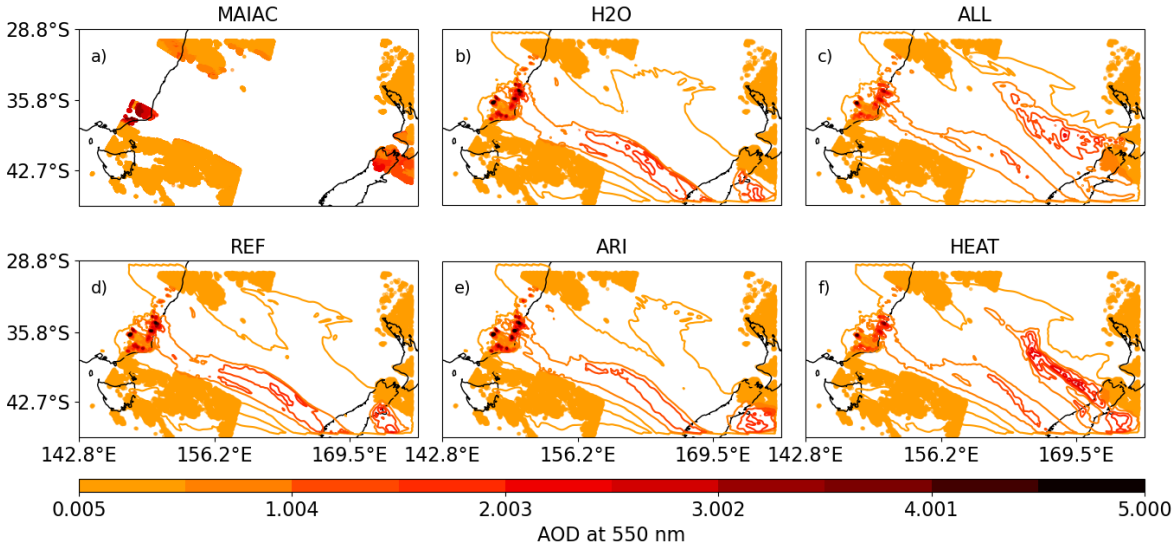

Figure 7.1.: Aerosol optical depth (AOD) at 550 nm observed by a) MAIAC and simulated in the experiments: b) H2O, c) ALL, d) REF, e) ARI, and f) HEAT on the 31st of December 2019, 03:00 UTC. The dots in b)-f) display the AOD in a grid cell closest to the MAIAC measurement. The lines represent the contours of the simulated AOD.

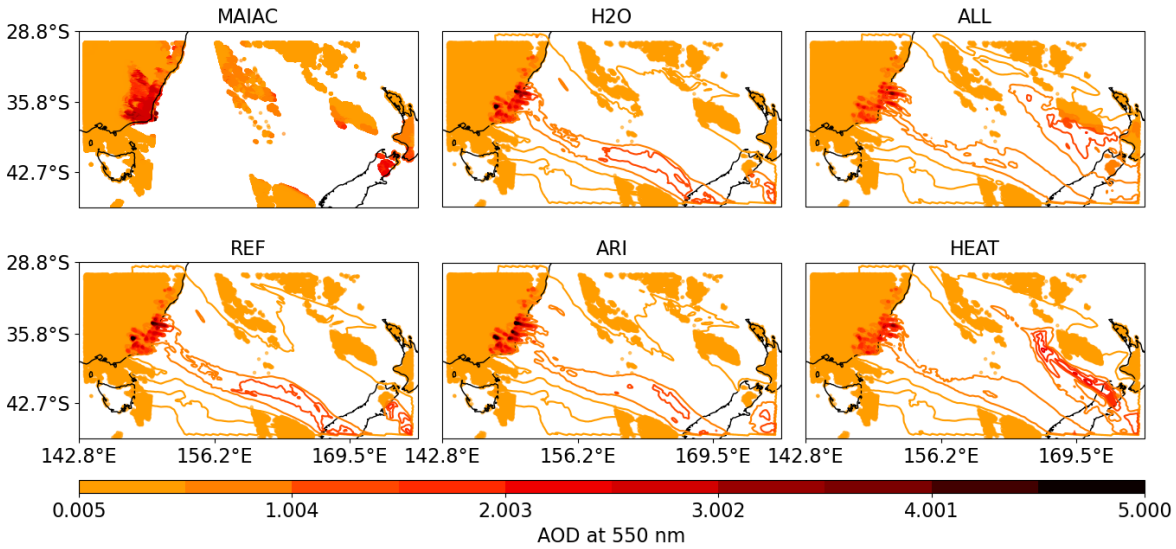

Figure 7.2.: Aerosol optical depth (AOD) at 550 nm observed by a) MAIAC and simulated in the experiments: b) H2O, c) ALL, d) REF, e) ARI, and f) HEAT on the 1st of January 2020, 02:00 UTC. The dots in b)-f) display the AOD in a grid cell closest to the MAIAC measurement. The lines represent the contours of the simulated AOD.

over the middle of New Zealand with AOD values of 3. There are two gaps, one diagonal through the domain and one meridional. The meridional gap results from the limited swath path size of the satellite. All experiments have the highest concentrations south-east of the Australian coast. The maximum AOD values are 12.8 for REF, 12.4 for H2O, 5.2 for HEAT, 13.8 for ARI and 5.42 for ALL. In REF the plume spreads south-eastwards. There is a local peak over New Zealand, but it shifts to the south in comparison with the observations. In the experiments H2O and ARI the AOD distribution is similar to REF. For the HEAT experiment the local peak over New Zealand reaches AOD values of up to 4 and is spread more widely north-west. In comparison to observations the peak is shifted slightly to the west. The ALL experiment shows a similar distribution to the HEAT experiment, but with AOD values below 3 over New Zealand. In terms of maximum AOD values the experiments HEAT and ALL fit the MAIAC data best, these two experiments also depict the local peak over New Zealand best.

Figure 7.2 a displays the MAIAC AOD at 550 nm of the 1st of January 2020 01:00 UTC-03:30 UTC. The simulations display the AOD at 550 nm at 02:00 UTC. The MAIAC retrievals show gaps again south-eastwards from the fires and some meridional gaps, the latter are again caused by the limited width of the swath path. The maximum AODs overlap with the fire areas. There is a local peak in the middle of New Zealand. A peak AOD of 4.1 is retrieved from MAIAC, in the experiments the maximum AOD values are 8.2 for REF, 8.5 for H2O, 3.8 for HEAT, 7.7 for ARI and 4.1 for ALL. The peak AOD in REF (figure 7.2 d) is above the active fires and spreads south-east. There are elevated concentrations over the middle of New Zealand but with AOD values below 2 and approximately 66 % lower than in the MAIAC retrievals. H2O and ARI show again a similar distribution to REF. For ARI the AOD values are over all lower and the local peak is shifted south-east compared to the retrievals and to REF. The HEAT experiment captures the peak over new Zealand well. In the ALL experiment the AOD over New Zealand remains below 2, and is therefore lower than in HEAT and the observations. Overall, the HEAT experiment fits the retrievals best, although it underestimates the exposure of the AOD values above 4 over land.

Moreover, the maximum AOD values in the experiments REF, H2O and ARI are with up to 12.8 very high and exceed AOD values reported for the Black Summer Fires in literature. The maximum values are only simulated in single grid cells in immediate proximity of the fire. For example, there are only 8 grid cells in REF on the 31st of December at 03:00 UTC that exceed an AOD of 5, therefore the maximum values are not representative. Li et al. (2021b) report maximum AOD values of 2.74 from AERONET observations. Additionally, they calculate the AOD based on the emission of multiple satellite fire observations. Li et al. (2021b) calculate AOD values of 12.8 in areas close to the fire and conclude that "instruments retrieving AOD in different wavelength regions are needed to understand the physical and optical properties of smoke plumes in extreme fires like the 2019–2020 bushfires". This indicates that the selectively simulated AOD values above 10 are not unrealistic.

Further, it can be seen that there are single peaks simulated over the fires, whereas the retrieval plume spreads more uniformly. It is noteworthy that the AOD above the fire areas reaches values of up to 4.

This can already result in retrieval errors (detecting dense aerosol plumes as clouds) and impact not only the MAIAC retrieval but also the GFAS FRP data. This can lead to an underestimation of the emission or missing a fire spot completely. It is also evident that the retrieval gaps match well with the high simulated AOD values.

Further, it can be seen that moisture release and aerosol-radiation interaction have little impact on the horizontal distribution of the plume, whereas sensible heat release shows clear differences, not only in the patterns but also in the maximum AOD. The initial heat release increases the emission height to levels with higher wind speeds. This increases the dilution of the plume. The dilution is even stronger in the ALL experiment.

Overall, the comparison with MAIAC data is challenging, firstly because of the large observation gaps, due to overpassing times, but probably also due to high AOD cause by the extreme aerosol loadings. Therefore, large parts of the simulated plume are not captured. This is underlined by the contour lines, which fit well in the MAIAC data gaps. The distribution in the ALL and HEAT experiment fits the data and the gaps best. According to Levy et al. (2013) a normal value range for confident AOD retrievals is 0–1.0 with up to 5.0 for satellites and 7.0 for AERONET retrievals. This indicates possible retrieval errors.

In order to simulate the correct AOD the concentration and the aerosol optical properties need to be captured well. Both parameters are given with uncertainties. The assumptions of the optical properties are discussed in section 4.5.4. The uncertainties in emission flux and injection heights are established in the previous chapter. Nevertheless, it can be concluded that the simulated AOD is overall in an agreeable range. Therefore, the optical properties appear to be reasonable.

7.3. NASA 3D winds plume height

For the following analyzes the plume and cloud height retrievals from NASA 3D winds are compared to the simulated plume and cloud heights. A quality flag is used to remove poor retrievals. Nevertheless, the data is given with an accuracy of approximately 200 m. For the simulations the retrieval mask is used as well. Because the retrieval is not able to separate clouds from aerosols the plots display either the plume or the cloud top height. The plume is defined as a grid cell that exceeds an AOD at 550 nm of 0.005 and a cloud is defined as a grid cell that exceeds a mass mixing ratio of cloud water and cloud ice of 0.05 g kg^{-1}.

Figure 7.3 displays the 3D wind retrieval in comparison to the five experiments on the 31st of December between 02:45 and 4:25 UTC and the simulation at 03:30 UTC. The retrieval in figure 7.3 a shows a feature almost diagonal through the domain, which consists of the aerosol plume overlapping with clouds. Within that feature there is a convective cell arising south-east of the Australian coastline, with maximum altitudes of 20.0 km. There is a feature in the northern center of the domain connected to clouds that is simulated in all the experiments. The REF experiment shows similar features as the retrieval. There are

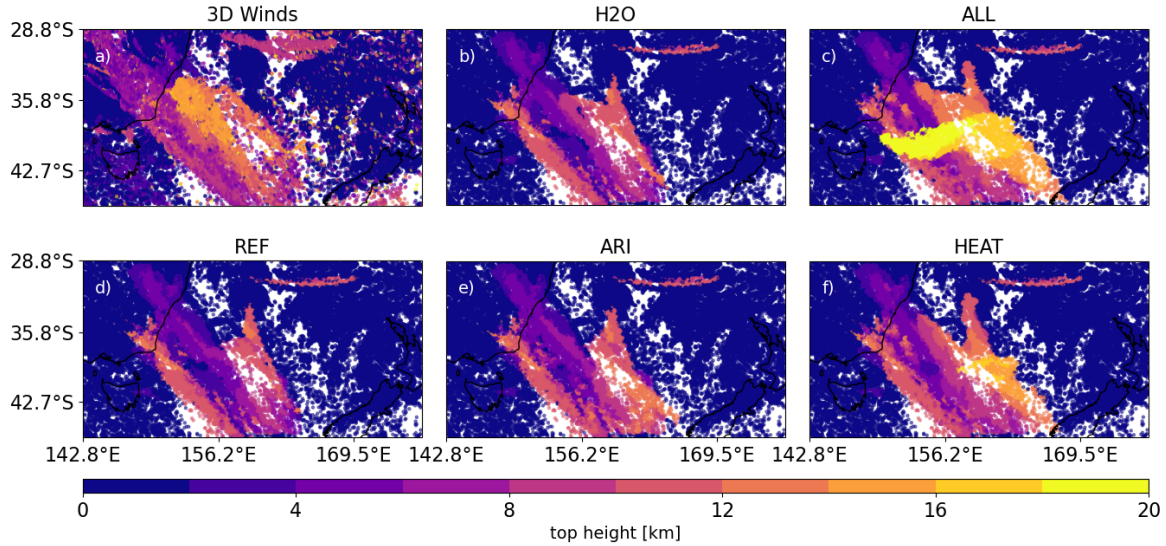

Figure 7.3.: Aerosol and cloud top height a) retrieved by the NASA 3D wind algorithm and simulated in the experiments: b) H2O, c) ALL, d) REF, e) ARI, and f) HEAT on the 31st of December 2019, 03:30 UTC. The dots in b)-f) represent the top height of either the aerosol plume (grid cell that exceeds an AOD at 550 nm of 0.005) or a cloud (a grid cell that exceeds a mass mixing ratio of cloud water+cloud ice of 0.05 g kg^{-1}).

two elevated areas, one shifted to the south-east and one shifted to the north-west in comparison to the observations. The maximum height is with 13.0 km below the retrieved maximum height. The H2O experiment is similar to REF. The elevated areas are shifted slightly and the maximum altitude is increased by 0.9 km. The ARI experiment is again similar to REF but shows more elevation downstream of the plume, with a top height of 13.0 km. In the HEAT experiment there is a clear elevation downstream from the coast that matches the observations well. The maximum altitude is 17.4 km. In the ALL experiment there is a dominant elevated feature south-east of the Australian coast spreading eastwards with maximum altitudes of 20.2 km. The average heights of the plume and cloud above 2 km are 8.3 km for the retrieval, 6.6 km for REF, 6.9 km for H2O, 7.1 km for ARI, 8.1 km for HEAT and 10.1 km for ALL. This outlines the underestimation of the REF experiment. For H2O the maximum height is increased but there are only small changes in the average plume height. For ARI the top height does not change but the whole plume is lofted due to aerosol-radiation interaction. The HEAT experiment agrees best with the observation not only in terms of the position but also in average height. The ALL experiment fits best with maximum height but in the simulation the elevated feature is higher, whereas the retrievals only reach altitudes of 20 km selectively. This is outlined by the average height that is 1.8 km above the observations.

Figure 7.4 is structured the same way as figure 7.3, but shows the 1st of January 03:30 UTC. The feature in the 3D winds retrieval is again spreading diagonally, increasing the height as it moves south-east from the Australian coast with maximum altitudes of 19.9 km over New Zealand. There is a separated elevated area south-west of the feature, which is missed in all experiments. The REF experiment shows a similar structure, with the highest areas over New Zealand but shifted to the south and with lower

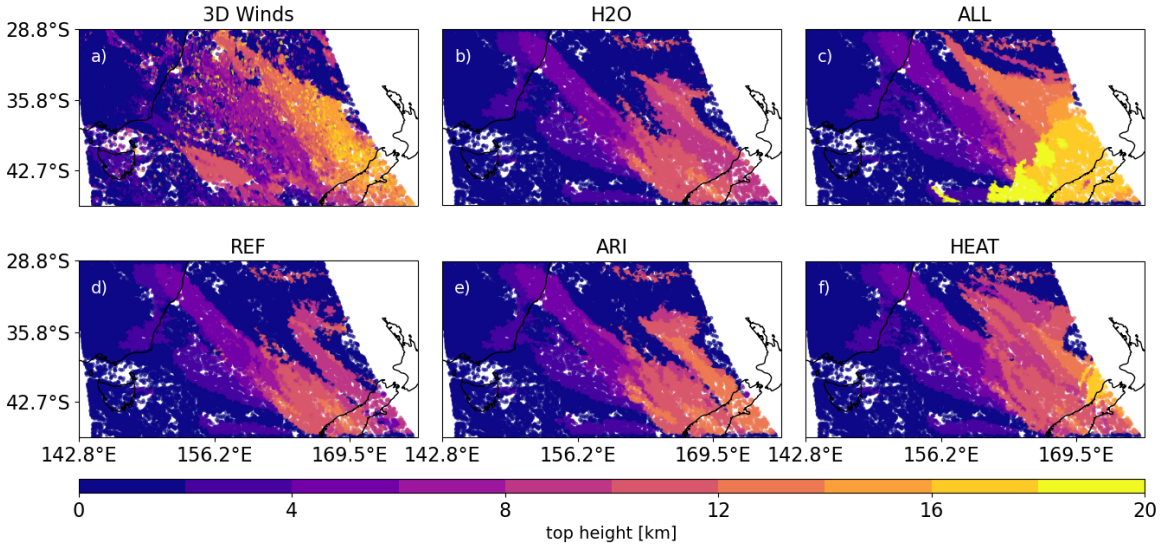

Figure 7.4.: Aerosol and cloud top height a) retrieved by the NASA 3D wind algorithm and simulated in the experiments: b) H2O, c) ALL, d) REF, e) ARI, and f) HEAT on the 1st of January 2019, 03:30 UTC. The dots in b)-f) represent the top height of either the aerosol plume (grid cell that exceeds an AOD at 550 nm of 0.005) or a cloud (a grid cell that exceeds a mass mixing ratio of cloud water+cloud ice of 0.05 g kg^{-1}).

elevation, outlined by a maximum altitude of 12.6 km. The H2O experiment is again similar to REF but the elevated area is spread more widely. The top height is 12.6 km as well. The ARI experiment is distributed similarly, but elevated with a maximum height of 13.5 km. In HEAT the distribution and heights match the observations well. The maximum height is 16.9 km and located over the center of New Zealand. The ALL experiment shows similar spreading to HEAT, but elevated and with an additional feature in the southern center of the domain, which reaches maximum heights of 20.2 km. The mean plume heights above 2 km are 8.4 km for the retrieval, 6.4 km for REF, 6.7 km for H2O, 7.0 km for ARI, 7.4 km for HEAT and 9.3 km for ALL. Here again, REF, H2O and ARI underestimate the observed heights in maximum and average height. The plume top and average heights in ALL fit the observations best, although the most elevated area in ALL is not shown in the 3D winds retrieval. This feature results from the elevated plume on the previous day (figure 7.3 c).

Overall, the simulations of all the experiments fit the observations well. There is an underestimation of the top height in REF and H2O. The moisture release affects the early stage of the plume development, while aerosol-radiation interaction lofts the plume over time. In ARI the top heights are underestimated at the beginning of the simulation but as the plume rises due to aerosol-radiation interaction the top heights align with the observations compared to REF. The HEAT experiment fits the retrievals best in both cases. The top heights are comparable, but with a shift in the peak area. For the second case the HEAT experiment also underestimates the plume heights, as analyzed before the FRP decreases over time, therefore the initial lofting effect is expected to decreases as well. In the ALL experiment a distinct arising of the plume is simulated, which overestimates the retrieved plume height. Nevertheless, with this

setup pyro-convection and additional cloud formation is simulated, which enables a transport of aerosols to the upper troposphere/lower stratosphere region. A process that many NWP models fail to simulate.

7.4. CALIPSO attenuated backscatter

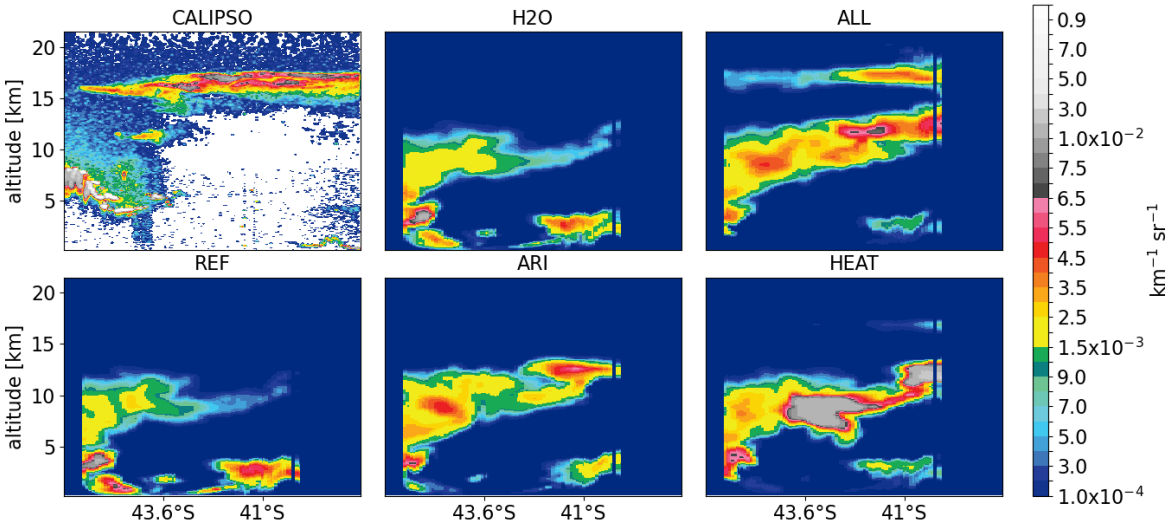

Figure 7.5.: a) CALIPSO attenuated backscatter at 532 nm and the simulated backscatter at 532 nm in the experiments: b) H2O, c) ALL, d) REF, e) ARI, and f) HEAT on the 1st of January 2020 at 13:30 UTC.

In this section the CALIPSO attenuated backscatter at 532 nm is compared to the simulated backscatter at 532 nm in the experiments. Figure 7.5 displays the cross section of the satellite passing over New Zealand close to the eastern boundary of the domain on the 1st of January 2020 at 13:30 UTC. The satellite path can be found in appendix B.1. Figure 7.5 shows a stratiform signal between 17.5 and 15.0 km through almost all of the cross section, decreasing between 46°S and 44°S. Underneath the signal, the white area indicates that retrieval is not possible due to the dense cloud/aerosol plume. There is a second signal at 46°S at 7.7 km decreasing to 2.5 km at 44°S. The REF experiment in figure 7.5 d differs from the observation, the strongest signal is at 45.5°S from the ground up to 5 km. This is 2 km lower than the observation, but weaker signals are simulated up to an altitude of 11 km. There is a second signal below 5 km between 42°S and 40 °S, which cannot be evaluated due to the missing signal in the CALIPSO data. The observed stratiform layer is not simulated. The backscattering in the H2O experiment is similar to REF. For ARI, the plume is lofted to 12.5 km and distributed more widely. The shape is a more stratiform in comparison to REF, but still underestimates the observed height by 5 km. Moreover, the signal strength is underestimated. The backscatter in the HEAT experiment is increased between 7.0 km and 10.0 km between, 44°S and 41.5°S and again between 11 km and 13 km between, 41°S and 40°S. There is a small signal at 17.5 km. In the ALL experiment the signal at 46°S to 40°S is increased in height and there is stratiform layer around 17.5 km. Although the signal strength in the ALL experiment is lower, it compares best to the CALIPSO data. The CALIPSO algorithm classifies that signal as a mixture of

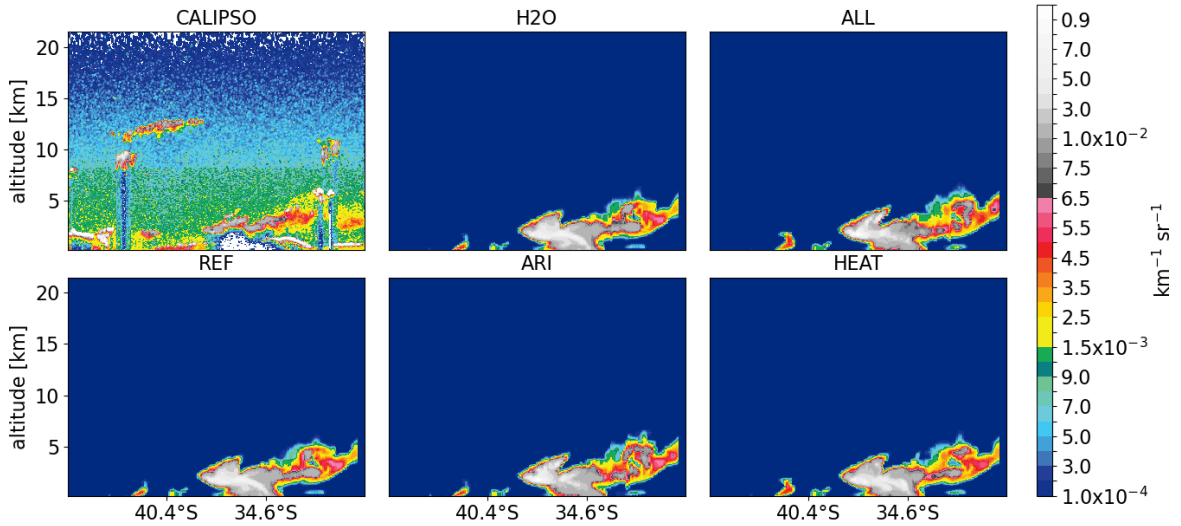

Figure 7.6.: a) CALIPSO attenuated backscatter at 532 nm and the simulated backscatter at 532 nm in the experiments: b) H2O, c) ALL, d) REF, e) ARI, and f) HEAT on the 1st of January 2020 at around 15:30 UTC.

aerosol and cloud. The cloud backscatter is not included in the model.

Figure 7.6 displays the cross section of CALIPSO south of the Australian coast on the 1st of January 2020 at around 15:30 UTC. The CALIPSO data shows backscattering between 46°S and 39°S between 2 km and 5.0 km. There is further backscattering at 31°S at 10 km, at 34°S at 8 km and between 43°S -38°S at 12 km. These signals are classified as clouds by the CALIPSO algorithm. The model simulates clouds in these areas as well. This is also the case for the signals south of 43°S. The REF experiment fits the observations well, the signals below 2 km north of 43°S are captured. The signal north of 38°S agrees well in height and magnitude. The other experiments are very similar to the REF experiments and therefore also fit the observations well.

Figure 7.5 displays the aerosol plume, which is approximately 2 days old at the time. Sufficient time to induce a detectable lofting in the ARI experiment due to aerosol-radiation interaction. With the increased emission height in the HEAT experiment more aerosols are transported to higher levels, creating a stronger backscatter around 10 km. Only the ALL experiment is able to simulate the stratiform layer, visible in the CALIPSO data, with higher aerosol concentrations in the upper levels due to increase of emission height by heat and moisture release and the lofting due to aerosol-radiation interaction. Further, the heights in ALL and the CALIPSO data match well, in contrast to the overestimation suggested by the NASA 3d wind retrievals.

This raises the question, why are the experiments in figure 7.6 so similar? Firstly, the age of the plume is different. In figure 7.6 the plume is close to the source on the 1st of January. It has been established that on this day the FRP is smallest, therefore the moisture and heat released is lower. Secondly, the overpass is during the night, when the atmosphere is more stable. This generally decreases the vertical transport in all experiments. The diurnal cycle reduces the heat and moisture during the night and further, and the

aerosol-radiative effects are limited to terrestrial radiation and remain small. All this reduces the effect of the implemented features, leading to similar results.

7.5. CERES SW upwards flux TOA

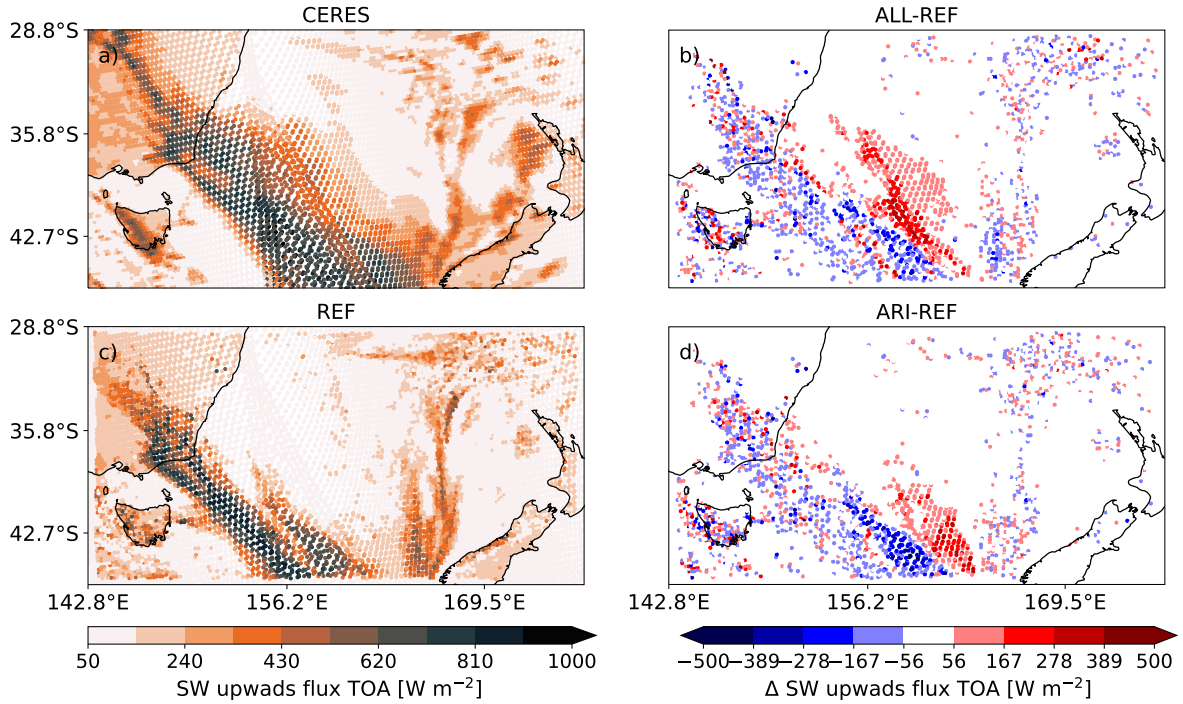

Figure 7.7.: a) CERES short wave (SW) upwards flux top of the atmosphere (TOA), c) simulated SW upwards flux TOA in REF and the difference d) ARI-REF and b) ALL-REF.

This section compares the CERES short wave (SW) upwards flux top of the atmosphere (TOA) to the experiments REF, ARI and ALL. The SW upward flux indicates how much solar radiation is reflected or scattered back to the top of the atmosphere. For example, the SW upwards flux is larger over land than over the ocean, because the ocean has a low albedo. Clouds with a very high albedo reflect solar radiation well and aerosols scatter solar radiation as well. Figure 7.7 a displays the CERES data on the 31st of December at 13:00 AEDT. The SW upwards flux is increased along the north-west corner of the domain to the center at the southern boundary. It has been established that in these areas clouds and aerosols are present. Within this feature a maximum SW upwards flux of 1494.8 W m^{-2} is reached. There is an increase north-south of the domain and in the north-eastern corner. There are further clouds in this area. The REF does not consider aerosol-radiation interaction, therefore notable features are only related to clouds. The cloud band spreading south-east is narrower than the CERES data. The cloud signal in the eastern half of the domain is captured well. Figure 7.7 d displays the difference of ARI-REF. In cloudy areas there is noise, which results from small perturbations induced by the aerosol-radiation interaction, that creates noise in the cloud patterns. There is an increase east of the cloud band by up to

464.6 W m^{-2}. The signal in the area of the cloud band decreases by up to 642.2 W m^{-2}. This difference is caused by the aerosol plume. The scattering of the plume increases the SW upwards flux for clear sky conditions but decreases it, when positioned above clouds, reducing the clouds high reflectivity. The ALL-REF difference in figure 7.7 b shows a similar pattern. The area of increase is larger and matches the CERES observation best. Even though the reduction due to the aerosol-radiative effect is large with over 600 W m^{-2}, it is difficult to validate this effect with the given data. The interaction of clouds and aerosols makes it difficult to determine the respective contribution to the SW upwards flux. Furthermore, the semi-direct aerosol effect impacts the cloud cover and theses changes further impact the SW upward flux. The widening of the signal in ARI and ALL matches the wider feature in the CERES data, but the reduction of SW upward flux by the aerosol-radiative effects is difficult to evaluate.

8. Conclusions and outlook

The aim of this work is a better understanding of the development of vegetation fire plumes and a better representation of these in NWP models with interactive aerosols. The focus of this work is how moisture release, sensible heat release by the fire and aerosol-radiation interaction influence the plume height, transport and cloud formation. Therefore, I implemented a parameterization for the emission of combustion and fuel moisture by the fire. I included sensible heat release by the fire, based on fire radiative power (FRP) measurements from GFAS, and implemented the optical properties for biomass burning aerosols in two size modes and two mixing states, based on Mie calculations.
Firstly, I compared a plume-parameterizing simulation with 6.6 km grid spacing and a plume-resolving setup with 600 m grid spacing. The latter simulates plume rise based on moisture and sensible heat release and resolving convection. Pyro-convection in high resolution setups has been simulated in several previous studies (Luderer et al., 2006; Luderer, 2007; Thurston et al., 2015; Trentmann et al., 2006), mostly for idealized setups. With the setup developed in this study, I am able to simulate a selected and well observed case study of significant magnitude, and answer the research questions stated in the introduction:

1. **How does moisture and sensible heat release by the fire impact the plume height and pyro-convection in a convection-resolving setup and how does it differ from a parameterized plume height?**

   Including moisture and sensible heat release in a convection resolving setup increases the plume top height by 7.6 km. The moisture and heat release is proportional to the GFAS FRP. In the area of the highest FRP moist convection is triggered. This results in liquid and ice cloud formation. An increase in moisture emission by a factor of 20 has small impacts on the plume top and mass weighted height (maximum increase of 700 m) but triggers moist convection earlier in the day and increases the LWP and IWP. The increase of the sensible heat by 36 % increases the mass weighted plume height by up to 60 % and moist convection is triggered even earlier in the day. The LWP and IWP are increased even more strongly than for increased moisture release. For a decrease in sensible heat release by 36 % moist convection is rarely triggered and the plume top height is comparable to the experiment without moisture and sensible heat release. The plume-rise model parameterizes pyro-convection based on the atmospheric conditions and a heat flux according to the vegetation type in the grid cell. The vegetation type in the grid cell remains constant, therefore the atmospheric conditions are the only variables determining the diurnal cycle of the emission profile. In the plume-resolving setup aerosols and moisture are emitted in the lowermost model

layer. Atmospheric stability and the sensible and latent heat then determine the buoyancy. Here, the sensible heat released is weighted with a diurnal cycle. The plume-resolving experiment has generally lower plume heights during the day and larger plume heights during the night, compared to the plume-parameterizing experiment. The plume top heights are comparable. The dependency on the FRP, which is proportional to the sensible heat and moisture release results in a wide range of plume heights, especially if moist convection is triggered.

The simulations show the explicit simulation of pyro-convection and pyro-cumulus formations. The sensitivity experiments show that sensible heat release is the dominant contributor and the high relative humidity of the background meteorology makes the moisture release by the fire small in comparison. This agrees with Luderer et al. (2006). The plume top height of the plume-parameterizing experiment can be reproduced if moist convection is triggered. Overall, a wider range of plume heights is simulated in high resolution setup. This concurs with Val Martin et al. (2010).

Secondly, the moisture and sensible heat release, as well as the aerosol-radiation interaction are coupled with the plume-rise model to address the issue of underestimation of plume injection heights for intense fires, as presented by Val Martin et al. (2010). For the implementation of the aerosol-radiative effects an analysis of the aging and internal mixture of the aerosols is performed. This is necessary to determine the input parameters required for the Mie calculations of the aerosol optical properties. The simulated case is again the Australian New Years Event. Based on this, it is possible to answer the research questions formulated in the introduction:

2. **What is the impact of moisture and sensible heat release by the fire on the plume evolution and cloud formation in a plume-parameterizing setup?**
   The impact of moisture release is most dominant within the first 12 hours of the simulation, when the emissions are highest. Water vapor is emitted at altitudes where clouds are already existing. This increases cloud water and ice close to the emission source. Latent heat release induces a buoyancy, which slightly increases the plume height, while at the same time cloud-radiative effects reduce the surface temperature. Therefore, the plume-rise model simulates the emission height assuming of a more stable atmosphere, which leads to a reduced injection height. The introduction of moisture release creates noise in the LWC and IWC within the plume with no systematical change from the second simulation day onward. The effect in the plume evolution is small.
   The introduction of sensible heat release by the fire increases the near surface temperature by up to 18 K. This not only generates an updraft but also increases the injection height calculated by the plume-rise model due to a destabilized atmosphere. This increases the plume top height by up to 3 km within the first 4 hours of the simulation. The strong buoyancy leads to cloud formation (increase in cloud water and ice) close to the fire source. This creates additional buoyancy due to latent heat release. The rising of the plume to levels with different wind fields leads to a wider

horizontal distribution of the plume and has a strong effect on the transport within the first three days.

3. **Does aerosol-radiation interaction induce a self-lofting of the plume within the first three days? How does the semi-direct aerosol effect manifest itself?**
   Aerosol-radiation interaction causes heating at the plume top and reduces the solar radiation reaching the surface. The SW net flux is selectively reduced by up to 80.2 %, which reduces the near surface temperature by up to 7 K. Further, the plume top absorbs solar radiation. This leads to a stabilization of the atmosphere, especially during the night. The plume is not stratiform, therefore the effect takes place on different height levels but creates an overall updraft within the plume, which increases plume top and mass weighted height from the second day onward. There is a semi-direct effect due to the destabilization of the atmosphere during the day, which increases cloud ice formation within the plume by up to 26.0 %, and due to the stabilization of the atmosphere during the night, which reduces cloud water by up to 38.32 %. With the performed experiments it is not possible to differentiate between the aerosol-radiative effect and the cloud-radiative effects because the changes in cloud cover (beside the noise) are placed within the aerosol plume. Therefore, the contribution of the cloud/aerosol-radiative feedback cannot be quantified.

Thirdly, an experiment in a plume-parameterizing setup including the moisture and heat release by the fire and the aerosol-radiation interaction is performed. The effect of moisture and sensible heat release is dominant during the first 6 hours of the simulation. The emission height is increased due to the destabilization of the atmosphere and cloud water and ice increase close to the fire. Aerosol-radiation interaction increases cloud ice formation during the day and reduces liquid clouds during the night. The lofting of the plume is even stronger, because of the increased emission height, which leads to a wider horizontal spreading of the plume and positions more aerosols above clouds.
In order to evaluate these impacts the experiments are compared to observational data. AOD comparisons of the simulations with MAIAC is found to be difficult, due to large gaps in the measurements, but overall agree in distribution and magnitude. Cloud and plume top heights are compared to NASA 3D wind height retrievals. The top heights are underestimated except for the experiment including sensible heat release and including all implementations. The experiment including all implementations overestimates the heights, but it is able to reproduce a convective cell arising, which is also visible in the retrievals. CALIPSO data is further used although, this data only captures the plume selectively. For the aged plume that originates from the simulation start the experiment with all implementations is the only experiment able to reproduce the signals seen in the CALIPSO data. This further confirms that plume top heights are not generally overestimated as suggested in the comparison with the 3D wind retrievals. Lastly, the SW radiative flux at the top of the atmosphere is compared with CERES data. This comparison is difficult, because of the overlap of the aerosol plume and the cloud band. The comparison with observations for this case study is overall difficult, on the one hand because of the dense aerosol plume, which may be

recognized as a cloud, and on the other hand because of the mixing of clouds and the aerosol plume. Selective measurements, e.g. AERONET data or air quality measurements can diverge strongly from the model for small shifts of the simulated plume to the real one.
The motivation to improve the description of biomass burning plumes in NWP models or rather chemical transport models is to quantify the impact of these aerosols on the air quality, and therefore the human health. Additionally, these aerosols have a strong impact on the Earth's radiation budget and the injection height is decisive for the plume transport. In comparison with observations the developments in this study show an overall improvement in the representation of the aerosol plume. It is outlined that the impacts of moisture and heat release are significant on the first day with the strongest FRPs. This suggests that these implementations are most relevant for extreme fire events. The sensitivity of the injection height on the plume evolution has been outlined and remains with high uncertainties. Therefore, it is not determined that the improvement shown in this work are generally applicable to future case studies.

Outlook

The results in section 5.1 suggest that for plume-resolving simulations the sensible heat release is the dominate determining factor of the plume rise and the vertical transport of the aerosol mass. Moist convection appears to be more sensitive to the sensible heat release than the moisture release. In this work the sensitivity of both is only tested towards the assumptions used in the plume-rise model. A more comprehensive sensitivity study could determine the exact values of sensible heat, moisture release and the combination of both required to trigger moist convection. Further analysis of plume and cloud dynamics, like updraft strengths, entrainment and vorticity can help understand what drives and determines the plume evolution.
Luderer et al. (2006) and Thurston et al. (2015) suggest that the moisture release by the fire is less important than the background moisture. The simulation period in this study was deliberately chosen, because of its multiple pyro-Cb outbreaks, therefore it would be interesting to extend the current setup to additional test cases with comparable FRP but different meteorological conditions. Based on this it could be determined if the findings are generally applicable.
The simulations with fine grid resolution are limited to comparably small domains, which are not suitable for the study of long-range transport. The limits of currently used plume-rise models in numerical weather and climate models have been discussed and demonstrated. A different approach would be the use of machine learning to predict the emission height. Data generated by extensive plume-resolving sensitivity studies would provide useful training data for a neural network. The simulation setups could be similar to the setup introduced in this study, testing the sensitivity of moisture release, different meteorological backgrounds, heat release by the fire and vegetation types on the emission height.
In a next step, the dependency of the plume rise on the grid spacing could be tested. How do the plume heights change with the same setup but different grid spacing of 300 m or 100 m? The Freitas plume

rise model used a resolution of 100 m (Freitas et al., 2006), how would a plume-resolving setup with a resolution of 100 m compare to the plume-rise model?

The effect of sensible heat release strongly increases the plume heights and creates cloud formation close to the fires even with a relatively coarse grid spacing of 6.6 km. For a grid spacing of 3.3 km it is possible to resolve convection. This raises the question of how plume heights change in a convection resolving setup of 3.3 km grid spacing without plume-rise model. Would this setup be able to simulate moist convection?

So far only aerosols are emitted by the fire, but vegetation fires are also a source of chemically active gases (nitric oxide, carbon monoxide and volatile organic compounds) and long-lived halogenated compounds that can impact atmospheric chemistry. In the case of the Black Summer Fires, it has been reported that emissions penetrating the tropopause resulted in a remarkable ozone depletion (Heinold et al., 2022). With the setup in this study, it is possible to simulate the penetration of the tropopause. Future work can make use of this and simulate chemical components and their effect in the troposphere and stratosphere.

The evaluation of the simulations results is challenging due to limited observational data. The NASA 3D wind retrievals have been extended and now also include the option to use the two geostationary satellites: GEO-KOMPSAT-2 (over Korea) and the Himawari-8 for wind and height retrievals (based on personal communication with Dr. Jim Carr, jcarr@carrastro.com). This option has a coarser spatial resolution, but enables retrievals every 10 min, regardless of the overpass times, and can provide useful information on the evolution of the aerosol plume, including observation of the fire peak and the initial emission height.

A. Appendix for chapter 6

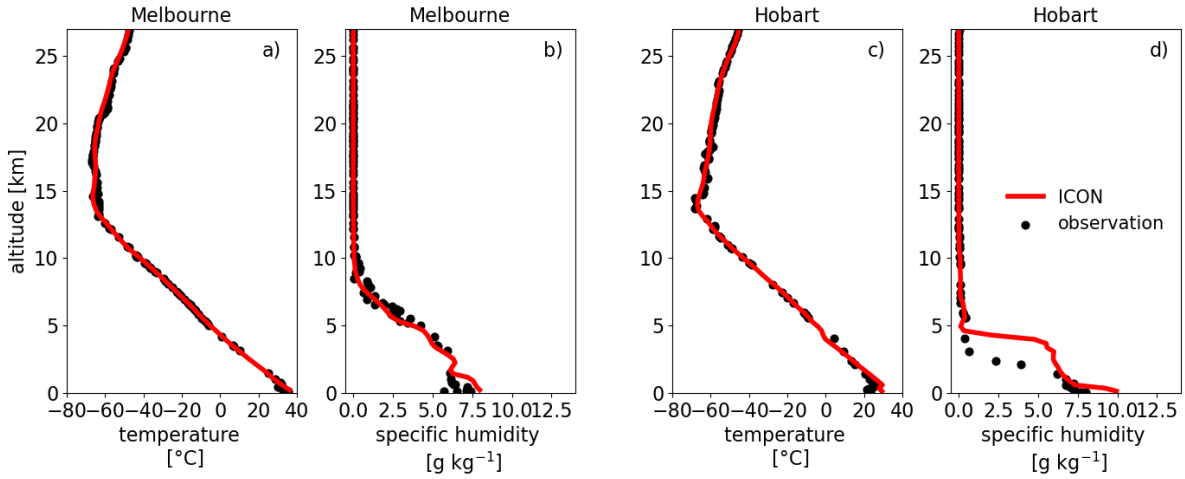

Figure A.1.: Comparison of radio soundings (black dots) and ICON simulated (red lines) a) temperature in Melbourne, b) specific humidity in Melbourne, c) temperature in Hobart, and d) specific humidity in Hobart at the 30th of December 2019 11:00 AEDT.

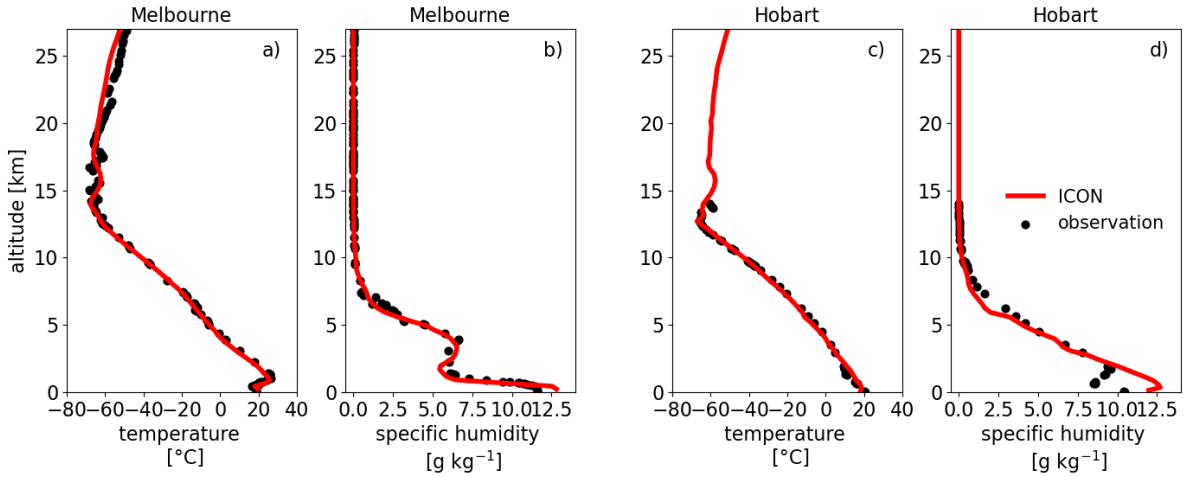

Figure A.2.: Comparison of radio soundings (black dots) and ICON simulated (red lines) a) temperature in Melbourne, b) specific humidity in Melbourne, c) temperature in Hobart, and d) specific humidity in Hobart at the 30th of December 2019 23:00 AEDT.

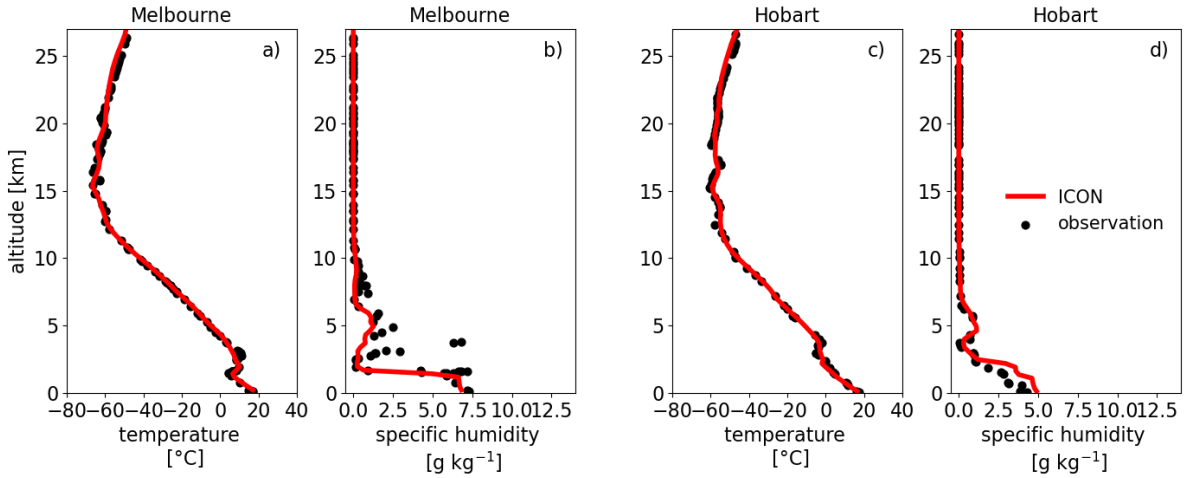

Figure A.3.: Comparison of radio soundings (black dots) and ICON simulated (red lines) a) temperature in Melbourne, b) specific humidity in Melbourne, c) temperature in Hobart, and d) specific humidity in Hobart at the 31st of December 2019 11:00 AEDT.

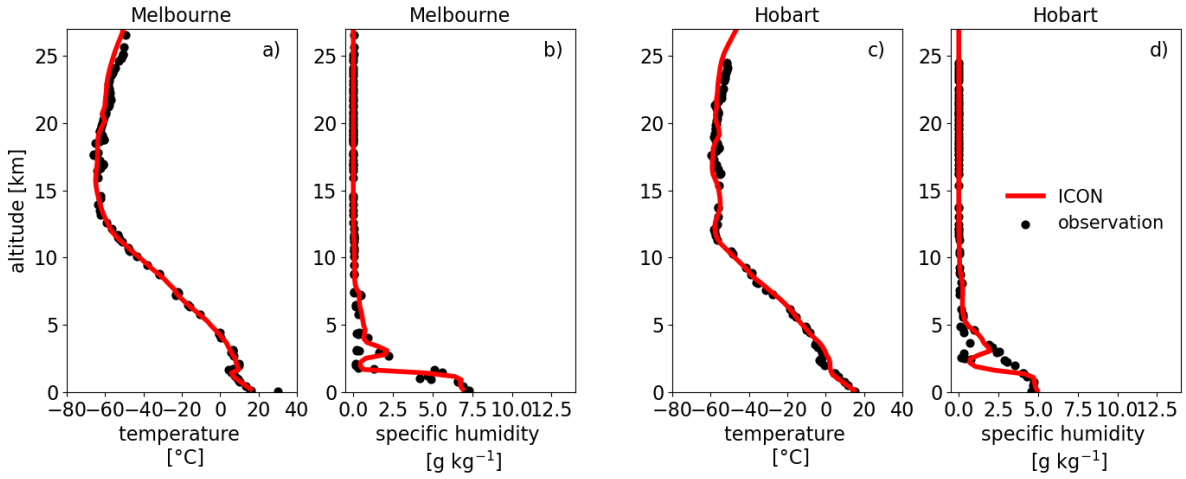

Figure A.4.: Comparison of radio soundings (black dots) and ICON simulated (red lines) a) temperature in Melbourne, b) specific humidity in Melbourne, c) temperature in Hobart, and d) specific humidity in Hobart 31st of December 2019 23:00 AEDT.

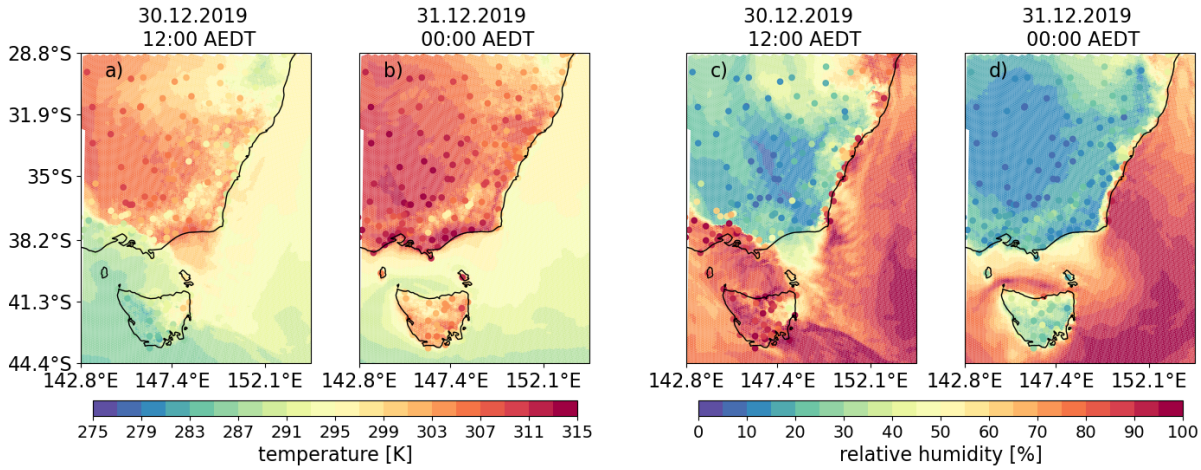

Figure A.5.: Measurements of automated weather stations (colored dots) compared to REF. a) temperature and b) relative humidity on the 1st of 30th of December 2019 12:00 AEDT, and c) temperature and d) relative humidity at the 31st of December 2019 00:00 AEDT, all in the lowermost model level.

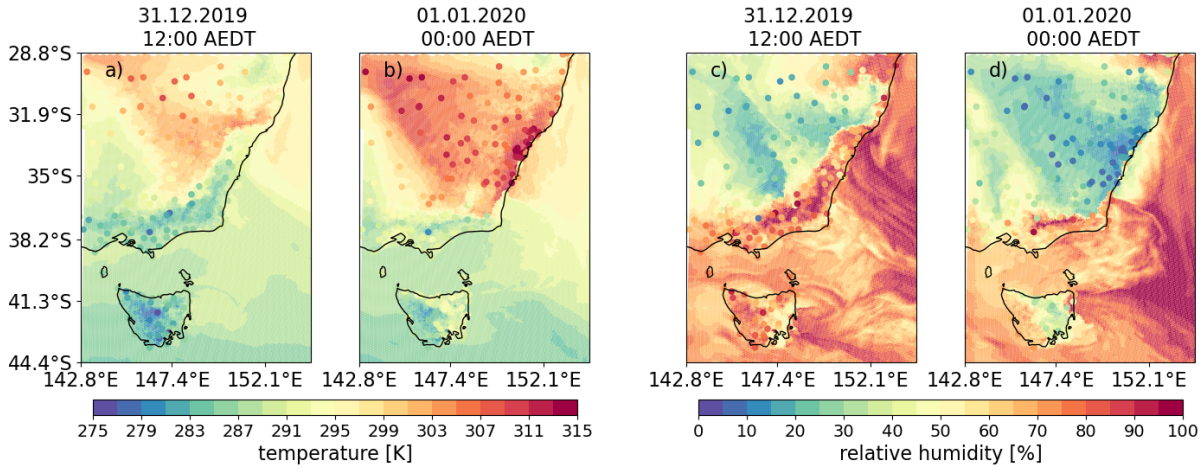

Figure A.6.: Measurements of automated weather stations (colored dots) compared to REF. a) temperature and b) relative humidity on the 1st of 31th of December 2019 12:00 AEDT, and c) temperature and d) relative humidity on the 1st of January 2020 00:00 AEDT, all in the lowermost model level.

Figure A.7.: Comparison 3-hourly mean PM2.5 air quality measurements and simulated ICON-ART organic and black carbon.

Figure A.8.: Comparison 3-hourly mean PM2.5 air quality measurements and simulated ICON-ART organic and black carbon.

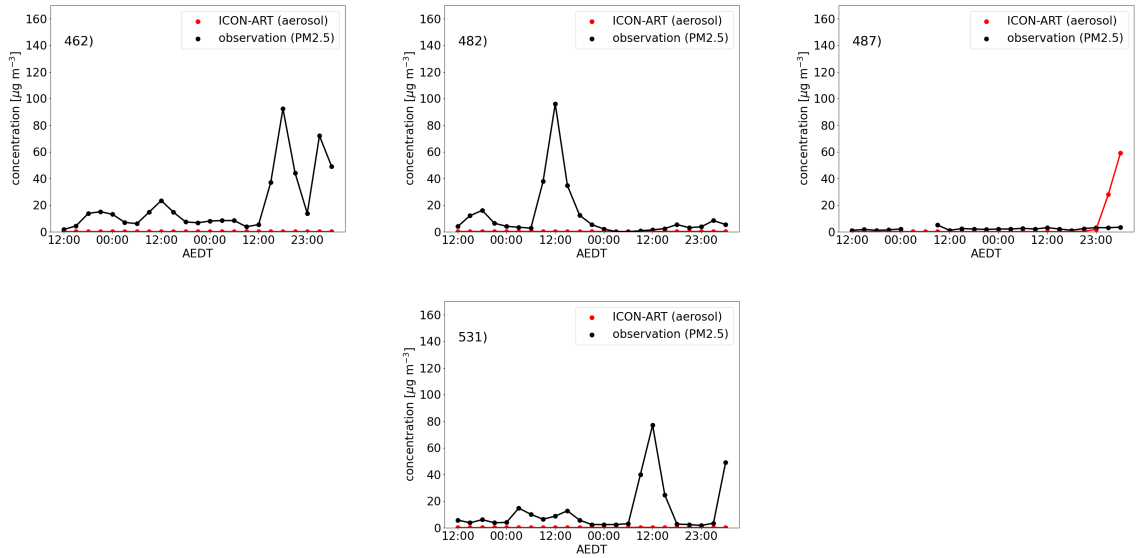

Figure A.9.: Comparison 3-hourly mean PM2.5 air quality measurements and simulated ICON-ART organic and black carbon.

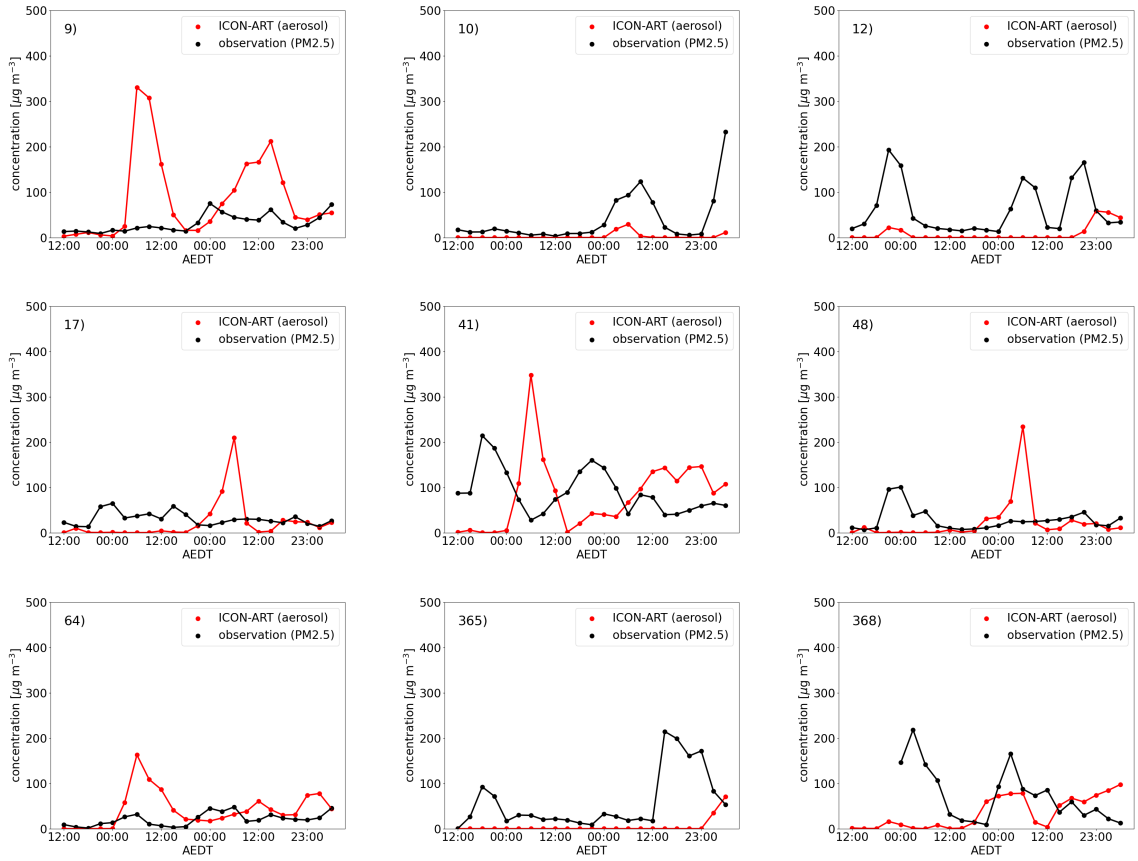

Figure A.10.: Comparison 3-hourly mean PM2.5 air quality measurements and simulated ICON-ART organic and black carbon.

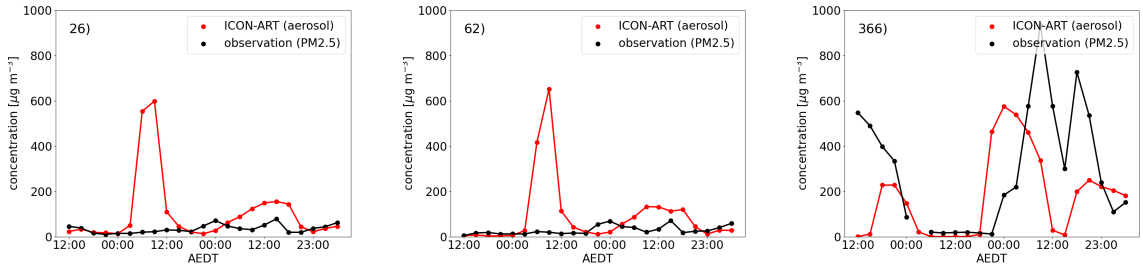

Figure A.11.: Comparison 3-hourly mean PM2.5 air quality measurements and simulated ICON-ART organic and black carbon.

Table A.1.: Summery of air quality measurement stations (part 1).

station_id	station	state	lat	lon	station_monitoring_region
371	armidale	NSW	-30,50845	151,661658	Northern Tablelands
9	albion_park_south	NSW	-34,57783844	150,7825381	Illawarra
373	rouse_hill	NSW	-33,682762	150,903713	Sydney North-west
11	bargo	NSW	-34,30624563	150,5806198	Sydney South-west
364	lismore	NSW	-28,83213	153,2935	Bushfire - Lismore (offline)
370	port_macquarie	NSW	-31,447762	152,876525	Mid-North Coast
369	liverpool_swaqs	NSW	-33,91889	150,93252	Research Monitoring
372	cook_and_phillip	NSW	-33,872468	151,213337	Sydney East
13	beresfield	NSW	-32,79678858	151,6610103	Lower Hunter
375	bradfield_highway	NSW	-33,84344834	151,2114197	Roadside Monitoring
42	parramatta_north	NSW	-33,7995094	150,997805	Sydney North-west
39	narrabri	NSW	-30,318409	149,829342	North-west Slopes
37	muswellbrook	NSW	-32,27165795	150,8857132	Upper Hunter
374	coffs_harbour	NSW	-30,298315	153,118125	Mid-North Coast
46	rozelle	NSW	-33,86434613	151,1639427	Sydney East
21	carrington	NSW	-32,90966046	151,7633362	Newcastle Local
17	camberwell	NSW	-32,47233	151,091919	Upper Hunter
368	katoomba	NSW	-33,710323	150,299539	Research Monitoring
24	gunnedah	NSW	-30,98178258	150,2607372	North-west Slopes
366	goulburn	NSW	-34,73455	149,724216	Southern Tablelands
10	albury	NSW	-36,051849	146,9399	South-west Slopes
12	bathurst	NSW	-33,401824	149,574583	Central Tablelands
365	orange	NSW	-33,274327	149,094472	Central Tablelands
57	wallsend	NSW	-32,8943912	151,6702075	Upper Hunter
53	tamworth	NSW	-31,109889	150,914528	North-west Slopes
454	bourke	NSW	-30,0362	145,952	Western LLS
458	cobar	NSW	-31,4837	145,829	Western LLS
34	mayfield	NSW	-32,88493327	151,7284241	Newcastle Local
64	wyong	NSW	-33,27894899	151,4324233	Central Coast
62	wollongong	NSW	-34,41706803	150,8873283	Illawarra
531	wagga_wagga_north_dt	NSW	-35,104407	147,360512	Riverina LLS
52	stockton	NSW	-32,90201075	151,7843047	Newcastle Local
51	st_marys	NSW	-33,79515754	150,7667978	Sydney North-west
48	singleton	NSW	-32,55663634	151,1786497	Upper Hunter
45	richmond	NSW	-33,61643788	150,7473356	Sydney North-west
44	randwick	NSW	-33,93177389	151,2428107	Sydney East
43	prospect	NSW	-33,79425278	150,9141768	Sydney North-west
41	oakdale	NSW	-34,05169965	150,4981819	Sydney South-west
40	newcastle	NSW	-32,93117889	151,7596294	Lower Hunter
30	liverpool	NSW	-33,93134917	150,9072993	Sydney South-west
26	kembla_grange	NSW	-34,47398434	150,81944	Illawarra
23	earlwood	NSW	-33,91617937	151,1357819	Sydney East
22	chullora	NSW	-33,89158612	151,0460603	Sydney East
20	campbelltown_west	NSW	-34,06665668	150,7955361	Sydney South-west
18	camden	NSW	-34,04172026	150,6901712	Sydney South-west
15	bringelly	NSW	-33,91765997	150,7619438	Sydney South-west

Table A.2.: Summery of air quality measurement stations (part 2).

32	macquarie_park	NSW	-33,7652905	151,1177491	Sydney East
462	dubbo	NSW	-32,2195	148,578	Central West LLS
463	kyalite	NSW	-35,0368	143,489	Murray LLS
467	ivanhoe	NSW	-33,0548	144,154	Western LLS
474	moree	NSW	-29,4897	149,847	North West LLS
465	hay	NSW	-34,54131	144,86448	Riverina LLS
466	hillston	NSW	-33,49151	145,52476	Western LLS
56	wagga_wagga_north	NSW	-35,104144	147,360398	South-west Slopes
479	walgett	NSW	-30,0359	148,123	North West LLS
482	white_cliffs	NSW	-30,8517	143,074	Western LLS
486	gunnedah_aqmu	NSW	-30,981876	150,260666	North West LLS
487	grafton	NSW	-29,620691	152,96331	Bushfire Monitoring
334	moe	VIC	-38,1864662	146,2583313	
341	melbourne_cbd	VIC	-37,807583	144,970001	
331	footscray	VIC	-37,80487767	144,8727377	
336	morwell_east	VIC	-38,22947539	146,424459	
337	morwell_south	VIC	-38,23953618	146,3873704	

B. Appendix for chapter 7

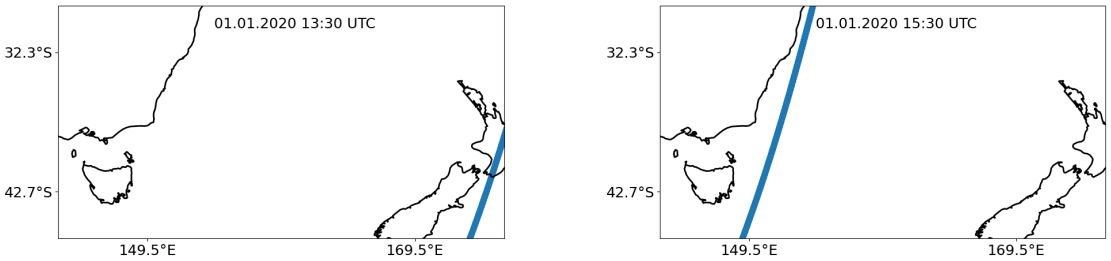

Figure B.1.: CALIPSO paths from left to right corresponding to the figures 7.5 and 7.6.

Artistic Interpretation

Lisa Muth, untitled, 2023-2024, oil on canvas, 120 cm×40 cm

C. Bibliography

Alonso-Blanco, E., A. I. Calvo, V. Pont, M. Mallet, R. Fraile, and A. Castro, 2014: Impact of biomass burning on aerosol size distribution, aerosol optical properties and associated radiative forcing. *Aerosol and Air Quality Research*, **14**, 708–724, doi:10.4209/aaqr.2013.05.0163.

Anderson, M. C., C. Hain, B. Wardlow, A. Pimstein, J. R. Mecikalski, and W. P. Kustas, 2011: Evaluation of drought indices based on thermal remote sensing of evapotranspiration over the continental United States. *Journal of Climate*, **24 (8)**, 2025–2044, doi:10.1175/2010JCLI3812.1.

Andreae, M. O. and P. Merlet, 2001: Emission of trace gases and aerosols from biomass burning. *Global biogeochemical cycles*, **15 (4)**, 955–966, doi:10.1029/2000GB001382.

Andreae, M. O., D. Rosenfeld, P. Artaxo, A. A. Costa, G. Frank, K. M. Longo, and M. A. F. d. Silva-Dias, 2004: Smoking rain clouds over the Amazon. *science*, **303 (5662)**, 1337–1342, doi:10.5194/acp-23-1019-2023.

Bechtold, P., N. Semane, P. Lopez, J.-P. Chaboureau, A. Beljaars, and N. Bormann, 2014: Representing equilibrium and nonequilibrium convection in large-scale models. *Journal of the Atmospheric Sciences*, **71 (2)**, 734–753, doi:10.1175/JAS-D-13-0163.1.

Bellouin, N. and H. Yu, 2022: Chapter 11 - Aerosol–radiation interactions. *Aerosols and Climate*, Carslaw, K. S., Ed., Elsevier, 445–487.

Bohren, C. F. and D. R. Huffman, 2008: *Absorption and scattering of light by small particles*. John Wiley & Sons.

Bond, T. C., G. Habib, and R. W. Bergstrom, 2006: Limitations in the enhancement of visible light absorption due to mixing state. *Journal of Geophysical Research Atmospheres*, **111**, D20 211, doi:10.1029/2006JD007315.

Borchers Arriagada, N., A. J. Palmer, D. M. Bowman, G. G. Morgan, B. B. Jalaludin, and F. H. Johnston, 2020: Unprecedented smoke-related health burden associated with the 2019–20 bushfires in eastern Australia. *Medical Journal of Australia*, **213 (6)**, 282–283, doi:10.5694/mja2.50545.

Bradstock, R. A., R. J. Williams, and A. M. Gill, 2012: *Flammable Australia: fire regimes, biodiversity and ecosystems in a changing world*. CSIRO publishing.

Briggs, G. A., 1975: Plume rise predictions. *Lectures on air pollution and environmental impact analyses*, Springer, 59–111.

Brito, J., L. V. Rizzo, W. T. Morgan, H. Coe, B. Johnson, J. Haywood, K. Longo, S. Freitas, M. O. Andreae, and P. Artaxo, 2014: Ground-based aerosol characterization during the South American Biomass Burning Analysis (SAMBBA) field experiment. *Atmospheric Chemistry and Physics*, **14**, 12 069–12 083, doi:10.5194/acp-14-12069-2014.

Brock, C. A., K. D. Froyd, M. Dollner, C. J. Williamson, G. Schill, D. M. Murphy, N. J. Wagner, A. Kupc, J. L. Jimenez, P. Campuzano-Jost, B. A. Nault, J. C. Schroder, D. A. Day, D. J. Price, B. Weinzierl, J. P. Schwarz, J. M. Katich, S. Wang, L. Zeng, R. Weber, J. DIbb, E. Scheuer, G. S. DIskin, J. P. DIgangi, T. Bui, J. M. Dean-Day, C. R. Thompson, J. Peischl, T. B. Ryerson, I. Bourgeois, B. C. Daube, R. Commane, and S. C. Wofsy, 2021: Ambient aerosol properties in the remote atmosphere from global-scale in situ measurements. *Atmospheric Chemistry and Physics*, **21**, 15 023–15 063, doi:10.5194/acp-21-15023-2021.

Brown, H., X. Liu, R. Pokhrel, S. Murphy, Z. Lu, R. Saleh, T. Mielonen, H. Kokkola, T. Bergman, G. Myhre, R. B. Skeie, D. Watson-Paris, P. Stier, B. Johnson, N. Bellouin, M. Schulz, V. Vakkari, J. P. Beukes, P. G. van Zyl, S. Liu, and D. Chand, 2021: Biomass burning aerosols in most climate models are too absorbing. *Nature Communications*, **12**, 277, doi:10.1038/s41467-020-20482-9.

Buchholz, R. R., L. K. Emmons, S. Tilmes, and The CESM2 Development Team, 2019: CESM2.1/CAM-chem Instantaneous Output for Boundary Conditions. UCAR/NCAR - Atmospheric Chemistry Observations and Modeling Laboratory. URL `https://doi.org/10.5065/NMP7-EP60`, accessed 12.02.2024.

Burbidge, A. A. and N. McKenzie, 1989: Patterns in the modern decline of Western Australia's vertebrate fauna: causes and conservation implications. *Biological conservation*, **50 (1-4)**, 143–198, doi:10.1016/0006-3207(89)90009-8.

Bureau of Meteorology, 2018: When bushfires make their own weather. URL `https://media.bom.gov.au/social/blog/1618/when-bushfires-make-their-own-weather/`, accessed 22.02.2024.

———, 2020a: Annual climate statement 2019. URL `http://www.bom.gov.au/climate/current/annual/aus/2019/#tabs=Overview`, accessed 12.02.2024.

———, 2020b: Bushfire weather. URL `http://www.bom.gov.au/weather-services/fire-weather-centre/bushfire-weather/index.shtml`, accessed 12.02.2024.

———, 2020c: Climate classification maps. URL `//http://www.bom.gov.au/climate/maps/averages/climate-classification/?maptype=kpn`, accessed 12.02.2024.

———, 2020d: Climate Data Services. URL https://reg.bom.gov.au/climate/data-services/, accessed 12.02.2024.

———, 2022: MSLP Analysis (Manual) Australian Region. URL http://www.bom.gov.au/cgi-bin/charts/charts.browse.pl?&syear=2019&smonth=12&sday=26&eyear=2022&emonth=01&eday=14&pdep=14&pstart=28&idcode=IDX0102&list=LIST, accessed 12.02.2024.

Cahill, C. F., T. A. Cahill, and K. D. Perry, 2008: The size- and time-resolved composition of aerosols from a sub-Arctic boreal forest prescribed burn. *Atmospheric Environment*, **42**, 7553–7559, doi:10.1016/j.atmosenv.2008.04.034.

Carr, J. L., D. L. Wu, M. A. Kelly, and J. Gong, 2018: MISR-GOES 3D Winds: Implications for Future LEO-GEO and LEO-LEO Winds. *Remote Sensing*, **10 (12)**, 1885, doi:10.3390/rs10121885.

Carr, J. L., D. L. Wu, J. Daniels, M. D. Friberg, W. Bresky, and H. Madani, 2020: GEO–GEO stereo-tracking of atmospheric motion vectors (AMVs) from the geostationary ring. *Remote Sensing*, **12 (22)**, 3779, doi:10.3390/rs12223779.

Carr, J. L., D. L. Wu, R. E. Wolfe, H. Madani, G. Lin, and B. Tan, 2019: Joint 3D-wind retrievals with stereoscopic views from MODIS and GOES. *Remote Sensing*, **11 (18)**, 2100, doi:10.3390/rs11182100.

Centre for Air pollution, energy and health Research, 2021: National Air Pollution Monitoring Database, derived from regulatory monitor data from NSW DPIE, Vic EPA, Qld DES, SA EPA, WA DEWR, Tas EPA, NT EPA, and ACT Health. Downloaded from the Centre for Air pollution, energy and health Research [accessed 2023-12-05].

Chand, D., R. Wood, T. Anderson, S. Satheesh, and R. Charlson, 2009: Satellite-derived direct radiative effect of aerosols dependent on cloud cover. *Nature Geoscience*, **2 (3)**, 181–184, doi:10.1038/ngeo437.

Chang, D. Y., J. Yoon, J. Lelieveld, S. K. Park, S. S. Yum, J. Kim, and S. Jeong, 2021: Direct radiative forcing of biomass burning aerosols from the extensive Australian wildfires in 2019–2020. *Environmental Research Letters*, **16 (4)**, 044 041, doi:10.1088/1748-9326/abecfe.

Chou, C., P. Formenti, M. Maille, P. Ausset, G. Helas, M. Harrison, and S. Osborne, 2008: Size distribution, shape, and composition of mineral dust aerosols collected during the African Monsoon Multidisciplinary Analysis Special Observation Period 0: Dust and Biomass-Burning Experiment field campaign in Niger, January 2006. *Journal of Geophysical Research Atmospheres*, **113**, 1–17, doi:10.1029/2008JD009897.

Clark, J. M. A. C. J., T. L. and D. R. Packham, 1996: A Coupled Atmosphere-Fire Model: Convective Feedback on Fire-Line Dynamics. *Bulletin of the American Meteorological Society*, **35**, 875–901, doi:10.1175/1520-0450(1996)035<0875:ACAMCF>2.0.CO;2.

Clark, T. L., J. Coen, and D. Latham, 2004: Description of a coupled atmosphere-fire model. *International Journal of Wildland Fire*, **13**, 49–63, doi:10.1071/WF03043.

Clements, C. B., S. Zhong, S. Goodrick, J. Li, B. E. Potter, X. Bian, W. E. Heilman, J. J. Charney, R. Perna, M. Jang, et al., 2007: Observing the Dynamics of Wildland Grass Fires: FireFlux – A Field ValidationExperiment. *Bulletin of the American Meteorological Society*, **88**, 1369–1382, doi:10.1175/BAMS-88-9-1369.

Coen, J. L., 2005: Simulation of the Big Elk Fire using coupled atmosphere-fire modeling. *International Journal of Wildland Fire*, **14**, 49–59, doi:10.1071/WF04047.

Colarco, P., M. Schoeberl, B. Doddridge, L. Marufu, O. Torres, and E. Welton, 2004: Transport of smoke from Canadian forest fires to the surface near Washington, DC: Injection height, entrainment, and optical properties. *Journal of Geophysical Research: Atmospheres*, **109 (D6)**, doi:10.1029/2003JD004248.

Copernicus Atmosphere Monitoring Service, 2021: CAMS global biomass burning emissions based on fire radiative power (GFAS). URL `https://ads.atmosphere.copernicus.eu/cdsapp#!/dataset/cams-global-fire-emissions-gfas?tab=form`, accessed 12.02.2024.

Cubison, M., A. Ortega, P. Hayes, D. Farmer, D. Day, M. Lechner, W. Brune, E. Apel, G. Diskin, J. Fisher, et al., 2011: Effects of aging on organic aerosol from open biomass burning smoke in aircraft and laboratory studies. *Atmospheric Chemistry and Physics*, **11 (23)**, 12 049–12 064, doi:10.5194/acp-11-12049-2011.

Cunningham, P. and M. J. Reeder, 2009: Severe convective storms initiated by intense wildfires: Numerical simulations of pyro-convection and pyro-tornadogenesis. *Geophysical Research Letters*, **36 (12)**, L12 812, doi:10.1029/2009GL039262.

Davey, S. M. and A. Sarre, 2020: Editorial: the 2019/20 Black Summer bushfires. *Australian Forestry*, **83 (2)**, 47–51, doi:10.1080/00049158.2020.1769899.

Deb, P., H. Moradkhani, P. Abbaszadeh, A. S. Kiem, J. Engström, D. Keellings, and A. Sharma, 2020: Causes of the Widespread 2019–2020 Australian Bushfire Season. *Earth's Future*, **8 (11)**, e2020EF001 671, doi:10.1029/2020EF001671.

DeCarlo, P., I. Ulbrich, J. Crounse, B. de Foy, E. Dunlea, A. Aiken, D. Knapp, A. Weinheimer, T. Campos, P. Wennberg, et al., 2010: Investigation of the sources and processing of organic aerosol over the Central Mexican Plateau from aircraft measurements during MILAGRO. *Atmospheric Chemistry and Physics*, **10 (12)**, 5257–5280, doi:10.5194/acp-10-5257-2010.

Denjean, C., J. Brito, Q. Libois, M. Mallet, T. Bourrianne, F. Burnet, R. Dupuy, C. Flamant, and P. Knippertz, 2020: Unexpected Biomass Burning Aerosol Absorption Enhancement Explained by Black Carbon Mixing State. *Geophysical Research Letters*, **47**, 1–11, doi:10.1029/2020GL089055.

Dirksen, R. J., K. Folkert Boersma, J. de Laat, P. Stammes, G. R. van der Werf, M. Val Martin, and H. M. Kelder, 2009: An aerosol boomerang: Rapid around-the-world transport of smoke from the December 2006 Australian forest fires observed from space. *Journal of Geophysical Research: Atmospheres*, **114 (D21)**, D21 201, doi:10.1029/2009JD012360.

Duane, A., M. Castellnou, and L. Brotons, 2021: Towards a comprehensive look at global drivers of novel extreme wildfire events. *Climatic Change*, **165 (3-4)**, 43, doi:10.1007/s10584-021-03066-4.

Emmons, L. K., R. H. Schwantes, J. J. Orlando, G. Tyndall, D. Kinnison, J.-F. Lamarque, D. Marsh, M. J. Mills, S. Tilmes, C. Bardeen, R. R. Buchholz, A. Conley, A. Gettelman, R. Garcia, I. Simpson, D. R. Blake, S. Meinardi, and G. Pétron, 2020: The Chemistry Mechanism in the Community Earth System Model Version 2 (CESM2). *Journal of Advances in Modeling Earth Systems*, **12 (4)**, e2019MS001 882, doi:10.1029/2019MS001882.

Feng, Y., Q. Liu, Y. Qu, and S. Liang, 2015: Estimation of the ocean water albedo from remote sensing and meteorological reanalysis data. *IEEE Transactions on Geoscience and Remote Sensing*, **54 (2)**, 850–868, doi:10.1109/TGRS.2015.2468054.

Fidelis, A., 2020: Is fire always the "bad guy"? *Flora*, **268**, 151 611, doi:10.1016/j.flora.2020.151611.

Filippi, J. B., X. Pialat, and C. B. Clements, 2013: Assessment of ForeFire/Meso-NH for wildland fire/atmosphere coupled simulation of the FireFlux experiment. *Proceedings of the Combustion Institute*, **34**, 2633–2640, doi:10.1016/j.proci.2012.07.022.

Fiorucci, P., F. Gaetani, A. Lanorte, and R. Lasaponara, 2007: Dynamic fire danger mapping from satellite imagery and meteorological forecast data. *Earth Interactions*, **11 (7)**, 1–17, doi:10.1175/EI199.1.

Fisher, R., T. Vigilante, C. Yates, and J. Russell-Smith, 2003: Patterns of landscape fire and predicted vegetation response in the North Kimberley region of Western Australia. *International Journal of Wildland Fire*, **12 (4)**, 369–379, doi:10.1071/WF03021.

Fordyce, I., D. Eamus, G. A. Duff, and R. J. Williams, 1997: The role of seedling age and size in the recovery of Allosyncarpia ternata following fire. *Australian Journal of Ecology*, **22 (3)**, 262–269, doi:10.1111/j.1442-9993.1997.tb00671.x.

Fountoukis, C. and A. Nenes, 2007: ISORROPIA II: a computationally efficient thermodynamic equilibrium model for K+–Ca 2+–Mg 2+–NH 4+–Na+–SO 4 2—NO 3—Cl—H 2 O aerosols. *Atmospheric Chemistry and Physics*, **7 (17)**, 4639–4659, doi:10.5194/acp-7-4639-2007.

Fox-Hughes, P., 2023: Synoptic and Mesoscale Aspects of Exceptional Fire Weather during the New Year Period 2019–20 in Southeastern New South Wales, Australia. *Weather and Forecasting*, **38 (11)**, 2237 – 2252, doi:10.1175/WAF-D-23-0007.1.

Franklin, D. C., 1999: Evidence of disarray amongst granivorous bird assemblages in the savannas of northern Australia, a region of sparse human settlement. *Biological Conservation*, **90 (1)**, 53–68, doi:10.1016/S0006-3207(99)00010-5.

Freeborn, P. H., M. J. Wooster, W. M. Hao, C. A. Ryan, B. L. Nordgren, S. P. Baker, and C. Ichoku, 2008: Relationships between energy release, fuel mass loss, and trace gas and aerosol emissions during laboratory biomass fires. *Journal of Geophysical Research: Atmospheres*, **113 (D1)**, D01 301, doi:10.1029/2007JD008679.

Freitas, S. R., K. M. Longo, and M. O. Andreae, 2006: Impact of including the plume rise of vegetation fires in numerical simulations of associated atmospheric pollutants. *Geophysical Research Letters*, **33**, 1–5, doi:10.1029/2006GL026608.

Freitas, S. R., K. M. Longo, R. Chatfield, D. Latham, M. A. S. Dias, M. O. Andreae, E. Prins, J. C. Santos, R. Gielow, and J. A. Carvalho, 2007: Including the sub-grid scale plume rise of vegetation fires in low resolution atmospheric transport models. *Atmospheric Chemistry and Physics*, **7**, 3385–3398, doi:10.5194/acp-7-3385-2007.

Freitas, S. R., K. M. Longo, J. Trentmann, and D. Latham, 2010: Technical Note: Sensitivity of 1-D smoke plume rise models to the inclusion of environmental wind drag. *Atmospheric Chemistry and Physics*, **10**, 585–594, doi:10.5194/acp-10-585-2010.

Friedman, B., H. Herich, L. Kammermann, D. S. Gross, A. Arneth, T. Holst, and D. J. Cziczo, 2009: Subarctic atmospheric aerosol composition: 1. Ambient aerosol characterization. *Journal of Geophysical Research Atmospheres*, **114**, 1–11, doi:10.1029/2009JD011772.

Fromm, M., R. McRae, J. Sharples, and G. Kablick Iii, 2012: Pyrocumulonimbus pair in Wollemi and Blue Mountains National Parks, 22 November 2006. *Australian Meteorological and Oceanographic Journal*, **62 (3)**, 117, doi:10.22499/2.6203.001.

Fromm, M., A. Tupper, D. Rosenfeld, R. Servranckx, and R. McRae, 2006: Violent pyro-convective storm devastates Australia's capital and pollutes the stratosphere. *Geophysical Research Letters*, **33 (5)**, L05 815, doi:10.1029/2005GL025161.

Fromm, M. D. and R. Servranckx, 2003: Transport of forest fire smoke above the tropopause by supercell convection. *Geophysical Research Letters*, **30 (10)**, 1542, doi:10.1029/2002GL016820.

Fuzzi, S., S. Decesari, M. C. Facchini, F. Cavalli, L. Emblico, M. Mircea, M. O. Andreae, I. Trebs, A. Hoffer, P. Guyon, P. Artaxo, L. V. Rizzo, L. L. Lara, T. Pauliquevis, W. Maenhaut, N. Raes, X. Chi, O. L. Mayol-Bracero, L. L. Soto-García, M. Claeys, I. Kourtchev, J. Rissler, E. Swietlicki, E. Tagliavini, G. Schkolnik, A. H. Falkovich, Y. Rudich, G. Fisch, and L. V. Gatti, 2007: Overview of the

inorganic and organic composition of size-segregated aerosol in Rondônia, Brazil, from the biomass-burning period to the onset of the wet season. *Journal of Geophysical Research Atmospheres*, **112**, D01 201, doi:10.1029/2005JD006741.

Gassmann, A. and H. J. Herzog, 2008: Towards a consistent numerical compressible non-hydrostatic model using generalized Hamiltonian tools. *Quarterly Journal of the Royal Meteorological Society*, **134**, 1597–1613, doi:10.1002/qj.297.

Generoso, S., I. Bey, J.-L. Attié, and F.-M. Bréon, 2007: A satellite-and model-based assessment of the 2003 Russian fires: Impact on the Arctic region. *Journal of Geophysical Research: Atmospheres*, **112 (D15)**, doi:10.1029/2006JD008344.

Giglio, L., 2007: Characterization of the tropical diurnal fire cycle using VIRS and MODIS observations. *Remote Sensing of Environment*, **108 (4)**, 407–421, doi:10.1016/j.rse.2006.11.018.

Giorgetta, M. A., R. Brokopf, T. Crueger, M. Esch, S. Fiedler, J. Helmert, C. Hohenegger, L. Kornblueh, M. Köhler, E. Manzini, et al., 2018: ICON-A, the atmosphere component of the ICON earth system model: I. Model description. *Journal of Advances in Modeling Earth Systems*, **10 (7)**, 1613–1637, doi:10.1029/2017MS001233.

Gonzi, S. and P. I. Palmer, 2010: Vertical transport of surface fire emissions observed from space. *Journal of Geophysical Research: Atmospheres*, **115 (D2)**, D02 306, doi:10.1029/2009JD012053.

Gott, B., 2005: Aboriginal Fire Management in South-Eastern Australia: Aims and Frequency. *Journal of Biogeography*, **32 (7)**, 1203–1208, doi:10.1111/j.1365-2699.2004.01233.x.

Grabowski, W. W. and H. Morrison, 2021: Supersaturation, buoyancy, and deep convection dynamics. *Atmospheric Chemistry and Physics*, **21 (18)**, 13 997–14 018, doi:10.5194/acp-21-13997-2021.

Heil, A., J. Kaiser, G. van der Werf, M. Wooster, M. Schultz, and H. van der Gon, 2010: Assessment of the real-time fire emissions (GFASv0) by MACC. URL `https://www.ecmwf.int/node/9842`.

Heinold, B., H. Baars, B. Barja, M. Christensen, A. Kubin, K. Ohneiser, K. Schepanski, N. Schutgens, F. Senf, R. Schrödner, D. Villanueva, and I. Tegen, 2022: Important role of stratospheric injection height for the distribution and radiative forcing of smoke aerosol from the 2019–2020 Australian wildfires. *Atmospheric Chemistry and Physics*, **22 (15)**, 9969–9985, doi:10.5194/acp-22-9969-2022.

Hines, F., F. Hines, K. G. Tolhurst, A. A. Wilson, and G. J. McCarthy, 2010: *Overall fuel hazard assessment guide*. East Melbourne, Victoria, Australia: Victorian Government, Department of Sustainability and Environment.

Hirsch, E. and I. Koren, 2021: Record-breaking aerosol levels explained by smoke injection into the stratosphere. *Science*, **371 (6535)**, 1269–1274, doi:10.1126/science.abe1415.

Hodshire, A. L., Q. Bian, E. Ramnarine, C. R. Lonsdale, M. J. Alvarado, S. M. Kreidenweis, S. H. Jathar, and J. R. Pierce, 2019: More Than Emissions and Chemistry: Fire Size, Dilution, and Background Aerosol Also Greatly Influence Near-Field Biomass Burning Aerosol Aging. *Journal of Geophysical Research: Atmospheres*, **124**, 5589–5611, doi:10.1029/2018JD029674.

Hodshire, A. L., E. Ramnarine, A. Akherati, M. L. Alvarado, D. K. Farmer, S. H. Jathar, S. M. Kreidenweis, C. R. Lonsdale, T. B. Onasch, S. R. Springston, J. Wang, Y. Wang, L. I. Kleinman, A. J. Sedlacek, and J. R. Pierce, 2021: Dilution impacts on smoke aging: Evidence in Biomass Burning Observation Project (BBOP) data. *Atmospheric Chemistry and Physics*, **21**, 6839–6855, doi:10.5194/acp-21-6839-2021.

Hogan, R. J. and A. Bozzo, 2018: A Flexible and Efficient Radiation Scheme for the ECMWF Model. *Journal of Advances in Modeling Earth Systems*, **10 (8)**, 1990–2008, doi:10.1029/2018MS001364.

Hoose, C. and O. Möhler, 2012: Heterogeneous ice nucleation on atmospheric aerosols: a review of results from laboratory experiments. *Atmospheric Chemistry and Physics*, **12 (20)**, 9817–9854, doi:10.5194/acp-12-9817-2012.

Hoshyaripour, G., V. Bachmann, J. Förstner, A. Steiner, H. Vogel, F. Wagner, C. Walter, and B. Vogel, 2019: Effects of particle nonsphericity on dust optical properties in a forecast system: Implications for model-observation comparison. *Journal of Geophysical Research: Atmospheres*, **124 (13)**, 7164–7178, doi:10.1029/2018JD030228.

Hosseini, S., Q. Li, D. Cocker, D. Weise, A. Miller, M. Shrivastava, J. W. Miller, S. Mahalingam, M. Princevac, and H. Jung, 2010: Particle size distributions from laboratory-scale biomass fires using fast response instruments. *Atmospheric Chemistry and Physics*, **10**, 8065–8076, doi:10.5194/acp-10-8065-2010.

Hyer, E. J., D. J. Allen, and E. S. Kasischke, 2007: Examining injection properties of boreal forest fires using surface and satellite measurements of CO transport. *Journal of Geophysical Research: Atmospheres*, **112 (D18)**, D18 307, doi:10.1029/2006JD008232.

Jacob, D. J., 1986: Chemistry of OH in remote clouds and its role in the production of formic acid and peroxymonosulfate. *Journal of Geophysical Research: Atmospheres*, **91 (D9)**, 9807–9826, doi:10.1029/JD091iD09p09807.

Janhäll, S., M. O. Andreae, and U. Pöschl, 2010: Biomass burning aerosol emissions from vegetation fires: Particle number and mass emission factors and size distributions. *Atmospheric Chemistry and Physics*, **10**, 1427–1439, doi:10.5194/acp-10-1427-2010.

Justice, C. O., L. Giglio, D. Roy, L. Boschetti, I. Csiszar, D. Davies, S. Korontzi, W. Schroeder, K. O'Neal, and J. Morisette, 2011: MODIS-derived global fire products. *Land Remote Sensing and*

Global Environmental Change: NASA's Earth Observing System and the Science of ASTER and MODIS, 661–679, doi:10.1007/978-1-4419-6749-$7_2$9.

Kablick III, G. P., D. R. Allen, M. D. Fromm, and G. E. Nedoluha, 2020: Australian PyroCb Smoke Generates Synoptic-Scale Stratospheric Anticyclones. *Geophysical Research Letters*, **47 (13)**, e2020GL088 101, doi:10.1029/2020GL088101.

Kahn, R. A., Y. Chen, D. L. Nelson, F.-Y. Leung, Q. Li, D. J. Diner, and J. A. Logan, 2008: Wildfire smoke injection heights: Two perspectives from space. *Geophysical Research Letters*, **35 (4)**, L04 809, doi:10.1029/2007GL032165.

Kahn, R. A., W.-H. Li, C. Moroney, D. J. Diner, J. V. Martonchik, and E. Fishbein, 2007: Aerosol source plume physical characteristics from space-based multiangle imaging. *Journal of Geophysical Research: Atmospheres*, **112 (D11)**, D11 205, doi:10.1029/2006JD007647.

Kaiser, J., J. Flemming, M. Schultz, M. Suttie, and M. Wooster, 2009: The MACC Global Fire Assimilation System: First Emission Products (GFASv0). URL `https://www.ecmwf.int/node/10373`.

Kaiser, J. C., J. Hendricks, M. Righi, N. Riemer, R. A. Zaveri, S. Metzger, and V. Aquila, 2014: The MESSy aerosol submodel MADE3 (v2.0b): description and a box model test. *Geoscientific Model Development*, **7 (3)**, 1137–1157, doi:10.5194/gmd-7-1137-2014.

Kaiser, J. W., A. Heil, M. O. Andreae, A. Benedetti, N. Chubarova, L. Jones, J. J. Morcrette, M. Razinger, M. G. Schultz, M. Suttie, and G. R. V. D. Werf, 2012: Biomass burning emissions estimated with a global fire assimilation system based on observed fire radiative power. *Biogeosciences*, **9**, 527–554, doi:10.5194/bg-9-527-2012.

Ke, Z., Y. Wang, Y. Zou, Y. Song, and Y. Liu, 2021: Global Wildfire Plume-Rise Data Set and Parameterizations for Climate Model Applications. *Journal of Geophysical Research: Atmospheres*, **126 (6)**, e2020JD033 085, doi:10.1029/2020JD033085.

Kerminen, V.-M. and A. S. Wexler, 1995: The interdependence of aerosol processes and mixing in point source plumes. *Atmospheric Environment*, **29 (3)**, 361–375, doi:10.1016/1352-2310(94)00262-J.

Kessler, E., 1969: *On the distribution and continuity of water substance in atmospheric circulations*, American Meteorological Society, 1–84.

Khalizov, A. F., H. Xue, L. Wang, J. Zheng, and R. Zhang, 2009: Enhanced light absorption and scattering by carbon soot aerosol internally mixed with sulfuric acid. *The Journal of Physical Chemistry A*, **113 (6)**, 1066–1074, doi:10.1021/jp807531n.

Khaykin, S., B. Legras, S. Bucci, P. Sellitto, L. Isaksen, F. Tencé, S. Bekki, A. Bourassa, L. Rieger, D. Zawada, et al., 2020: The 2019/20 Australian wildfires generated a persistent smoke-charged vortex rising

up to 35 km altitude. *Communications Earth & Environment*, **1 (1)**, 22, doi:10.1038/s43247-020-00022-5.

Kiefer, C. M., C. B. Clements, and B. E. Potter, 2012: Application of a mini unmanned aircraft system for in situ monitoring of fire plume thermodynamic properties. *Journal of Atmospheric and Oceanic Technology*, **29**, 309–315, doi:10.1175/JTECH-D-11-00112.1.

Kiefer, M. T., W. E. Heilman, S. Zhong, J. J. Charney, and X. Bian, 2016: A study of the influence of forest gaps on fire-atmosphere interactions. *Atmospheric Chemistry and Physics*, **16**, 8499–8509, doi:10.5194/acp-16-8499-2016.

Kiefer, M. T., W. E. Heilman, S. Zhong, J. J. Charney, X. Bian, N. S. Skowronski, J. L. Hom, K. L. Clark, M. Patterson, and M. R. Gallagher, 2014: Multiscale simulation of a prescribed fire event in the New Jersey Pine Barrens using ARPS-CANOPY. *Journal of Applied Meteorology and Climatology*, **53**, 793–812, doi:10.1175/JAMC-D-13-0131.1.

Kiefer, M. T., M. D. Parker, and J. J. Charney, 2010: Regimes of dry convection above wildfires: Sensitivity to fire line details. *Journal of the Atmospheric Sciences*, **67**, 611–632, doi:10.1175/2009JAS3226.1, fire -atmo domain größe 20 km.

Kiefer, M. T., S. Zhong, W. E. Heilman, J. J. Charney, and X. Bian, 2018: A Numerical Study of Atmospheric Perturbations Induced by Heat From a Wildland Fire: Sensitivity to Vertical Canopy Structure and Heat Source Strength. *Journal of Geophysical Research: Atmospheres*, **123**, 2555–2572, doi:10.1002/2017JD027904.

Kleinman, L. I., A. J. Sedlacek, K. Adachi, P. R. Buseck, S. Collier, M. K. Dubey, A. L. Hodshire, E. Lewis, T. B. Onasch, J. R. Pierce, J. Shilling, S. R. Springston, J. Wang, Q. Zhang, S. Zhou, and R. J. Yokelson, 2020: Rapid evolution of aerosol particles and their optical properties downwind of wildfires in the western US. *Atmospheric Chemistry and Physics*, **20**, 13 319–13 341, doi:10.5194/acp-20-13319-2020.

Kochanski, A. K., A. Fournier, and J. Mandel, 2018: Experimental design of a prescribed burn instrumentation. *Atmosphere*, **9**, doi:10.3390/atmos9080296.

Kochanski, A. K., M. A. Jenkins, J. Mandel, J. D. Beezley, C. B. Clements, and S. Krueger, 2013: Evaluation of WRF-SFIRE performance with field observations from the FireFlux experiment. *Geoscientific Model Development*, **6**, 1109–1126, doi:10.5194/gmd-6-1109-2013.

Kochanski, A. K., M. A. Jenkins, K. Yedinak, J. Mandel, J. Beezley, and B. Lamb, 2016: Toward an integrated system for fire, smoke and air quality simulations. *International Journal of Wildland Fire*, **25**, 534–546, doi:10.1071/WF14074.

Kondratyev, K., 1969: *Radiation in the Atmosphere*, Academic Press, International Geophysics, Vol. 12, chap. 7 Albedo of the Underlying Surface and Clouds, 411–452.

Koppmann, R., K. V. Czapiewski, and J. S. Reid, 2005: A review of biomass burning emissions, part I: gaseous emissions of carbon monoxide, methane, volatile organic compounds, and nitrogen containing compounds. *Atmos. Chem. Phys. Discuss*, **5**, 10 455–10 516, doi:10.5194/acpd-5-10455-2005.

Kumar, A., R. B. Pierce, R. Ahmadov, G. Pereira, S. Freitas, G. Grell, C. Schmidt, A. Lenzen, J. P. Schwarz, A. E. Perring, J. M. Katich, J. Hair, J. L. Jimenez, P. Campuzano-Jost, and H. Guo, 2022: Simulating wildfire emissions and plume rise using geostationary satellite fire radiative power measurements: A case study of the 2019 Williams Flats fire. *Atmospheric Chemistry and Physics*, **22**, 10 195–10 219, doi:10.5194/acp-22-10195-2022.

Labonne, M., F.-M. Bréon, and F. Chevallier, 2007: Injection height of biomass burning aerosols as seen from a spaceborne lidar. *Geophysical Research Letters*, **34 (11)**, L11 806, doi:10.1029/2007GL029311.

Lack, D. A., J. M. Langridge, R. Bahreini, C. D. Cappa, A. M. Middlebrook, and J. P. Schwarz, 2012: Brown carbon and internal mixing in biomass burning particles. *Proceedings of the National Academy of Sciences*, **109 (37)**, 14 802–14 807, doi:10.1073/pnas.1206575109.

Lamarque, J.-F., D. Edwards, L. Emmons, J. Gille, O. Wilhelmi, C. Gerbig, D. Prevedel, M. Deeter, J. Warner, D. Ziskin, et al., 2003: Identification of CO plumes from MOPITT data: Application to the August 2000 Idaho-Montana forest fires. *Geophysical Research Letters*, **30 (13)**, doi:10.1029/2003GL017503.

Latham, D. J., 1994: *PLUMP, a Plume Predictor and Cloud Model for Fire Managers*, Vol. 314. US Department of Agriculture, Forest Service, Intermountain Research Station.

Lattimer, B. Y., 2019: *Heat Transfer from Fires*, 1–10. Springer International Publishing, doi:10.1007/978-3-319-51727-$8_3$8 – 1.

Lavoué, D., C. Liousse, H. Cachier, B. J. Stocks, and J. G. Goldammer, 2000: Modeling of carbonaceous particles emitted by boreal and temperate wildfires at northern latitudes. *Journal of Geophysical Research: Atmospheres*, **105 (D22)**, 26 871–26 890, doi:10.1029/2000JD900180.

Lefevre, G., J. Yon, F. Liu, and A. Coppalle, 2018: Spectrally resolved light extinction enhancement of coated soot particles. *Atmospheric Environment*, **186**, 89–101, doi:10.1016/j.atmosenv.2018.05.029.

Leung, F.-Y. T., J. A. Logan, R. Park, E. Hyer, E. Kasischke, D. Streets, and L. Yurganov, 2007: Impacts of enhanced biomass burning in the boreal forests in 1998 on tropospheric chemistry and the sensitivity of model results to the injection height of emissions. *Journal of Geophysical Research: Atmospheres*, **112 (D10)**, D10 313, doi:10.1029/2006JD008132.

Levin, E. J., G. R. McMeeking, C. M. Carrico, L. E. Mack, S. M. Kreidenweis, C. E. Wold, H. Moosmüller, W. P. Arnott, W. M. Hao, J. L. Collett, and W. C. Malm, 2010: Biomass burning smoke aerosol properties

measured during Fire Laboratory at Missoula Experiments (FLAME). *Journal of Geophysical Research Atmospheres*, **115**, 1–15, doi:10.1029/2009JD013601.

Levin, N., M. Yebra, and S. Phinn, 2021: Unveiling the Factors Responsible for Australia's Black Summer Fires of 2019/2020. *Fire*, **4 (3)**, 58, doi:10.3390/fire4030058.

Levy, R. C., S. Mattoo, L. A. Munchak, L. A. Remer, A. M. Sayer, F. Patadia, and N. C. Hsu, 2013: The Collection 6 MODIS aerosol products over land and ocean. *Atmospheric Measurement Techniques*, **6 (11)**, 2989–3034, doi:10.5194/amt-6-2989-2013.

Li, F., X. Zhang, and S. Kondragunta, 2021a: Highly anomalous fire emissions from the 2019–2020 Australian bushfires. *Environmental Research Communications*, **3 (10)**, 105 005, doi:10.1088/2515-7620/ac2e6f.

Li, M., F. Shen, and X. Sun, 2021b: 2019–2020 Australian bushfire air particulate pollution and impact on the South Pacific Ocean. *Scientific Reports*, **11**, 12 288, doi:10.1038/s41598-021-91547-y.

Linn, R., J. Reisner, J. J. Colman, and J. Winterkamp, 2002: Studying wildfire behavior using FIRETEC. *International Journal of Wildland Fire*, **11**, 233–246, doi:10.1071/wf02007.

Liu, L., Y. Cheng, S. Wang, C. Wei, M. L. Pöhlker, C. Pöhlker, P. Artaxo, M. Shrivastava, M. O. Andreae, U. Pöschl, and H. Su, 2020: Impact of biomass burning aerosols on radiation, clouds, and precipitation over the Amazon: relative importance of aerosol–cloud and aerosol–radiation interactions. *Atmospheric Chemistry and Physics*, **20 (21)**, 13 283–13 301, doi:10.5194/acp-20-13283-2020.

Liu, Y., W. E. Heilman, B. E. Potter, C. B. Clements, W. A. Jackson, N. H. French, S. L. Goodrick, A. K. Kochanski, N. K. Larkin, P. W. Lahm, et al., 2022: *Smoke Plume Dynamics*. Wildland Fire Smoke in the United States, 83-119 pp.

Lucas, C., 2005: Fire climates of australia: Past, present and future. *Proceedings, 6th Symposium on Fire and Forest Meteorology, Canmore, Alberta, Canada*, 25–27.

Luderer, G., J. Trentmann, T. Winterrath, C. Textor, M. Herzog, H. Graf, and M. Andreae, 2006: Modeling of biomass smoke injection into the lower stratosphere by a large forest fire (Part II): sensitivity studies. *Atmospheric Chemistry and Physics*, **6 (12)**, 5261–5277, doi:10.5194/acp-6-5261-2006.

Luderer, G. G., 2007: *Modeling of deep-convective transport of forest fire smoke into the upper troposphere and lower stratosphere*. IMPRS.

Lyapustin, A., 2023: MODIS/Terra+Aqua Surface Reflectance (Bands 8-12) from MAIAC, Daily L3 Global 0.05Deg CMG V061. URL `https://doi.org/10.5067/MODIS/MCD19A1CMGO.061`, last access 04.03.2024.

Lyapustin, A., J. Martonchik, Y. Wang, I. Laszlo, and S. Korkin, 2011a: Multiangle implementation of atmospheric correction (MAIAC): 1. Radiative transfer basis and look-up tables. *Journal of Geophysical Research: Atmospheres*, **116 (D3)**, D03 210, doi:10.1029/2010JD014985.

Lyapustin, A., Y. Wang, S. Korkin, and D. Huang, 2018: MODIS collection 6 MAIAC algorithm. *Atmospheric Measurement Techniques*, **11 (10)**, 5741–5765, doi:10.5194/amt-11-5741-2018.

Lyapustin, A., Y. Wang, I. Laszlo, R. Kahn, S. Korkin, L. Remer, R. Levy, and J. Reid, 2011b: Multiangle implementation of atmospheric correction (MAIAC): 2. Aerosol algorithm. *Journal of Geophysical Research: Atmospheres*, **116 (D3)**, D03 211, doi:10.1029/2010JD014985.

Lyapustin, A. I., Y. Wang, I. Laszlo, T. Hilker, F. G. Hall, P. J. Sellers, C. J. Tucker, and S. V. Korkin, 2012: Multi-angle implementation of atmospheric correction for MODIS (MAIAC): 3. Atmospheric correction. *Remote Sensing of Environment*, **127**, 385–393, doi:10.1016/j.rse.2012.09.002.

Mandel, J., J. D. Beezley, and A. K. Kochanski, 2011: Coupled atmosphere-wildland fire modeling with WRF 3.3 and SFIRE 2011. *Geoscientific Model Development*, **4**, 591–610, doi:10.5194/gmd-4-591-2011.

Marlon, J. R., P. J. Bartlein, C. Carcaillet, D. G. Gavin, S. P. Harrison, P. E. Higuera, F. Joos, M. J. Power, and I. C. Prentice, 2008: Climate and human influences on global biomass burning over the past two millennia. *Nature Geoscience*, **1**, 697–702, doi:10.1038/ngeo468.

Marutzky, R., 1991: Erkenntnisse zur Schadstoffbildung bei der Verbrennung von Holz und Spanplatten. *WKI-Bericht Nr. 26. Braunschweig, Germany*.

Mätzler, C., 2002: MATLAB functions for Mie scattering and absorption, version 2. *IAP Res Rep, 8*, 1–24.

McCarter, R. J. and A. Broido, 1965: *Radiative and convective energy from wood crib fires*. Pyrodinamics, 65-85 pp.

McClure, C. D., C. Y. Lim, D. H. Hagan, J. H. Kroll, and C. D. Cappa, 2020: Biomass-burning-derived particles from a wide variety of fuels - Part 1: Properties of primary particles. *Atmospheric Chemistry and Physics*, **20**, 1531–1547, doi:10.5194/acp-20-1531-2020.

McKenzie, N., A. Burbidge, A. Baynes, R. Brereton, C. Dickman, G. Gordon, L. Gibson, P. Menkhorst, A. Robinson, M. Williams, et al., 2007: Analysis of factors implicated in the recent decline of Australia's mammal fauna. *Journal of Biogeography*, **34 (4)**, 597–611, doi:10.1111/j.1365-2699.2006.01639.x.

Mlawer, E. J., S. J. Taubman, P. D. Brown, M. J. Iacono, and S. A. Clough, 1997: Radiative transfer for inhomogeneous atmospheres: RRTM, a validated correlated-k model for the longwave. *Journal of Geophysical Research: Atmospheres*, **102 (D14)**, 16 663–16 682, doi:10.1029/97JD00237.

MODIS Characterization Support Team, 2017: MODIS 500m Calbrated Radiance Product. URL http://dx.doi.org/10.5067/MODIS/MOD02HKM.061, last access 04.03.2024.

Morandini, F., Y. Perez-Ramirez, V. Tihay, P. A. Santoni, and T. Barboni, 2013: Radiant, convective and heat release characterization of vegetation fire. *International Journal of Thermal Sciences*, **70**, 83–91, doi:10.1016/j.ijthermalsci.2013.03.011.

Morgan, G. W., K. G. Tolhurst, M. W. Poynter, N. Cooper, T. McGuffog, R. Ryan, M. A. Wouters, N. Stephens, P. Black, D. Sheehan, P. Leeson, S. Whight, and S. M. Davey, 2020: Prescribed burning in south-eastern Australia: history and future directions. *Australian Forestry*, **83 (1)**, 4–28, doi:10.1080/00049158.2020.1739883.

Morgan, M. G., P. J. Adams, and D. W. Keith, 2006: Elicitation of expert judgments of aerosol forcing. *Climatic Change*, **75 (1-2)**, 195–214, doi:10.1007/s10584-005-9025-y.

Muser, L. O., 2022: Combining Aerosol Aging and Data Assimilation for Improving Volcanic Aerosol Forecast. Ph.D. thesis, Karlsruher Institut für Technologie (KIT).

Muser, L. O., G. Ali Hoshyaripour, J. Bruckert, Á. Horváth, E. Malinina, S. Wallis, F. J. Prata, A. Rozanov, C. Von Savigny, H. Vogel, and B. Vogel, 2020: Particle aging and aerosol-radiation interaction affect volcanic plume dispersion: Evidence from the Raikoke 2019 eruption. *Atmospheric Chemistry and Physics*, **20 (23)**, 15 015–15 036, doi:10.5194/acp-20-15015-2020.

NASA/LARC/SD/ASDC, 2017a: CALIPSO Imaging Infrared Radiometer Level 1B Radiance data, Standard V2-00. URL https://doi.org/10.5067/IIR/CALIPSO/STANDARD_L1B-V2-00.

———, 2017b: CERES and GEO-Enhanced TOA, Within-Atmosphere and Surface Fluxes, Clouds and Aerosols 1-Hourly Terra-Aqua Edition4A. URL https://doi.org/10.5067/TERRA+AQUA/CERES/SYN1DEG-1HOUR_L3.004A.

Nenes, A., S. N. Pandis, and C. Pilinis, 1998: ISORROPIA: A new thermodynamic equilibrium model for multiphase multicomponent inorganic aerosols. *Aquatic geochemistry*, **4**, 123–152, doi:10.1023/A:1009604003981.

noaa-himawari8, 2024: Aws s3 explorer. URL https://noaa-himawari8.s3.amazonaws.com/index.html, accessed 12.02.2024.

Nolan, R. H., M. M. Boer, V. Resco de Dios, G. Caccamo, and R. A. Bradstock, 2016: Large-scale, dynamic transformations in fuel moisture drive wildfire activity across southeastern Australia. *Geophysical Research Letters*, **43 (9)**, 4229–4238, doi:10.1002/2016GL068614.

Novakov, T., S. Menon, T. W. Kirchstetter, D. Koch, and J. E. Hansen, 2005: Aerosol organic carbon to black carbon ratios: Analysis of published data and implications for climate forcing. *Journal of Geophysical Research: Atmospheres*, **110 (D21)**, doi:10.1029/2005JD005977.

Nussbaumer, T., 1989: *Schadstoffbildung bei der Verbrennung von Holz*. ETH Zurich.

Ohneiser, K., A. Ansmann, H. Baars, P. Seifert, B. Barja, C. Jimenez, M. Radenz, A. Teisseire, A. Floutsi, M. Haarig, A. Foth, A. Chudnovsky, R. Engelmann, F. Zamorano, J. Bühl, and U. Wandinger, 2020: Smoke of extreme Australian bushfires observed in the stratosphere over Punta Arenas, Chile, in January 2020: optical thickness, lidar ratios, and depolarization ratios at 355 and 532 nm. *Atmospheric Chemistry and Physics*, **20 (13)**, 8003–8015, doi:10.5194/acp-20-8003-2020.

Ohneiser, K., A. Ansmann, B. Kaifler, A. Chudnovsky, B. Barja, D. A. Knopf, N. Kaifler, H. Baars, P. Seifert, D. Villanueva, C. Jimenez, M. Radenz, R. Engelmann, I. Veselovskii, and F. Zamorano, 2022: Australian wildfire smoke in the stratosphere: the decay phase in 2020/2021 and impact on ozone depletion. *Atmospheric Chemistry and Physics*, **22 (11)**, 7417–7442, doi:10.5194/acp-22-7417-2022.

Ohneiser, K., A. Ansmann, J. Witthuhn, H. Deneke, A. Chudnovsky, G. Walter, and F. Senf, 2023: Self-lofting of wildfire smoke in the troposphere and stratosphere: simulations and space lidar observations. *Atmospheric Chemistry and Physics*, **23 (4)**, 2901–2925, doi:10.5194/acp-23-2901-2023.

Ortega, A., D. Day, M. Cubison, W. Brune, D. Bon, J. De Gouw, and J. Jimenez, 2013: Secondary organic aerosol formation and primary organic aerosol oxidation from biomass-burning smoke in a flow reactor during FLAME-3. *Atmospheric Chemistry and Physics*, **13 (22)**, 11 551–11 571, doi:10.5194/acp-13-11551-2013.

Pardon, L. G., B. W. Brook, A. D. Griffiths, and R. W. Braithwaite, 2003: Determinants of survival for the northern brown bandicoot under a landscape-scale fire experiment. *Journal of Animal Ecology*, **72 (1)**, 106–115, doi:10.1046/j.1365-2656.2003.00686.x.

Parmar, R. S., M. Welling, M. O. Andreae, and G. Helas, 2008: Water vapor release from biomass combustion. *Atmospheric Chemistry and Physics*, **8**, 6147–6153, doi:10.5194/acp-8-6147-2008.

Paugam, R., M. Wooster, S. Freitas, and M. Val Martin, 2016: A review of approaches to estimate wildfire plume injection height within large-scale atmospheric chemical transport models. *Atmospheric Chemistry and Physics*, **16 (2)**, 907–925, doi:10.5194/acp-16-907-2016.

Peterson, D. A., M. D. Fromm, R. H. McRae, J. R. Campbell, E. J. Hyer, G. Taha, C. P. Camacho, G. P. Kablick III, C. C. Schmidt, and M. T. DeLand, 2021: Australia's Black Summer pyrocumulonimbus super outbreak reveals potential for increasingly extreme stratospheric smoke events. *NPJ climate and atmospheric science*, **4 (1)**, 38, doi:10.1038/s41612-021-00192-9.

Pfister, G., L. Emmons, P. Hess, R. Honrath, J.-F. Lamarque, M. Val Martin, R. Owen, M. Avery, E. V. Browell, J. Holloway, et al., 2006: Ozone production from the 2004 North American boreal fires. *Journal of Geophysical Research: Atmospheres*, **111 (D24)**, doi:10.1029/2006JD007695.

Pimont, F., J.-L. Dupuy, R. R. Linn, and S. Dupont, 2011: Impacts of tree canopy structure on wind flows and fire propagation simulated with FIRETEC. *Annals of Forest Science*, **68**, 523–530, doi:10.1007/s13595-011-0061-7.

Potter, B. E., 2005: The role of released moisture in the atmospheric dynamics associated with wildland fires. *International Journal of Wildland Fire*, **14 (1)**, 77–84, doi:10.1071/WF04045.

Prill, F., D. Reinert, D. Rieger, and G. Zängl, 2022: ICON Tutorial. URL `https://www.dwd.de/DE/leistungen/nwv_icon_tutorial/pdf_einzelbaende/icon_tutorial2020.pdf?__blob=publicationFile&v=4`.

Pósfai, M., R. Simonics, J. Li, P. V. Hobbs, and P. R. Buseck, 2003: Individual aerosol particles from biomass burning in southern Africa: 1. Compositions and size distributions of carbonaceous particles. *Journal of Geophysical Research: Atmospheres*, **108 (D13)**, doi:10.1029/2002JD002291.

Raffuse, S. M., K. J. Craig, N. K. Larkin, T. T. Strand, D. C. Sullivan, N. J. Wheeler, and R. Solomon, 2012: An evaluation of modeled plume injection height with satellite-derived observed plume height. *Atmosphere*, **3 (1)**, 103–123, doi:10.3390/atmos3010103.

Ramnarine, E., J. K. Kodros, A. L. Hodshire, C. R. Lonsdale, M. J. Alvarado, and J. R. Pierce, 2019: Effects of near-source coagulation of biomass burning aerosols on global predictions of aerosol size distributions and implications for aerosol radiative effects. *Atmospheric Chemistry and Physics*, **19**, 6561–6577, doi:10.5194/acp-19-6561-2019.

Reid, J. S., T. F. Eck, S. A. Christopher, R. Koppmann, O. Dubovik, D. Eleuterio, B. N. Holben, E. A. Reid, and J. Zhang, 2005a: A review of biomass burning emissions part III: intensive optical properties of biomass burning particles. *Atmospheric Chemistry and Physics*, **5 (3)**, 827–849, doi:10.5194/acp-5-827-2005.

Reid, J. S., P. V. Hobbs, R. J. Ferek, D. R. Blake, J. V. Martins, M. R. Dunlap, and C. Liousse, 1998a: Physical, chemical, and optical properties of regional hazes dominated by smoke in Brazil. *Journal of Geophysical Research Atmospheres*, **103**, 32 059–32 080, doi:10.1029/98JD00458.

Reid, J. S., P. V. Hobbs, C. Liousse, J. V. Martins, R. E. Weiss, and T. F. Eck, 1998b: Comparisons of techniques for measuring shortwave absorption and black carbon content of aerosols from biomass burning in Brazil. *Journal of Geophysical Research: Atmospheres*, **103 (D24)**, 32 031–32 040, doi:10.1029/98JD00773.

Reid, J. S., R. Koppmann, T. F. Eck, and D. P. Eleuterio, 2005b: A review of biomass burning emissions part II: intensive physical properties of biomass burning particles. *Atmos. Chem. Phys*, **5**, 799–825, doi:10.5194/acp-5-799-2005.

Remer, L. A., Y. J. Kaufman, B. N. Holben, A. M. Thompson, and D. McNamara, 1998: Biomass burning aerosol size distribution and modeled optical properties. *Journal of Geophysical Research Atmospheres*, **103**, 31 879–31 891, doi:10.1029/98JD00271.

Rieger, D., M. Bangert, I. Bischoff-Gauss, J. Förstner, K. Lundgren, D. Reinert, J. Schröter, H. Vogel, G. Zängl, R. Ruhnke, et al., 2015: ICON–ART 1.0–a new online-coupled model system from the global to regional scale. *Geoscientific Model Development*, **8 (6)**, 1659–1676, doi:10.5194/gmd-8-1659-2015.

Rieger, D., M. Kohler, R. J. Hogan, S. A. K. Schafer, A. Seifert, A. De Lozar, and G. Zängl, 2019: ecRad in ICON - Details on the Implementation and First Results. *Journal of Advances in Modeling Earth Systems*, **10 (8)**, 1990–2008, doi:10.5676/DWD_pub/nwv/icon$_0$04.

Riemer, N., 2002: Numerische Simulationen zur Wirkung des Aerosols auf die troposphärische Chemie und die Sichtweite. Ph.D. thesis.

Riley, M., J. Kirkwood, N. Jiang, G. Ross, and Y. Scorgie, 2020: Air quality monitoring in NSW: From long term trend monitoring to integrated urban services. *Air Quality and Climate Change*, **54 (1)**, 44–51, doi:10.3316/informit.078202598997117.

Rio, C., F. Hourdin, and A. Chédin, 2010: Numerical simulation of tropospheric injection of biomass burning products by pyro-thermal plumes. *Atmospheric Chemistry and Physics*, **10 (8)**, 3463–3478, doi:10.5194/acp-10-3463-2010.

Roberts, G., M. J. Wooster, and E. Lagoudakis, 2009: Annual and diurnal african biomass burning temporal dynamics. *Biogeosciences*, **6 (5)**, 849–866, doi:10.5194/bg-6-849-2009.

Rodgers, C. D., 2000: *Inverse methods for atmospheric sounding: theory and practice*, Vol. 2. World scientific.

Rosenfeld, D., M. Fromm, J. Trentmann, G. Luderer, M. Andreae, and R. Servranckx, 2007: The Chisholm firestorm: observed microstructure, precipitation and lightning activity of a pyro-cumulonimbus. *Atmospheric Chemistry and Physics*, **7 (3)**, 645–659, doi:10.5194/acp-7-645-2007.

Russell-Smith, J. and D. Bowman, 1992: Conservation of monsoon rainforest isolates in the Northern Territory, Australia. *Biological Conservation*, **59 (1)**, 51–63, doi:10.1016/0006-3207(92)90713-W.

Russell-Smith, J., P. G. Ryan, and D. C. Cheal, 2002: Fire regimes and the conservation of sandstone heath in monsoonal northern Australia: frequency, interval, patchiness. *Biological conservation*, **104 (1)**, 91–106, doi:10.1016/S0006-3207(01)00157-4.

Russell-Smith, J., P. G. Ryan, D. Klessa, G. Waight, and R. Harwood, 1998: Fire regimes, fire-sensitive vegetation and fire management of the sandstone Arnhem Plateau, monsoonal northern Australia. *Journal of Applied Ecology*, **35 (6)**, 829–846, doi:10.1111/j.1365-2664.1998.tb00002.x.

Sakaeda, N., R. Wood, and P. J. Rasch, 2011: Direct and semidirect aerosol effects of southern African biomass burning aerosol. *Journal of Geophysical Research: Atmospheres*, **116 (D12)**, doi:10.1029/2010JD015540.

Sakamoto, K. M., J. D. Allan, H. Coe, J. W. Taylor, T. J. Duck, and J. R. Pierce, 2015: Aged boreal biomass-burning aerosol size distributions from BORTAS 2011. *Atmospheric Chemistry and Physics*, **15**, 1633–1646, doi:10.5194/acp-15-1633-2015.

Schraufnagel, D. E., 2020: The health effects of ultrafine particles. *Experimental & molecular medicine*, **52 (3)**, 311–317, doi:10.1038/s12276-020-0403-3.

Schröter, J., D. Rieger, C. Stassen, H. Vogel, M. Weimer, S. Werchner, J. Förstner, F. Prill, D. Reinert, G. Zängl, M. Giorgetta, R. Ruhnke, B. Vogel, and P. Braesicke, 2018: ICON-ART 2.1: a flexible tracer framework and its application for composition studies in numerical weather forecasting and climate simulations. *Geoscientific Model Development*, **11 (10)**, 4043–4068, doi:10.5194/gmd-11-4043-2018.

Schuster, G. L., O. Dubovik, and B. N. Holben, 2006: Angstrom exponent and bimodal aerosol size distributions. *Journal of Geophysical Research: Atmospheres*, **111 (D7)**, doi:10.1029/2005JD006328.

Sellitto, P., R. Belhadji, C. Kloss, and B. Legras, 2022: Radiative impacts of the Australian bushfires 2019–2020–Part 1: Large-scale radiative forcing. *Atmospheric Chemistry and Physics*, **22 (14)**, 9299–9311, doi:10.5194/acp-22-9299-2022.

Simoneit, B. R., 2002: Biomass burning— a review of organic tracers for smoke from incomplete combustion. *Applied Geochemistry*, **17 (3)**, 129–162, doi:10.1016/S0883-2927(01)00061-0.

Sofiev, M., T. Ermakova, and R. Vankevich, 2012: Evaluation of the smoke-injection height from wild-land fires using remote-sensing data. *Atmospheric Chemistry and Physics*, **12 (4)**, 1995–2006, doi:10.5194/acp-12-1995-2012.

Stith, J. L., L. F. Radke, and P. V. Hobbs, 1981: Particle emissions and the production of ozone and nitrogen oxides from the burning of forest slash. *Atmospheric Environment (1967)*, **15 (1)**, 73–82, doi:10.1016/0004-6981(81)90127-X.

Sun, R., M. A. Jenkins, S. K. Krueger, W. Mell, and J. J. Charney, 2006: An evaluation of fire-plume properties simulated with the Fire Dynamics Simulator (FDS) and the Clark coupled wildfire model. *Canadian Journal of Forest Research*, **36**, 2894–2908, doi:10.1139/X06-138.

Thurston, W., K. J. Tory, R. J. Fawcett, and J. D. Kepert, 2015: Large-eddy simulations of pyro-convection and its sensitivity to environmental conditions. *Research Proc. Bushfire and Natural Hazards CRC & AFAC 2015 Conf*, 148–160.

Tiedtke, M., 1989: A comprehensive mass flux scheme for cumulus parameterization in large-scale models. *Monthly weather review*, **117 (8)**, 1779–1800, doi:10.1175/1520-0493(1989)117<1779:ACMFSF>2.0.CO;2.

Tory, K. J. and J. D. Kepert, 2021: Pyrocumulonimbus Firepower Threshold: Assessing the atmospheric potential for pyroCb. *Weather and Forecasting*, **36 (2)**, 439–456, doi:10.1175/WAF-D-20-0027.1.

Trentmann, J., 2001: Atmospheric processes in a young biomass burning plume-radiation and chemistry. Ph.D. thesis, Universität Hamburg Hamburg.

Trentmann, J., M. O. Andreae, H.-F. Graf, P. V. Hobbs, R. D. Ottmar, and T. Trautmann, 2002: Simulation of a biomass-burning plume: Comparison of model results with observations. *Journal of Geophysical Research: Atmospheres*, **107 (D2)**, AAC 5–1–AAC 5–15, doi:10.1029/2001JD000410.

Trentmann, J., G. Luderer, T. Winterrath, M. Fromm, R. Servranckx, C. Textor, M. Herzog, H.-F. Graf, and M. Andreae, 2006: Modeling of biomass smoke injection into the lower stratosphere by a large forest fire (Part I): reference simulation. *Atmospheric Chemistry and Physics*, **6 (12)**, 5247–5260, doi:10.5194/acp-6-5247-2006.

Turquety, S., J. A. Logan, D. J. Jacob, R. C. Hudman, F. Y. Leung, C. L. Heald, R. M. Yantosca, S. Wu, L. K. Emmons, D. P. Edwards, et al., 2007: Inventory of boreal fire emissions for North America in 2004: Importance of peat burning and pyroconvective injection. *Journal of Geophysical Research: Atmospheres*, **112 (D12)**, doi:10.1029/2006JD007281.

Val Martin, M., R. E. Honrath, R. C. Owen, G. Pfister, P. Fialho, and F. Barata, 2006: Significant enhancements of nitrogen oxides, black carbon, and ozone in the north atlantic lower free troposphere resulting from north american boreal wildfires. *Journal of Geophysical Research: Atmospheres*, **111 (D23)**, D23S60, doi:10.1029/2006JD007530.

Val Martin, M., R. A. Kahn, J. A. Logan, R. Paugam, M. Wooster, and C. Ichoku, 2012: Space-based observational constraints for 1-D fire smoke plume-rise models. *Journal of Geophysical Research: Atmospheres*, **117 (D22)**, 204, doi:10.1029/2012JD018370.

Val Martin, M., J. Logan, R. Kahn, F.-Y. Leung, D. Nelson, and D. Diner, 2010: Smoke injection heights from fires in North America: analysis of 5 years of satellite observations. *Atmospheric Chemistry and Physics*, **10 (4)**, 1491–1510, doi:10.5194/acp-10-1491-2010.

Vestin, A., J. Rissler, E. Swietlicki, G. P. Frank, and M. O. Andreae, 2007: Cloud-nucleating properties of the Amazonian biomass burning aerosol: Cloud condensation nuclei measurements and modeling. *Journal of Geophysical Research Atmospheres*, **112**, 1–16, doi:10.1029/2006JD008104.

Viney, N. R., 1991: A review of fine fuel moisture modelling. *International Journal of Wildland Fire*, **1 (4)**, 215–234, doi:10.1071/WF9910215.

Wacker, U., T. Frisius, and F. Herbert, 2006: Evaporation and precipitation surface effects in local mass continuity laws of moist air. *Journal of the atmospheric sciences*, **63 (10)**, 2642–2652, doi:10.1175/JAS3754.1.

Walter, C., S. R. Freitas, C. Kottmeier, I. Kraut, D. Rieger, H. Vogel, and B. Vogel, 2016: The importance of plume rise on the concentrations and atmospheric impacts of biomass burning aerosol. *Atmospheric Chemistry and Physics*, **16**, 9201–9219, doi:10.5194/acp-16-9201-2016.

Wang, J., S. A. Christopher, U. Nair, J. S. Reid, E. M. Prins, J. Szykman, and J. L. Hand, 2006: Mesoscale modeling of Central American smoke transport to the United States: 1."Top-down" assessment of emission strength and diurnal variation impacts. *Journal of Geophysical Research: Atmospheres*, **111 (D5)**, doi:10.1029/2005JD006416.

Weimer, M., J. Schröter, J. Eckstein, K. Deetz, M. Neumaier, G. Fischbeck, L. Hu, D. B. Millet, D. Rieger, H. Vogel, B. Vogel, T. Reddmann, O. Kirner, R. Ruhnke, and P. Braesicke, 2017: An emission module for ICON-ART 2.0: implementation and simulations of acetone. *Geoscientific Model Development*, **10 (6)**, 2471–2494, doi:10.5194/gmd-10-2471-2017.

Whitby, E. R. and P. H. McMurry, 1997: Modal aerosol dynamics modeling. *Aerosol Science and Technology*, **27 (6)**, 673–688, doi:10.1080/02786829708965504.

Williams, R., R. Bradstock, G. Cary, N. Enright, A. Gill, A. Leidloff, C. Lucas, R. Whelan, A. Andersen, D. Bowman, P. Clarke, G. Cook, K. Hennessy, and A. York, 2009: Interactions between climate change, fire regimes and biodiversity in Australia: A preliminary assessment.

Woinarski, J., D. Milne, and G. Wanganeen, 2001: Changes in mammal populations in relatively intact landscapes of Kakadu National Park, Northern Territory, Australia. *Austral ecology*, **26 (4)**, 360–370, doi:10.1046/j.1442-9993.2001.01121.x.

Woinarski, J. C., M. Armstrong, K. Brennan, A. Fisher, A. D. Griffiths, B. Hill, D. Milne, C. Palmer, S. Ward, M. Watson, et al., 2010: Monitoring indicates rapid and severe decline of native small mammals in Kakadu National Park, northern Australia. *Wildlife Research*, **37 (2)**, 116–126, doi:10.1071/WR09125.

Wolfe, R. E., D. P. Roy, and E. Vermote, 1998: MODIS land data storage, gridding, and compositing methodology: Level 2 grid. *IEEE Transactions on Geoscience and Remote Sensing*, **36 (4)**, 1324–1338, doi:10.1109/36.701082.

Wooster, M. J., G. Roberts, G. Perry, and Y. Kaufman, 2005: Retrieval of biomass combustion rates and totals from fire radiative power observations: FRP derivation and calibration relationships between biomass consumption and fire radiative energy release. *Journal of Geophysical Research: Atmospheres*, **110 (D24)**, doi:10.1029/2005JD006318.

Wu, H., J. W. Taylor, K. Szpek, J. M. Langridge, P. I. Williams, M. Flynn, J. D. Allan, S. J. Abel, J. Pitt, M. I. Cotterell, C. Fox, N. W. Davies, J. Haywood, and H. Coe, 2020: Vertical variability of the properties of highly aged biomass burning aerosol transported over the southeast Atlantic during CLARIFY-2017. *Atmospheric Chemistry and Physics*, **20**, 12 697–12 719, doi:10.5194/acp-20-12697-2020.

Zhang, X. and S. Kondragunta, 2008: Temporal and spatial variability in biomass burned areas across the USA derived from the GOES fire product. *Remote Sensing of Environment*, **112 (6)**, 2886–2897, doi:10.1016/j.rse.2008.02.006.

Zängl, G., D. Reinert, P. Rípodas, and M. Baldauf, 2015: The ICON (ICOsahedral Non-hydrostatic) modelling framework of DWD and MPI-M: Description of the non-hydrostatic dynamical core. *Quarterly Journal of the Royal Meteorological Society*, **141 (687)**, 563–579, doi:10.1002/qj.2378.

D. List of Figures

E. List of Tables

Acknowledgments

This study contains modified Copernicus Atmosphere Monitoring Service information [2023]. Further, I would like to thank the University of Wyoming for distributing the radiosonde data, the Bureau of Meteorology's "Climate Data Services"division for providing the AWS data and the CAR's National Air Pollution Monitor Database (NAPMD) for the data on air quality. JMA Himawari-8/9 was accessed on 25.05.23 from `https://registry.opendata.aws/noaa-himawari`. CALIPSO products are available at the Atmospheric Science Data Center of the NASA Langley Research Center. Furthermore, resources of the Deutsches Klimarechenzentrum (DKRZ) under project ID bb1070 have been used. Finally, I would like to thank the Graduate School for Climate and Environment (GRACE) for the support and opportunities that have contributed to this work.

Special thanks

Ich möchte dieses Kapitel nutzen um all jenen zu danken, die mich in bei dieser Arbeit unterstützet haben und diese Arbeit möglich gemacht haben.
An erster Stelle möchte ich mich bei Prof. Dr. Corinna Hoose für die Begutachtung und Betreuung bedanken. Danke für die produktiven Treffen, die konstruktive Kritik und die Unterstützung und Ermutigung für meinen Auslandsaufenthalt in Melbourne, all das hat meine Arbeit sehr weiter gebracht.
Ich danke auch Prof. Dr. Peter Braesicke für die Begutachtung und die Übernahme des Amt des Korreferenten.
Mein besonderer Dank gilt Dr. Bernhard Vogel, durch dich wurde diese Arbeit erst möglich. Danke für die gute Betreuung und die konstruktiven Treffen, die mich stets weitergebracht. Herzlichen Dank, dass du diese Treffen auch in deinen Ruhestand noch weitergeführt hast.
Mein weiterer Dank geht an Dr. Ali Hoshyaripour für die Betreuung, die Zeit für Treffen und Unterstützung und die Ermutigung an der Teilnahme internationaler Konferenzen.
Next, I want to thank the whole (current and former) working group "Aerosol and Reactive Tracer Modelling", especially Dr. Heike Vogel, Dr. Sven Werchner, Dr. Lukas Muser, Dr. Anika Rohde, Dr. Julia Bruckert Simran Chopra, and Sascha Bierbauer. I am grateful for the nice atmosphere at work, the open doors, all the help and the teamwork that have contributed significantly to this work.
An dieser Stelle möchte ich besonders Dr. Heike Vogel danken! Danke, für die ganze Hilfe und Un-

terstützung bei Fehlersuchen, Diskussionen von Ergebnissen, besonders aber auch für die moralische Unterstützung, Networking und schönen Gespräche zwischen den Türen privat und wissenschaftlich.
A special thanks goes to Dr. Jeremy Silver and the School of Mathematics and Statistics of the University of Melbourne. Thanks for the kind welcome, the discussions and input on my work during my three months aboard. It was a great experience for me, widened my horizons and contributed to this work.
A further thanks goes to all the members of the PermaStrom project. Thank you for including me and all the nice and constructive project meetings I was able to participate.
I further want to thank Dr. Akos Horvath, Dr. Jim Carr and Dr. Mariel Friberg for making the NASA 3DWind code available to me and all the help with setting up the retrievals an interpreting the results.
Ein großer Dank gilt meiner Familie, besonders meinen Eltern Claudia und Michael Muth, die mich seit ich denken kann in jeglicher Hinsicht unterstützt und an mich geglaubt haben. Außerdem möchte ich meinen Mitbewohner:innen in verschiedenen Konstellationen danken: Dr. Nikolas Schiffmann, Dr. Laura Merker, Felix Groden, Maike Rees, Felix Bösch, Joshua Grupp und Nils Senge. Vielen Dank für die tolle Zeit und den Rückhalt, besonders in der finalen Phase. Danke auch für die Routine und das gemeinsame Home Office in Pandemie-Zeiten, ihr habt auch dieser Zeit etwas Schönes gegeben.
Ein ganz herzlicher Dank geht an die "Meteo Chiller", danke für die tolle Zeit und Hilfe im Studium, die wegweisend für diese Arbeit war.
A special thanks goes to everyone who took the time and afford to read and feedback this thesis, Dr. Bernhard Vogel, Dr. Ali Hoshyaripour, Prof. Dr. Corinna Hoose, Timo Doll – , Aliza Mushtaq, Rouven Losert, Anna-Katharina Muth und Claudia Muth. Besonders möchte ich meinem Vater danken, der diese Arbeit bewundernswerten Engagement gelesen hat.
Finally, I would like to thank "The Front Bottoms"for the background music, which made long debugging and plotting sessions bearable and sometimes even fun.